Quadrupole Couplings in Nuclear Magnetic Resonance, General

Pascal P. Man

in
Encyclopedia of Analytical Chemistry
R.A. Meyers (Ed.)
pp. 12224–12265

Quadrupole Couplings in Nuclear Magnetic Resonance, General

Pascal P. Man
Université Pierre et Marie Curie, Paris, France

Nuclear magnetic resonance (NMR) spectroscopy is continually finding new applications. It enables the local symmetry to be probed at the atomic scale using the nuclear spins I *of the compound under investigation. The nuclear spin is either a half-integer (or odd) number or an integer (or even) number. The nuclei in the periodic table can be divided into two parts – spin-$\frac{1}{2}$ nuclei and spin larger than $\frac{1}{2}$ nuclei. The spin larger than $\frac{1}{2}$ nuclei are called quadrupole nuclei because they possess an electric quadrupole moment which interacts with the electric-field gradient (EFG) generated by its surroundings. By extension, their spins are called quadrupole spins. Spin-$\frac{1}{2}$ nuclei are not sensitive to the EFG. Of the nuclei that possess a spin, 6% have integer quadrupole spins and 66% have half-integer quadrupole spins.*

This article focuses on the half-integer quadrupole spins ($I = \frac{3}{2}, \frac{5}{2}, \frac{7}{2}$, and $\frac{9}{2}$) in single crystals and in powder compounds. Most of these spins are observable. As they are multi-energy-level systems (the number of energy levels is $2I + 1$), multiple quantum (MQ) transitions occur during excitation of the spin system by a radiofrequency (RF) pulse sequence. As a result, quantum mechanical concepts are needed for an understanding of the spin dynamics and for interpretation of the results. In particular, the choice of pulse sequence and the experimental conditions, such as pulse duration, pulse strength, and phase cycling in the pulse sequence, depend on the strength of the EFG surrounding the nuclear spin.

1 INTRODUCTION

Most nuclei in the periodic table have a spin I larger than $\frac{1}{2}$. These spins are called quadrupole spins and they are sensitive to the EFG generated by their surroundings. The coupling of the nuclear electric quadrupole moment eQ (a property of the nucleus) with an EFG (a property of the sample) is called the quadrupole interaction.[1–3] Nuclei with quadrupole spins are extensively used to probe static and dynamic phenomena accompanying reversible phase transitions in solids.[4–6] This article focuses on half-integer quadrupole spins ($I = \frac{3}{2}, \frac{5}{2}, \frac{7}{2}$, and $\frac{9}{2}$) in NMR experiments; that is, the interaction of the spin system with the Zeeman field $\mathbf{B}_0$ (the strong static magnetic field) is much larger than the quadrupole interaction.[7] Under these conditions, we consider the first two expansion terms of this interaction, namely the first- and second-order quadrupole interactions.

There are two ways to investigate the effects of an interaction in NMR:

- Studying the frequency-domain response of the spin system, which deals with transition frequencies between two energy levels and therefore the line positions, line shifts, and line shapes in the spectrum.
- Predicting the time-domain response of the spin system, namely the signal intensities, positions and amplitudes of echoes by using the density operator formalism.

Two-dimensional (2-D) NMR experiments are based on the time-domain response of the spin system to specific sequences, designed in such a way that the desired information is clearly shown in 2-D spectra.[8–10]

The main effects of the quadrupole interaction in the frequency domain are gathered in section 2 but are not developed because excellent review articles are available in the *Encyclopedia of Nuclear Magnetic Resonance*.[11,12] Expressions for the second-order quadrupole shift of the central line under static conditions, and for variable- and magic-angle spinning (MAS) are provided, together with the procedure for simulating powder patterns. As the spectra are the Fourier transforms of time-domain signals, which depend on the experimental parameters such as the strength of $\mathbf{B}_0$, that of the RF field $\mathbf{B}_1$, the pulse durations, the pulse separation, or the relative

Encyclopedia of Analytical Chemistry
R.A. Meyers (Ed.) Copyright © John Wiley & Sons Ltd

phase of the RF pulses, understanding of the effects of these parameters enables the undistorted line shapes to be obtained.

Section 3 deals with the time-domain response of the spin system excited by one- and two-pulse sequences that include Solomon echoes[1,13] and Hahn echoes.[14] Section 3.1, which focuses on one-pulse and 2-D nutation experiments, gives the meanings of the elements of the density matrix at the end of an RF pulse. The properties of these elements are crucial for an understanding of echoes in NMR. Nonselective (or hard) pulse excitation, and selective excitation of the spin system are presented to establish the experimental conditions for quantification of the spin population. For this purpose, the nature of a line (only the central line or the full spectrum) must be determined by a one-dimensional (1-D) nutation experiment. Section 3.2 presents a composite-pulse sequence that cancels spurious signals generated by the NMR probe when low-gyromagnetic-ratio nuclei are studied in a Zeeman field $\mathbf{B}_0$. Quantification of the spin population with this composite-pulse sequence is not possible. The numerical procedures for calculating the line intensity from single-pulse and composite-pulse sequences are given.

Section 3.3 presents a method for obtaining the two quadrupole parameters (the quadrupole coupling constant and the asymmetry parameter) from a featureless central-transition line shape by using a two-pulse sequence with a short pulse separation. This method is an extension of the 1-D nutation experiment, which is based on the fact that the variation of the line intensity versus a pulse duration depends on the ratio of the quadrupole coupling w_Q to the strength w_{RF} of the RF field $\mathbf{B}_1$. Furthermore, knowledge of the two quadrupole parameters allows the true isotropic chemical shift of a line to be determined. The latter is related to bond angle in solids.[15]

The broad powder pattern is distorted by the dead time of the receiver following an RF pulse. The usual way to overcome this problem is to apply a spin echo sequence. However, there is a subtle but important difference between Solomon echoes and Hahn echoes. Extensive examples are provided for supporting predictions. For simplicity mainly spins $I = \frac{3}{2}$ and $\frac{5}{2}$ are discussed because they represent the most-studied nuclei. Section 3.4 discusses Solomon echoes with respect to the excitation conditions, namely nonselective (or hard-pulse) excitation, and soft-pulse excitation. These echoes are satellite-transition signals only, because the delay separating the two RF pulses is much shorter than the duration of the free-induction decay (FID) of the central transition.[16] A numerical procedure is proposed to calculate the amplitudes of Solomon echoes, allowing the conditions for their observation to be optimized. Quantification of the spin population is not possible with satellite-transition signals.

For Hahn echoes, which are discussed in section 3.5, the pulse separation is larger than the duration of the central-transition FID; both central-transition and satellite-transition echoes are observed.[17,18] As a result of the spin–spin relaxation, Hahn echo amplitudes are much smaller than Solomon echo amplitudes. The various excitation conditions are also reviewed to deduce the conditions for quantifying the spin population. Hahn echo sequences also cancel spurious signals. A numerical procedure is proposed to predict the echo amplitudes. Section 3.5.7 discusses Hahn echoes in rapidly rotating samples. Finally, a 2-D multiple quantum/magic-angle spinning (MQ/MAS) experiment is reviewed in section 3.5.8. Emphases are on the various conventions for scaling and labeling the high-resolution axis in a 2-D sheared spectrum.

2 FREQUENCY-DOMAIN RESPONSE

2.1 Quadrupole Interaction

In its principal-axis system (PAS), the EFG tensor $\mathbf{V}$ is given by Equation (1):

$$\mathbf{V} = \begin{pmatrix} V_{XX} & 0 & 0 \\ 0 & V_{YY} & 0 \\ 0 & 0 & V_{ZZ} \end{pmatrix} \tag{1}$$

As the Laplace equation is valid, $V_{XX} + V_{YY} + V_{ZZ} = 0$, two new parameters are used: the largest component eq (Equation 2) and the asymmetry parameter η (Equation 3),

$$eq = V_{ZZ} \tag{2}$$

$$\eta = \frac{V_{XX} - V_{YY}}{V_{ZZ}} \tag{3}$$

with $0 \leq \eta \leq 1$. If necessary, the axes of the EFG tensor are relabeled to satisfy Equations (2) and (3). The definition of η is not unique.[11]

In NMR, the quadrupole interaction is treated as a weak perturbation of the Zeeman interaction (Equation 4),

$$H_Z = -w_L I_z \tag{4}$$

the coupling of the nuclear spin I with the Zeeman field $\mathbf{B}_0$. The Larmor frequency (Equation 5) is

$$w_L = \gamma \mathbf{B}_0 \tag{5}$$

which is a positive number if the gyromagnetic ratio γ is positive. The standard approach mainly considers the

first two perturbation terms of the quadrupole interaction. These are the first-order quadrupole interaction (Equation 6),

$$H_Q^{(1)} = N_Q \tfrac{1}{6}\sqrt{6}\{3I_z^2 - I(I+1)\}V_{2,0} \tag{6}$$

and the second-order quadrupole interaction (Equations 7 and 8),

$$H_Q^{(2)} = -\frac{N_Q^2}{w_L}\left(\tfrac{1}{2}V_{2,-1}V_{2,1}\{4I(I+1) - 8I_z^2 - 1\} + \tfrac{1}{2}V_{2,-2}V_{2,2}\{2I(I+1) - 2I_z^2 - 1\}\right) I_z \tag{7}$$

$$N_Q = \frac{eq}{2I(2I-1)\hbar} \tag{8}$$

The terms $V_{2,k}$ are the components of the EFG expressed as a spherical tensor of rank 2. The interaction $H_Q^{(1)}$ in Equation (6) is an *even* function of I_z. However, in Equation (7), $H_Q^{(2)}$ is an *odd* function of I_z. That is, Equation (7) can be rewritten as Equation (9):

$$H_Q^{(2)} = A_Q^{(2)} I_z^3 + B_Q^{(2)} I_z \tag{9}$$

The interaction $H_Q^{(1)}$ is independent of w_L, whereas $H_Q^{(2)}$ is inversely proportional to it. This means that the effect of $H_Q^{(2)}$ decreases when the strength of $\mathbf{B}_0$ increases.

Under static conditions $H_Q^{(1)}$ can be expressed as Equations (10–12):

$$H_Q^{(1)} = \tfrac{1}{3}w_Q\{3I_z^2 - I(I+1)\} \tag{10}$$

$$w_Q = \tfrac{3}{4}\Omega_Q(3\cos^2\beta - 1 + \eta\sin^2\beta\cos 2\alpha) \tag{11}$$

$$\Omega_Q = eQN_Q = \frac{e^2qQ}{2I(2I-1)\hbar} \tag{12}$$

The definition of the quadrupole coupling w_Q in Equation (10) is not unique. It is half that used by Abragam.[1] Fortunately, the quadrupole coupling constant $e^2qQ/\hbar$ is universally accepted. The angles α and β are the first two Euler angles of $\mathbf{B}_0$ in the PAS of the EFG tensor. However, β and α are the polar angles of $\mathbf{B}_0$ in this system. The definition of the Euler angles is also not unique.[11] Various conventions about signs of phases and frequencies have appeared in the NMR literature.[19]

In a powder sample consisting of many small single crystals oriented randomly with respect to $\mathbf{B}_0$, the values of α and $\cos\beta$ are distributed with equal probability. The factor $\cos\beta$ is involved instead of β because the elementary solid angle is $\sin\beta\,\mathrm{d}\beta\,\mathrm{d}\alpha = \mathrm{d}(\cos\beta)\,\mathrm{d}\alpha$. The histogram $P(w_Q)$ is obtained by counting the frequency lying between w_Q and $w_Q + \Delta w_Q$ for any combination of α and $\cos\beta$.

Combining Equations (11) and (12) gives Equation (13):

$$y = w_Q\frac{8I(2I-1)\hbar}{3e^2qQ} = 3\cos^2\beta - 1 + \eta\sin^2\beta\cos 2\alpha \tag{13}$$

which varies between $-(1+\eta)$ and 2, and reaches $\{-2, 2\}$ when $\eta = 1$. The interval $\{-2, 2\}$ is divided into n parts. For a given η, the values of y are computed for every combination of $\alpha = 2u\pi/M$ and $\cos\beta = r/M(u, r = 0, \ldots, M)$. The y values falling into the n intervals are counted. We chose $n = 41$ and $M = 300$. This procedure was proposed by Narita and colleagues.[20] It allows us to simulate the powder pattern (i.e. the equivalents of the spectrum of a powder sample) $P(y)$ of a satellite transition. Therefore, comparing the shape and the spreading of the experimental powder pattern with the simulated one provides the asymmetry parameter and the quadrupole coupling constant, respectively.

The spectral line intensity[21] and the echo amplitude (which are dealt with in section 3) do not depend on the sign of w_Q or y. So $P(y < 0)$ is co-added to $P(y > 0)$, reducing the numbers of values of $P(y)$ to $\frac{1}{2}(1+n)$. Other procedures giving the same result but with less computation time are available.[22,23]

2.2 Energy Levels and Spectrum

Figure 1 shows the splitting and shift of the energy levels, as well as those of the absorption lines (simply lines in the remainder of this article) in the spectra for a spin $I = \frac{3}{2}$ system in a single crystal, when considering $H_Q^{(1)}$ and $H_Q^{(2)}$.

Without $\mathbf{B}_0$, the four energy levels of a free spin-I system are degenerate (state a). When the spin system is introduced into $\mathbf{B}_0$, the Zeeman interaction splits these energy levels equally (state b) with $|I, m\rangle = |\frac{3}{2}, \frac{3}{2}\rangle, |\frac{3}{2}, \frac{1}{2}\rangle, |\frac{3}{2}, -\frac{1}{2}\rangle$, and $|\frac{3}{2}, -\frac{3}{2}\rangle$, or simply $|m\rangle = |\frac{3}{2}\rangle, |\frac{1}{2}\rangle, |-\frac{1}{2}\rangle$, and $|-\frac{3}{2}\rangle$. The difference between two consecutive energy levels defines w_L, giving a single line in the spectrum, shown as b′.

The first-order quadrupole interaction generates small shifts of the energy levels. As $H_Q^{(1)}$ is an even function of I_z, the energy-level shifts are an even function of the magnetic number m. Therefore two energy levels having the same $|m|$ are shifted by the same quantity: $\langle m|H_Q^{(1)}|m\rangle = \pm w_Q$ for a spin $I = \frac{3}{2}$ (state c), depending on $|m|$. The transition $(-\frac{1}{2} \leftrightarrow \frac{1}{2})$ is called the central transition; the other two transitions $(-\frac{3}{2} \leftrightarrow -\frac{1}{2})$ and $(\frac{1}{2} \leftrightarrow \frac{3}{2})$ are called the satellite transitions. As the two energy levels of the central transition are shifted by the same quantity, the line in the spectrum, called the central line, remains at w_L. However, the satellite lines are shifted by $\pm 2w_Q$ from the central line (shown as c′).

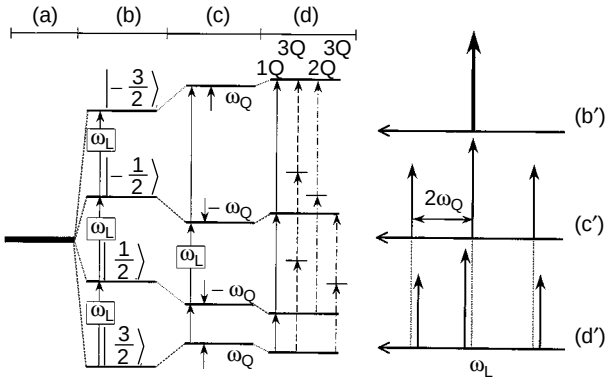

Figure 1 The four energy levels $|\frac{3}{2}\rangle$, $|\frac{1}{2}\rangle$, $|-\frac{1}{2}\rangle$, and $|-\frac{3}{2}\rangle$ for a spin $I = \frac{3}{2}$ system in a single crystal in (state a) zero Zeeman field $\mathbf{B}_0$, (b) in the presence of $\mathbf{B}_0$, (c) including the first-order quadrupole interaction $H_Q^{(1)}$, and (d) including the second-order quadrupole interaction $H_Q^{(2)}$. Their corresponding spectra are represented as arrows in (b′), (c′), and (d′), respectively. The figure provides definitions of the quadrupole coupling w_Q (c′) and of the Larmor frequency w_L (b). The transitions (d) between two energy levels occur during excitation of the spin system by an RF pulse: one-quantum (1Q) transitions are represented by solid arrows, 2Q transitions by dot-dashed arrows, and 3Q transitions by dashed arrows; for clarity, −1Q, −2Q, and −3Q transitions are not shown.

The effect of $H_Q^{(2)}$ is to shift the energy levels further (state d). As a result, an additional shift with respect to w_L, called the second-order quadrupole shift, occurs for each absorption line. However, this second-order quadrupole shift of a line is much smaller than the $\pm 2w_Q$ shift due to $H_Q^{(1)}$. As $H_Q^{(2)}$ is an odd function of I_z, the energy-level shifts are an odd function of m. Therefore, two energy levels having the same $|m|$ are shifted by the same quantity but in the opposite direction. Even the central line is shifted from w_L (shown as d′). Therefore the observed position of the central line is not w_L. The direction of the line shift depends on the orientation of $\mathbf{B}_0$ in the PAS of the EFG tensor.

To detect the presence of these split energy levels, a time-dependent perturbation has to be applied.[24] Continuous wave (CW) NMR applies an RF magnetic field $\mathbf{B}_1$ of *very weak* amplitude $w_{RF}(= \gamma B_1)$, whose Hamiltonian is (Equation 14)

$$H_{pert} \propto -w_{RF} I_x \cos w_c t \tag{14}$$

where w_c is the carrier or the spectrometer frequency. The RF field $\mathbf{B}_1$ is applied perpendicularly to $\mathbf{B}_0$. Therefore, the sample is surrounded with a bath of RF photons of energy w_c.[25] Excitation of the spin system and detection of its response occur simultaneously by using two RF coils. During the excitation of the spin system by $\mathbf{B}_1$, single quantum (SQ) transitions between two consecutive energy levels as well as MQ transitions between two nonconsecutive energy levels occur.[26] The probability per second that H_{pert} induces a transition between two states $|m\rangle$ and $|m'\rangle$ is proportional to $|\langle m'|I_x|m\rangle|^2$, which vanishes unless $m' = m \pm 1$. The condition $\Delta m = \pm 1$ is the selection rule for magnetic dipole transitions. Transverse magnetizations, detected by an RF coil, are related to SQ transitions. The expression $\zeta^2(m+1, m)$ is used to denote this probability (Equation 15):

$$\begin{aligned}\zeta^2(m+1, m) &\equiv |\langle m+1|I_x|m\rangle|^2 = |\langle m|I_x|m+1\rangle|^2 \\ &= I(I+1) - m(m+1)\end{aligned} \tag{15}$$

In the linear regime where the response of the spin system is proportional to the excitation, the spectral line intensity (the area of the absorption line) is proportional to ζ^2. Table 1 gives the values of ζ^2 as well as those of the relative spectral line intensity

$$\frac{\zeta^2}{\sum_{m=-I}^{I-1} \zeta^2}$$

for various half-integer spins. The effects of MQ transitions are observed in the nonlinear regime by using a stronger $\mathbf{B}_1$, so that the spin system is forced to absorb several RF photons simultaneously.[9,27]

In contrast, in pulsed NMR the process of these transitions is investigated only after the end of a strong

Table 1 Relative spectral line intensities $\zeta^2 \big/ \sum \zeta^2$ of all the SQ transitions ($m \leftrightarrow m+1$) of half-integer spins I, with $\zeta^2(m+1, m) = I(I+1) - m(m+1)$

Spins I	Transitions $m \leftrightarrow m+1$	ζ^2	$\zeta^2 \big/ \sum \zeta^2$
$\frac{1}{2}$	$-\frac{1}{2} \leftrightarrow \frac{1}{2}$	1	1
$\frac{3}{2}$	$\pm\frac{1}{2} \leftrightarrow \pm\frac{3}{2}$	3	3/10
	$-\frac{1}{2} \leftrightarrow \frac{1}{2}$	4	4/10
$\frac{5}{2}$	$\pm\frac{3}{2} \leftrightarrow \pm\frac{5}{2}$	5	5/35
	$\pm\frac{1}{2} \leftrightarrow \pm\frac{3}{2}$	8	8/35
	$-\frac{1}{2} \leftrightarrow \frac{1}{2}$	9	9/35
$\frac{7}{2}$	$\pm\frac{5}{2} \leftrightarrow \pm\frac{7}{2}$	7	7/84
	$\pm\frac{3}{2} \leftrightarrow \pm\frac{5}{2}$	12	12/84
	$\pm\frac{1}{2} \leftrightarrow \pm\frac{3}{2}$	15	15/84
	$-\frac{1}{2} \leftrightarrow \frac{1}{2}$	16	16/84
$\frac{9}{2}$	$\pm\frac{7}{2} \leftrightarrow \pm\frac{9}{2}$	9	9/165
	$\pm\frac{5}{2} \leftrightarrow \pm\frac{7}{2}$	16	16/165
	$\pm\frac{3}{2} \leftrightarrow \pm\frac{5}{2}$	21	21/165
	$\pm\frac{1}{2} \leftrightarrow \pm\frac{3}{2}$	24	24/165
	$-\frac{1}{2} \leftrightarrow \frac{1}{2}$	25	25/165

RF pulse by detecting a FID. Excitation and detection are performed with the same RF coil. Also, SQ and MQ transitions occur during the RF pulse, as in CW NMR. As an RF coil can only detect an FID generated by SQ transitions, a second RF pulse is required to probe the effects of MQ transitions.

When MQ transitions between $|m'\rangle$ and $|m\rangle$ are detected directly as in CW NMR, the absorption line would be located at about $(m' - m)w_L$ as the energy-level diagram suggests (state d in Figure 1). In fact this is not the case – the transition between two nonconsecutive energy levels is a multiple-photon process, as shown for a spin $I = \frac{3}{2}$. If $H_Q^{(1)}$ is the dominant interaction (state c), a 2Q transition is a two-photon process and the frequency of the photon is $w_L \pm w_Q$, depending on the transitions.[27,28] The 3Q transition is a three-photon process. The photon frequency of the central and 3Q transitions is w_L.[27] If $H_Q^{(2)}$ is present, their photon frequency is close to w_L. From a theoretical point of view, to avoid the effects of the Zeeman interaction on the transition frequency $w_{w,q}$ between two energy levels $|w\rangle$ and $|q\rangle$, we define $w_{w,q}$ in the rotating frame of the frequency carrier or, in short, the rotating frame. For the moment, we do not deal with the offset term $H_\Delta = -(w_L - w_c)I_z$. In other words, the Zeeman interaction is not considered in the definition of $w_{w,q}$ (Equation 16):

$$\begin{aligned} w_{w,q} &= \langle w|(H_Q^{(1)} + H_Q^{(2)})|w\rangle - \langle q|(H_Q^{(1)} + H_Q^{(2)})|q\rangle \\ &= w_{w,q}^{(1)} + w_{w,q}^{(2)} \end{aligned} \tag{16}$$

where $w_{w,q}^{(1)}$ and $w_{w,q}^{(2)}$ are, respectively, the first- and second-order quadrupole shifts of the $(w - q)$ quantum absorption line with respect to w_L.

In the simplest pulsed NMR experiment that uses a single RF pulse (Figure 2a), two durations are involved – the duration of the RF pulse t_1 and that of the signal acquisition τ_2. Furthermore we define the duration of the FID by T_{FID}. An FID in the time domain $F(t_1, \tau_2)$ and its spectrum in the frequency domain $S(t_1, w_2)$ are related by the Fourier transform of Equation (17):

$$F(t_1, \tau_2) = \int_{-\infty}^{+\infty} S(t_1, w_2) \exp(-i\tau_2 w_2)\, dw_2 \tag{17}$$

The amplitude of the FID at the end of the RF pulse is given by Equation (18),

$$F(t_1, \tau_2 = 0) = \int_{-\infty}^{+\infty} S(t_1, w_2)\, dw_2 \tag{18}$$

That is, the FID amplitude at the end of the RF pulse is related to the spectral line intensity. In the rotating frame (Figure 2b), the effect of an X pulse is the nutation of the magnetization vector **M** around $\mathbf{B}_1$ located along the x axis. The projection of **M** or the FID is detected along

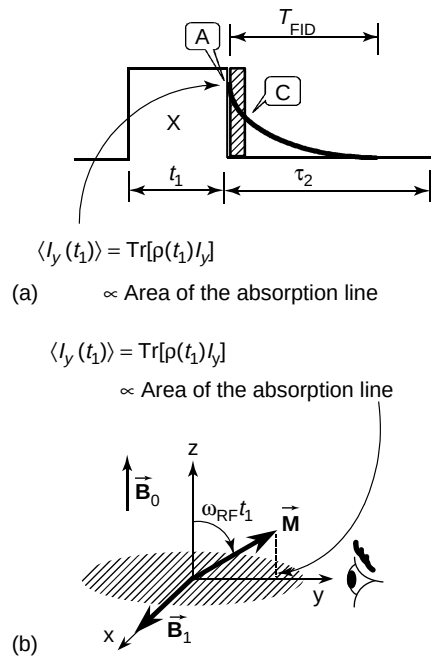

Figure 2 Relationship between the density operator $\rho(t_1)$, the spin operator I_y, and the area of an absorption line (spectral line intensity) or the amplitude of an FID $\langle I_y(t_1)\rangle$. (a) One-pulse experiment: the FID amplitude (point A) following the RF pulse is lost in the dead-time (shaded area) of the receiver; the acquisition of the FID starts from point C; t_1 is the pulse duration, τ_2 the acquisition period, and T_{FID} the duration of the FID. (b) Nutation of the magnetization vector **M** around the RF magnetic field $\mathbf{B}_1$ (along the x axis) in the rotating frame of the frequency carrier during the excitation of the spin system by an X pulse; $w_{RF}t_1$ is the pulse flip angle. The receiver, represented by an eye, detects the projection of **M** along the y axis. $\mathbf{B}_0$ is along the z axis.

the y axis. However, the FID amplitude, also denoted by $\langle I_y(t_1)\rangle$, is related to the density operator $\rho(t_1)$ as Equation (19),

$$\langle I_y(t_1)\rangle = F(t_1, \tau_2 = 0) = \mathrm{Tr}\{\rho(t_1)I_y\} \tag{19}$$

where Tr means trace. In practice, the FID is recorded with a quadrature detector. The complex spectral line intensity and the density operator are related by Equation (20):

$$\langle I_+(t_1)\rangle = \langle I_x(t_1) + iI_y(t_1)\rangle = \mathrm{Tr}\{\rho(t_1)I_+\} \tag{20}$$

Therefore, knowledge of the density operator allows us to predict the complex spectral line intensity and the dynamics of the spin system as usual (see section 3).

2.2.1 *Effect of the First-order Quadrupole Interaction on the Spectrum*

Two examples are used to illustrate the effects of $H_Q^{(1)}$ on the spectrum. The spectrum of ^{27}Al ($I = \frac{5}{2}$) from a single

crystal of α-Al_2O_3 consists of five lines (Figure 3a); the central line is in the middle of four satellite lines,[29] which means that the dominant interaction is $H_Q^{(1)}$. Figure 3(b) is the spectrum of two single crystals. As the central lines of the two crystals remain at w_L, they co-add, giving an intense line. In contrast, the two sets of four satellite lines are separated due to different orientations of $\mathbf{B}_0$ in the PAS of the EFG tensor for each crystal.

When the sample is a powder, there is a uniform distribution of the orientations of $\mathbf{B}_0$ in each crystallite.[30] If $H_Q^{(1)}$ is the dominant interaction, the contributions of all crystallites co-add, giving a sharp central line and a broad powder pattern of satellite lines. Figure 4 (spectrum a) shows the case of ^{23}Na ($I = \frac{3}{2}$) in a powder of $NaNO_3$.[31] The powder pattern can be simulated by using the numerical procedure described in section 2.1.

In a MAS experiment, the powder is packed in a rotor whose spinning axis relative to $\mathbf{B}_0$ is at the magic angle $\theta_m = 54°44'$. In the fast condition, that is if the rotor spinning rate is much larger than the line width, $H_Q^{(1)}$ will be canceled during free precession of the spin system.[18] Otherwise rotational echoes appear in the FID and spinning sidebands in the spectrum. Spectrum (c) in Figure 4 presents the ^{23}Na ($I = \frac{3}{2}$) MAS spectrum in powdered $NaNO_3$. The shape and the spread of

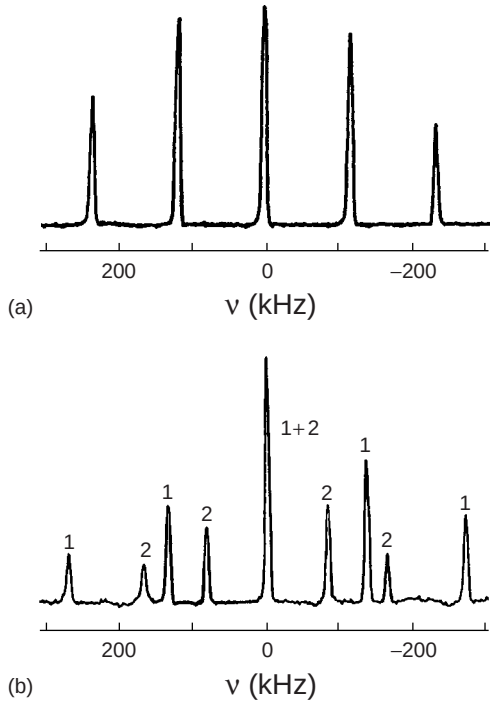

Figure 3 Effect of $H_Q^{(1)}$ on the one-pulse spectrum of ^{27}Al ($I = \frac{5}{2}$) in (a) a single crystal and (b) two crystals (denoted by 1 and 2) of α-Al_2O_3: the central lines co-add; the satellite lines are resolved.

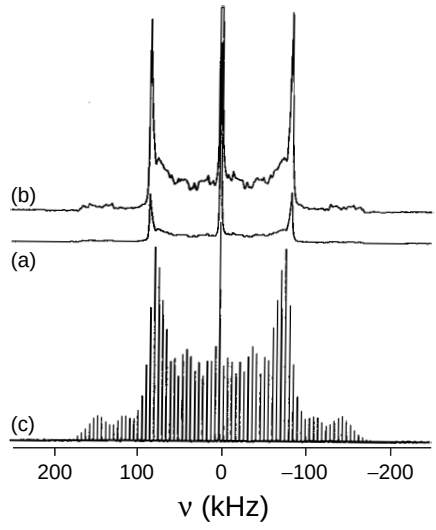

Figure 4 Effect of $H_Q^{(1)}$ on the spectrum of spin $I = \frac{3}{2}$ in a powdered sample. ^{23}Na ($I = \frac{3}{2}$) spectra of $NaNO_3$ recorded by using (a) static and (c) MAS conditions. The central line is cut off at (b) $\frac{1}{4}$ and (c) $\frac{1}{16}$ of its total height. (Reproduced by permission of Academic Press from J. Skibsted, N.C. Nielsen, H. Bildsøe, H.J. Jakobsen, *J. Magn. Reson.*, **95**, 88–117 (1991).)

these spinning sidebands enable determination of the asymmetry parameter η and the quadrupole coupling constant, respectively.

2.2.2 *Effect of the Second-order Quadrupole Interaction on the Spectrum*

When $H_Q^{(2)}$ becomes important, the central line is also shifted. For a powder, the central line is also broadened but to a lesser extent than the satellite lines, which spread over the megahertz range. As a result the powder pattern of the central line is generally observed, whereas that of the satellite lines is not. The shape of the central-transition powder pattern depends on the asymmetry parameter η, as shown by the spectra for three ^{139}La ($I = \frac{7}{2}$) salts in Figure 5(a–c).[32] Under static conditions, the second-order quadrupole shift of the central line with respect to w_L is given by Equations (21–24):[11]

$$w_{-1/2,1/2}^{(2)\text{static}} = -\frac{1}{6w_L}\left[\frac{3e^2qQ}{2I(2I-1)\hbar}\right]^2 \left\{I(I+1) - \frac{3}{4}\right\} \times \{A(\alpha,\eta)\cos^4\beta + B(\alpha,\eta)\cos^2\beta + C(\alpha,\eta)\} \quad (21)$$

$$A(\alpha,\eta) = -\tfrac{27}{8} + \tfrac{9}{4}\eta\cos 2\alpha - \tfrac{3}{8}(\eta\cos 2\alpha)^2 \quad (22)$$

$$B(\alpha,\eta) = \tfrac{30}{8} - \tfrac{1}{2}\eta^2 - 2\eta\cos 2\alpha + \tfrac{3}{4}(\eta\cos 2\alpha)^2 \quad (23)$$

$$C(\alpha,\eta) = -\tfrac{3}{8} + \tfrac{1}{3}\eta^2 - \tfrac{1}{4}\eta\cos 2\alpha - \tfrac{3}{8}(\eta\cos 2\alpha)^2 \quad (24)$$

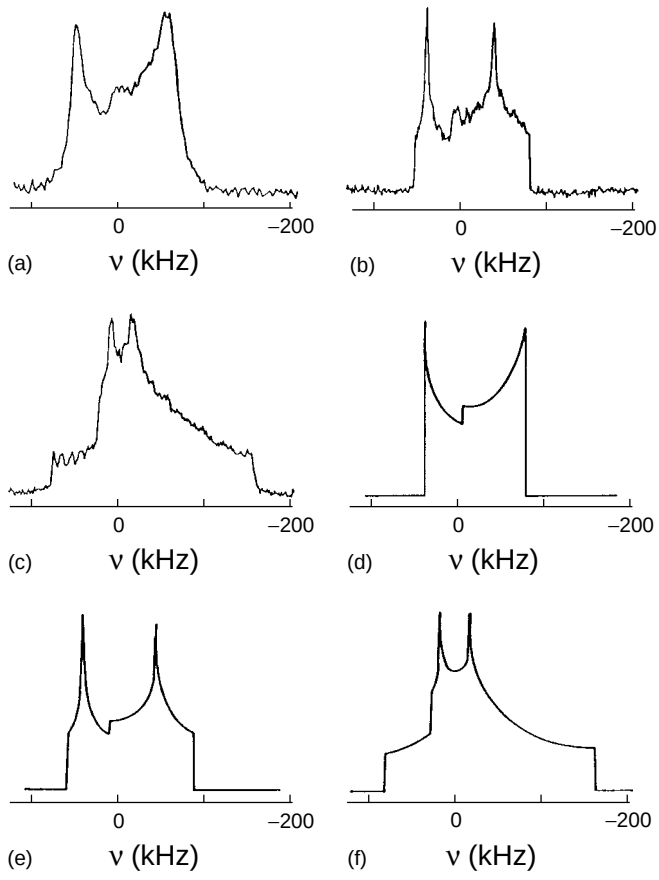

Figure 5 Effect of $H_Q^{(2)}$ on the static central line of a powder sample. ^{139}La ($I = \frac{7}{2}$) spectra of (a) $La(OH)_3$ with $\eta = 0.05$, (b) $LaCl_3$ ca. $6H_2O$ with $\eta = 0.40$, and (c) $La(NO_3)_3 \cdot 6H_2O$ with $\eta = 0.80$. The corresponding simulated spectra are shown in (d), (e), and (f), respectively. These spectra are the Fourier transform of half of the Hahn echo. (Reproduced by permission of The Royal Society of Chemistry from B. Herreros, P.P. Man, J.-M. Manoli, J. Fraissard, *J. Chem. Soc., Chem. Commun.*, 464–466 (1992).)

This shift is inversely proportional to w_L (see Equation 21). The central-transition powder pattern can be simulated by the angular part of Equations (21–24) using the procedure described in section 2.1. The limits are $\{-\frac{2}{3}(1+\eta), \frac{1}{24}(3+\eta)^2\}$ which become $\{-\frac{4}{3}, \frac{2}{3}\}$ when $\eta = 1$. Figure 5(d–f) are the simulated spectra.

Figure 6 shows the powder patterns of ^{59}Co ($I = \frac{7}{2}$) in $Na_3Co(NO_2)_6$ whose line width decreases when the strength of $\mathbf{B}_0$ increases.[33] However, above 11 T the dominant interaction becomes the chemical shift anisotropy whose contribution increases with the strength of $\mathbf{B}_0$.

When the rotor spinning axis is at the angle $\theta_r (\neq \theta_m)$ relative to $\mathbf{B}_0$, the experiment is called variable-angle spinning (VAS).[34] In the fast condition, the second-order quadrupole shift of the central line with respect to w_L is

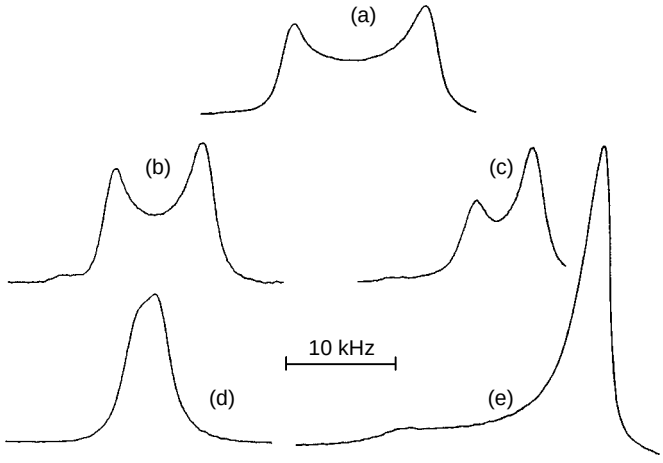

Figure 6 Effect of the strength of $\mathbf{B}_0$ on the central-transition powder pattern characterized by $H_Q^{(2)}$ on ^{59}Co ($I = \frac{7}{2}$) spectra of polycrystalline sodium hexanitrocobaltate(III) $Na_3Co(NO_2)_6$ in different $\mathbf{B}_0$: (a) 4.7, (b) 5.9, (c) 7.0, (d) 9.4, and (e) 11.7 T. (Reproduced by permission of The National Research Council of Canada from D.R. Eaton, R.J. Buist, B.G. Sayer, *Can. J. Chem.*, **65**, 1332–1335 (1987).)

defined by Equations (25–28):[18]

$$\begin{aligned} w_{-1/2,1/2}^{(2)\text{fast VAS}} = {} & \frac{\Omega_Q^2}{w_L}\left\{I(I+1) - \tfrac{3}{4}\right\} \\ & \times \Big(\tfrac{1}{2}B_{0,0}(\eta) + 4\{B_{2,0}(\eta)d_{0,0}^{(2)}(\beta_1) + 2B_{2,2}(\eta) \\ & \times d_{2,0}^{(2)}(\beta_1)\cos 2\alpha_1\}P_2(\cos\theta_r) + 9\{B_{4,0}(\eta) \\ & \times d_{0,0}^{(4)}(\beta_1) + 2B_{4,2}(\eta)d_{2,0}^{(4)}(\beta_1)\cos 2\alpha_1 \\ & + 2B_{4,4}(\eta)d_{4,0}^{(4)}(\beta_1)\cos 4\alpha_1\}P_4(\cos\theta_r)\Big) \end{aligned} \tag{25}$$

$$B_{0,0}(\eta) = -\tfrac{3}{5}\left(\tfrac{1}{3}\eta^2 + 1\right), \quad B_{2,0}(\eta) = \tfrac{3}{14}\left(\tfrac{1}{3}\eta^2 - 1\right) \tag{26}$$

$$B_{2,\pm 2}(\eta) = \frac{3}{7\sqrt{6}}\eta, \quad B_{4,0}(\eta) = \tfrac{9}{70}\left(\tfrac{1}{18}\eta^2 + 1\right) \tag{27}$$

$$B_{4,\pm 2}(\eta) = \frac{3}{14\sqrt{10}}\eta, \quad B_{4,\pm 4}(\eta) = \frac{1}{4\sqrt{70}}\eta^2 \tag{28}$$

where $P_2(\cos\theta_r)$ and $P_4(\cos\theta_r)$ are Legendre polynomials (Equations 29 and 30):

$$P_2(\cos\theta_r) = \tfrac{1}{2}(3\cos^2\theta_r - 1) \tag{29}$$

$$P_4(\cos\theta_r) = \tfrac{1}{8}(35\cos^4\theta_r - 30\cos^2\theta_r + 3) \tag{30}$$

The Euler angles α_1 and β_1 are those of the rotor in the PAS of the EFG tensor. In Equation (25), we can replace Ω_Q^2/w_L by Equation (31).

$$\frac{\Omega_Q^2}{w_L} = \frac{1}{6w_L}\left[\frac{3e^2qQ}{2I(2I-1)\hbar}\right]^2\left[\frac{2}{3}\right] \tag{31}$$

The VAS central-transition powder pattern can be simulated by using Equations (25–31) and the procedure described in section 2.1 with the same limits as in static experiment, that is, $\{-\frac{4}{3}, \frac{2}{3}\}$. The VAS central-transition powder pattern for $\theta_r = 0$ is identical to the static spectrum.

For MAS experiments in the fast condition, we only need to specify $\theta_r = \theta_m$, that is, $P_2(\cos\theta_r) = 0$ in Equation (25) to obtain the expression of the second-order quadrupole shift of the central line with respect to w_L, which is equivalent to the classical relationship (Equations 32–35).

$$w_{-1/2,1/2}^{(2)\text{fast MAS}} = -\frac{1}{6w_L}\left[\frac{3e^2qQ}{2I(2I-1)\hbar}\right]^2 \{I(I+1) - \tfrac{3}{4}\} \times \{D(\alpha_1,\eta)\cos^4\beta_1 + E(\alpha_1,\eta)\cos^2\beta_1 + F(\alpha_1,\eta)\} \quad (32)$$

$$D(\alpha_1,\eta) = \tfrac{21}{16} - \tfrac{7}{8}\eta\cos 2\alpha_1 + \tfrac{7}{48}(\eta\cos 2\alpha_1)^2 \quad (33)$$

$$E(\alpha_1,\eta) = -\tfrac{9}{8} + \tfrac{1}{12}\eta^2 + \eta\cos 2\alpha_1 - \tfrac{7}{24}(\eta\cos 2\alpha_1)^2 \quad (34)$$

$$F(\alpha_1,\eta) = \tfrac{5}{16} - \tfrac{1}{8}\eta\cos 2\alpha_1 + \tfrac{7}{48}(\eta\cos 2\alpha_1)^2 \quad (35)$$

In rapid conditions, the MAS central-transition powder pattern can be simulated by using the angular part of Equations (32–35), and the procedure described in section 2.1 with the limits $\{-\frac{1}{14}(1-\eta)^2, -\frac{1}{2}(1+\frac{1}{6}\eta^2)\}$. In practice, the same limits are used as in static conditions in order to compare the line widths. The central-transition powder pattern is narrowed by a factor ranging from three to four with respect to that obtained in static condition, depending on the value of η.[11]

For all experiments (static or rotating sample), the second-order quadrupole shift of the center of gravity of the central-transition powder pattern due to $H_Q^{(2)}$ (Equation 36) is[18]

$$w_{-1/2,1/2}^{(2)\text{iso}} = -\frac{3\Omega_Q^2}{10w_L}\{I(I+1) - \tfrac{3}{4}\}\left(1 + \tfrac{1}{3}\eta^2\right) \quad (36)$$

with respect to w_L. Experimentally, the center of gravity is the position that divides the integrated area of the powder pattern into two equal parts. The observed chemical shift of the center of gravity of the central-transition powder pattern $\delta_{G2}^{(obs)}$ comes from two contributions,[18] namely the isotropic chemical shift $\delta_{CS}^{(iso)}$ and $w_{-1/2,1/2}^{(2)\text{iso}}$ such that (Equation 37)

$$\delta_{G2}^{(obs)} = \delta_{CS}^{(iso)} + \frac{1}{w_c}w_{-1/2,1/2}^{(2)\text{iso}} \quad (37)$$

As $w_{-1/2,1/2}^{(2)\text{iso}} \leq 0$, the result $\delta_{CS}^{(iso)} \geq \delta_{G2}^{(obs)}$ is always true.

Figure 7 shows the MAS spectra of four- and six-coordinated ^{27}Al ($I = \frac{5}{2}$) in $Y_3Al_5O_{12}$.[35] The center of gravity of the six-coordinated Al powder pattern, whose spectrum is typical of $H_Q^{(1)}$, remains at its isotropic chemical shift position whatever the strength of $\mathbf{B}_0$. In contrast, that of the four-coordinated Al powder pattern shifts towards its isotropic chemical shift when the strength of $\mathbf{B}_0$ increases because the dominant interaction is $H_Q^{(2)}$.

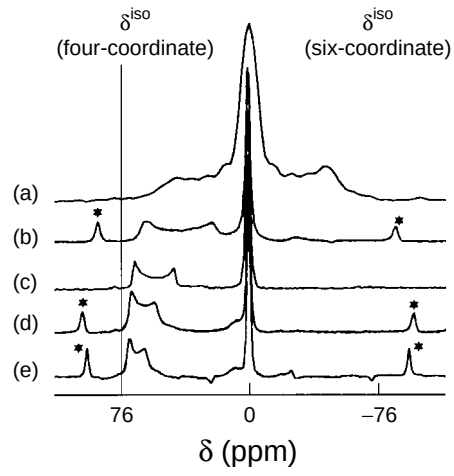

Figure 7 Effect of the strength of $\mathbf{B}_0$ on the shift and the shape of the central line characterized by $H_Q^{(1)}$ and $H_Q^{(2)}$. Spectra of four- and six-coordinate ^{27}Al ($I = \frac{5}{2}$) in $Y_3Al_5O_{12}$ crystalline powder acquired with varying $\mathbf{B}_0$: (a) 4.7, (b) 7.0, (c) 9.4, (d) 11.7, and (e) 14.1 T. Asterisked lines are spinning sidebands. The isotropic chemical shifts δ^{iso} of the four- and six-coordinate species are 76 and 0 ppm, respectively. (Reproduced by permission of Gordon and Breach Publishers, Harwood Academic, Yverdon Switzerland, from D. Massiot, B. Cote, F. Taulelle, J.-P. Coutures, *Application of NMR Spectroscopy to Cement Science*, eds. P. Colombet, A.R. Grimmer, 153–169 (1994).)

2.2.3 *Procedures used to Obtain the Spectrum*

Depending on the quadrupole coupling constant and the spin, the powder pattern is obtained by one of four procedures:

1. the Fourier transform of the FID following a single RF pulse such as those of ^{27}Al ($I = \frac{5}{2}$) in $Y_3Al_5O_{12}$ (Figure 7);
2. the Fourier transform of the second half of the echo obtained with the two-pulse sequences such as those of ^{139}La ($I = \frac{7}{2}$) in lanthanum salts (Figure 5);
3. the magnitude representation of the Fourier transform of the full echo;[36]
4. the summation of all the spectra obtained as in (2) by incrementing the carrier frequency by steps of 100 kHz, an example being the spectrum of ^{139}La ($I = \frac{7}{2}$) in $LaCoO_3$ (Figure 8).[37]

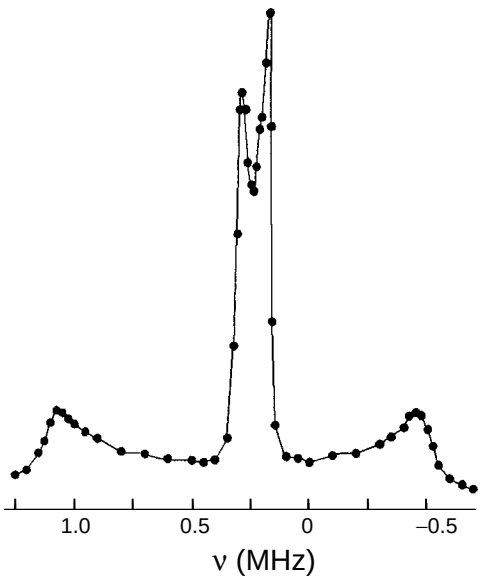

Figure 8 Use of the Hahn echo sequence for acquiring a very broad powder pattern (>200 kHz): ^{139}La ($I = \frac{7}{2}$) powder pattern of $LaCoO_3$ showing the central ($-\frac{1}{2} \leftrightarrow \frac{1}{2}$) transition (located between 0.5 and 0 MHz) and the ($\frac{1}{2} \leftrightarrow \frac{3}{2}$) and ($-\frac{3}{2} \leftrightarrow -\frac{1}{2}$) satellite transitions (located between 1.25 and −0.75 MHz). Each filled circle of the powder pattern is acquired with the Hahn echo sequence. (Reprinted from T.J. Bastow, '^{139}La NMR Characterization of La_2O_3 and La_{1-x} Sr_xMO_3 where M = Cr, Mn or Co', *Solid State NMR*, **3**, 17–22 Copyright (1994) with permission from Elsevier Science.)

3 TIME-DOMAIN RESPONSE

In limiting the discussion topics to the effects of interactions on the spectrum, the internal interactions H_{int} are restricted to secular Hamiltonians, that is, to those that commute with the Zeeman interaction. An example is the isotropic chemical shift shown in Equation (38):

$$H_{\text{CS}} = -w_{\text{c}}\delta_{\text{CS}}^{(\text{iso})} I_{\text{z}} \tag{38}$$

As the pulse duration is short (some microseconds), the rotor containing the sample appears to be static during excitation of the spin system by the RF pulses in MAS experiments. As a result, the internal interactions remain time independent. Only $H_{\text{Q}}^{(1)}$ is considered because this interaction can be much stronger than the amplitude w_{RF} of the RF pulse; thus the offset or shift interactions and $H_{\text{Q}}^{(2)}$ can be neglected. Homonuclear $H_{\text{D(II)}}$ and heteronuclear $H_{\text{D(IS)}}$ magnetic dipole–dipole interactions are also neglected during strong RF pulses. The assumptions during the RF pulses are the same for both static and MAS conditions, and both one- and two-pulse sequences (Figures 2 and 9).

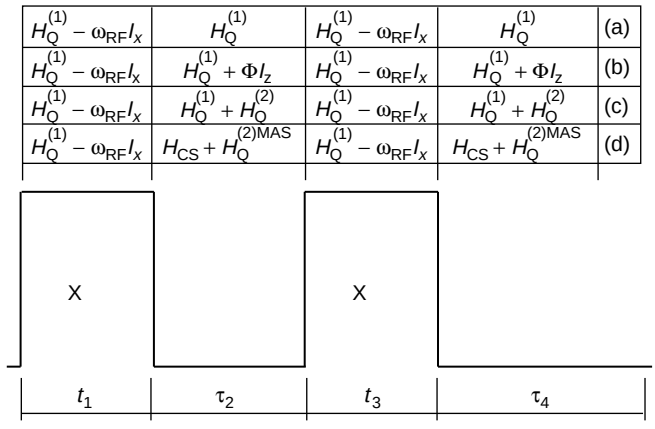

Figure 9 Interactions involved in the four periods of the two-pulse sequences discussed in this paper: the RF pulse of phase $X(-w_{\text{RF}}I_x)$, the first-order quadrupole interaction in static condition $H_{\text{Q}}^{(1)}$; the second-order quadrupole interaction in static condition $H_{\text{Q}}^{(2)}$ or in fast MAS condition $H_{\text{Q}}^{(2)\text{MAS}} \equiv H_{\text{Q}}^{(2)\text{fast MAS}}$; the isotropic chemical shift H_{CS}; and the secular part of the heteronuclear magnetic dipole-dipole interaction ΦI_z. (a) Two-pulse sequence with a short delay τ_2 or Solomon echo sequence in static condition; (b) and (c) Hahn echo sequence under static conditions; (d) Hahn echo sequence under rapid MAS conditions. The term t_1 is the first-pulse duration and t_3 is the second-pulse duration; τ_2 is the pulse separation or the experimental evolution period and τ_4 describes the acquisition period.

During free precession of the spin system, that is in the absence of RF pulses, interactions neglected during the RF pulses cannot be ignored. The simplification depends on the sample, the nuclei, and the experimental conditions (static or MAS conditions, and the strength of $\mathbf{B}_0$). The second-order quadrupole interaction can be neglected with strong $\mathbf{B}_0$ or with light nuclei. In MAS experiments, the chemical shift anisotropy, $H_{\text{Q}}^{(1)}$, as well as $H_{\text{D(IS)}}$, are canceled under rapid conditions, whereas $H_{\text{D(II)}}$ is dramatically reduced.

Throughout this article Hamiltonians H, the carrier frequency w_{c}, the Larmor frequency w_{L}, the RF pulse amplitude w_{RF}, and the line positions have been defined in angular frequency units. Only the frequency offsets are expressed in frequency units. Disregarding relaxation phenomena, the dynamics of a spin-I system submitted to two-pulse sequences is described by the density operator $\rho(t_1, \tau_2, t_3, \tau_4)$ expressed in the rotating frame. The duration t_1 is that of the first RF pulse, τ_2 is the pulse separation or experimental evolution period, t_3 is the second-pulse duration, and τ_4 the acquisition period (Figure 9). The Hamiltonian of an X pulse is given by Equation (39):

$$H_{\text{RF}} = -w_{\text{RF}} I_x \tag{39}$$

The spin dynamics from the Boltzmann equilibrium to the acquisition period are followed by using the density operators. In the high-temperature approximation, the initial state is described by the Boltzmann density operator $\rho(0) = I_z$. At the end of the first RF pulse the density operator is defined by Equation (40):

$$\rho(t_1) = \exp\{-\mathrm{i}(H_{\mathrm{int}} + H_{\mathrm{RF}})t_1\}\rho(0)\exp\{\mathrm{i}(H_{\mathrm{int}} + H_{\mathrm{RF}})t_1\} \tag{40}$$

Although the matrix representation of the secular Hamiltonian H_{int}, expressed in the eigenstates $|m\rangle$ of the Zeeman interaction H_z, is diagonal, this is not the case for H_{RF}. The matrix representation of $\exp\{-\mathrm{i}(H_{\mathrm{int}} + H_{\mathrm{RF}})t_1\}$ is the matrix whose elements are the exponential of each matrix element of $(H_{\mathrm{int}} + H_{\mathrm{RF}})$ if the latter is diagonal. Therefore, the first step is to diagonalize the matrix of $(H_{\mathrm{int}} + H_{\mathrm{RF}})$. For simplicity the matrix is denoted by the same symbol as the Hamiltonian. The eigenvalue matrix Ω, the eigenvector matrix T, and $(H_{\mathrm{int}} + H_{\mathrm{RF}})$ are related (Equation 41) as

$$\Omega = T(H_{\mathrm{int}} + H_{\mathrm{RF}})T^{\dagger} \tag{41}$$

where $T^{\dagger}$ is the complex conjugate of the transposed matrix of T. The calculation of Ω and T has been done analytically (Equation 42) for

$$H = H_{\mathrm{Q}}^{(1)} + H_{\mathrm{RF}} \tag{42}$$

in three cases: $I = \frac{3}{2}$,[38–41] $\frac{5}{2}$,[42,43] and $\frac{7}{2}$.[44–46] Otherwise we can always use a numerical procedure. The density matrix of Equation (40) becomes (Equation 43)

$$\rho(t_1) = T\exp(-\mathrm{i}\Omega t_1)T^{\dagger}\rho(0)T\exp(\mathrm{i}\Omega t_1)T^{\dagger} \tag{43}$$

After the first RF pulse, the density matrix is given by Equation (44),

$$\rho(t_1, \tau_2) = \exp(-\mathrm{i}H_{\mathrm{int}}\tau_2)\rho(t_1)\exp(\mathrm{i}H_{\mathrm{int}}\tau_2) \tag{44}$$

The effect of the second RF pulse is described by Equation (45),

$$\rho(t_1, \tau_2, t_3) = T\exp(-\mathrm{i}\Omega t_3)T^{\dagger}\rho(t_1, \tau_2)T\exp(\mathrm{i}\Omega t_3)T^{\dagger} \tag{45}$$

Finally, the density matrix during the acquisition period in a two-pulse sequence is

$$\rho(t_1, \tau_2, t_3, \tau_4) = \exp(-\mathrm{i}H_{\mathrm{int}}\tau_4)\rho(t_1, \tau_2, t_3)\exp(\mathrm{i}H_{\mathrm{int}}\tau_4) \tag{46}$$

Calculation of $\rho(t_1, \tau_2, t_3, \tau_4)$ requires 16 matrix multiplications. It would take a lot of time to perform them analytically to find out the position of the echo and the expression of the echo amplitude. Fortunately, careful analysis of $\rho(t_1, \tau_2, t_3, \tau_4)$ shows that only 12 matrix multiplications are needed (see sections 3.4.3 and 3.5.5).

3.1 One-pulse Sequence: Two-dimensional Nutation Experiment

In a one-pulse experiment, the Hamiltonian during the RF pulse is Equation (42), and that of the acquisition period is $H_{\mathrm{int}} = H_{\mathrm{Q}}^{(1)}$. First we describe the density matrix $\rho(t_1)$ at the end of the RF pulse. Then we discuss the simplest 2-D method, called nutation.

3.1.1 Spin Operators for $\mathrm{I} > \frac{1}{2}$

A matrix element of a spin operator O is denoted by $\langle r|O|c\rangle$ where the magnetic numbers r and c are half-integer numbers associated with the row and column of $\langle r|O|c\rangle$ in the matrix. We use the spin $I = \frac{5}{2}$ to describe the physical meanings of the density matrix elements at the end of the RF pulse. The extension to other spins is easy. A generalization of the three spin operators I_x, I_y, and I_z used to describe the dynamics of spin $I = \frac{1}{2}$ system are introduced for spins $I > \frac{1}{2}$: $I_x^{w,q}$, $I_y^{w,q}$, and $I_z^{w,q}$. Their matrix representations in the eigenstates of I_z are given by Equation (47).[8]

$$I_x^{w,q} = \begin{array}{c} \\ \langle w| \\ \\ \langle q| \end{array} \begin{array}{c} \begin{array}{cccc} & |w\rangle & & |q\rangle \end{array} \\ \begin{bmatrix} & & & \\ & & & \frac{1}{2} \\ & & & \\ & \frac{1}{2} & & \end{bmatrix} \end{array}$$

$$I_y^{w,q} = \begin{array}{c} \\ \langle w| \\ \\ \langle q| \end{array} \begin{array}{c} \begin{array}{cccc} & |w\rangle & & |q\rangle \end{array} \\ \begin{bmatrix} & & & \\ & & & -\frac{\mathrm{i}}{2} \\ & & & \\ & \frac{\mathrm{i}}{2} & & \end{bmatrix} \end{array}$$

$$I_z^{w,q} = \begin{array}{c} \\ \langle w| \\ \\ \langle q| \end{array} \begin{array}{c} \begin{array}{cccc} & |w\rangle & & |q\rangle \end{array} \\ \begin{bmatrix} & & & \\ & \frac{1}{2} & & \\ & & & \\ & & & -\frac{1}{2} \end{bmatrix} \end{array} \tag{47}$$

These $(2I+1)\times(2I+1)$ matrices have only two nonzero elements. From Equation (47) we deduce that if we permute the two magnetic numbers w and q, we obtain Equation (48):

$$I_x^{w,q} = I_x^{q,w}, \quad I_y^{w,q} = -I_y^{q,w}, \quad I_z^{w,q} = -I_z^{q,w} \tag{48}$$

The operators I_x, I_y, and I_z are related to those of Equation (47) as Equations (49–52):[40]

$$I_x = \sum_{w,q} \sqrt{C(w,q)} I_x^{w,q} \tag{49}$$

$$I_y = \sum_{w,q} \sqrt{C(w,q)} I_y^{w,q} \tag{50}$$

$$I_z = \sum_{w,q} C(w,q) I_z^{w,q} \tag{51}$$

$$C(w,q) = I(I+1) - wq \tag{52}$$

In particular $C(m, m+1) = \zeta^2$, with ζ being defined by Equation (15). The operator I_x is related to the X pulse (Equation 39) and the operator I_y is related to the time-domain signal (Equations 19 and 20; Figure 2). For example, $I = \frac{5}{2}$ gives Equations (53–55):

$$I_x = \sqrt{5} I_x^{\frac{5}{2},\frac{3}{2}} + \sqrt{8} I_x^{\frac{3}{2},\frac{1}{2}} + 3 I_x^{\frac{1}{2},-\frac{1}{2}} + \sqrt{8} I_x^{-\frac{1}{2},-\frac{3}{2}} + \sqrt{5} I_x^{-\frac{3}{2},-\frac{5}{2}} \tag{53}$$

$$I_y = \sqrt{5} I_y^{\frac{5}{2},\frac{3}{2}} + \sqrt{8} I_y^{\frac{3}{2},\frac{1}{2}} + 3 I_y^{\frac{1}{2},-\frac{1}{2}} + \sqrt{8} I_y^{-\frac{1}{2},-\frac{3}{2}} + \sqrt{5} I_y^{-\frac{3}{2},-\frac{5}{2}} \tag{54}$$

$$I_z = 5 I_z^{\frac{5}{2},\frac{3}{2}} + 8 I_z^{\frac{3}{2},\frac{1}{2}} + 9 I_z^{\frac{1}{2},-\frac{1}{2}} + 8 I_z^{-\frac{1}{2},-\frac{3}{2}} + 5 I_z^{-\frac{3}{2},-\frac{5}{2}} \tag{55}$$

The matrix forms are given by Equations (56–58):

$$I_x = \begin{array}{c} \\ \langle\frac{5}{2}| \\ \langle\frac{3}{2}| \\ \langle\frac{1}{2}| \\ \langle-\frac{1}{2}| \\ \langle-\frac{3}{2}| \\ \langle-\frac{5}{2}| \end{array} \begin{array}{c} \begin{array}{cccccc} |\frac{5}{2}\rangle & |\frac{3}{2}\rangle & |\frac{1}{2}\rangle & |-\frac{1}{2}\rangle & |-\frac{3}{2}\rangle & |-\frac{5}{2}\rangle \end{array} \\ \begin{bmatrix} 0 & \frac{1}{2}\sqrt{5} & 0 & 0 & 0 & 0 \\ \frac{1}{2}\sqrt{5} & 0 & \frac{1}{2}\sqrt{8} & 0 & 0 & 0 \\ 0 & \frac{1}{2}\sqrt{8} & 0 & \frac{1}{2}\sqrt{9} & 0 & 0 \\ 0 & 0 & \frac{1}{2}\sqrt{9} & 0 & \frac{1}{2}\sqrt{8} & 0 \\ 0 & 0 & 0 & \frac{1}{2}\sqrt{8} & 0 & \frac{1}{2}\sqrt{5} \\ 0 & 0 & 0 & 0 & \frac{1}{2}\sqrt{5} & 0 \end{bmatrix} \end{array} \tag{56}$$

$$I_y = \begin{array}{c} \\ \langle\frac{5}{2}| \\ \langle\frac{3}{2}| \\ \langle\frac{1}{2}| \\ \langle-\frac{1}{2}| \\ \langle-\frac{3}{2}| \\ \langle-\frac{5}{2}| \end{array} \begin{array}{c} \begin{array}{cccccc} |\frac{5}{2}\rangle & |\frac{3}{2}\rangle & |\frac{1}{2}\rangle & |-\frac{1}{2}\rangle & |-\frac{3}{2}\rangle & |-\frac{5}{2}\rangle \end{array} \\ \begin{bmatrix} 0 & \frac{-\mathrm{i}}{2}\sqrt{5} & 0 & 0 & 0 & 0 \\ \frac{\mathrm{i}}{2}\sqrt{5} & 0 & \frac{-\mathrm{i}}{2}\sqrt{8} & 0 & 0 & 0 \\ 0 & \frac{\mathrm{i}}{2}\sqrt{8} & 0 & \frac{-\mathrm{i}}{2}\sqrt{9} & 0 & 0 \\ 0 & 0 & \frac{\mathrm{i}}{2}\sqrt{9} & 0 & \frac{-\mathrm{i}}{2}\sqrt{8} & 0 \\ 0 & 0 & 0 & \frac{\mathrm{i}}{2}\sqrt{8} & 0 & \frac{-\mathrm{i}}{2}\sqrt{5} \\ 0 & 0 & 0 & 0 & \frac{\mathrm{i}}{2}\sqrt{5} & 0 \end{bmatrix} \end{array} \tag{57}$$

$$I_z = \begin{array}{c} \\ \langle\frac{5}{2}| \\ \langle\frac{3}{2}| \\ \langle\frac{1}{2}| \\ \langle-\frac{1}{2}| \\ \langle-\frac{3}{2}| \\ \langle-\frac{5}{2}| \end{array} \begin{array}{c} \begin{array}{cccccc} |\frac{5}{2}\rangle & |\frac{3}{2}\rangle & |\frac{1}{2}\rangle & |-\frac{1}{2}\rangle & |-\frac{3}{2}\rangle & |-\frac{5}{2}\rangle \end{array} \\ \begin{bmatrix} \frac{5}{2} & 0 & 0 & 0 & 0 & 0 \\ 0 & \frac{3}{2} & 0 & 0 & 0 & 0 \\ 0 & 0 & \frac{1}{2} & 0 & 0 & 0 \\ 0 & 0 & 0 & -\frac{1}{2} & 0 & 0 \\ 0 & 0 & 0 & 0 & -\frac{3}{2} & 0 \\ 0 & 0 & 0 & 0 & 0 & -\frac{5}{2} \end{bmatrix} \end{array} \tag{58}$$

The two matrices of Equations (56) and (57) can also be obtained from Equation (59):

$$I_x = \frac{1}{2}(I_+ + I_-); \quad I_y = \frac{1}{2\mathrm{i}}(I_+ - I_-) \tag{59}$$

where I_+ and I_- are the raising and the lowering operators.

3.1.2 *Meanings of the Matrix Elements of $\rho(t_1)$*

A density matrix element $\langle w|\rho(t_1)|w\rangle$ in the main diagonal of $\rho(t_1)$ is defined by

$$\langle w|\rho(t_1)|w\rangle \equiv \langle I_z^{w,-w}(t_1)\rangle = \mathrm{Tr}\{\rho(t_1) I_z^{w,-w}\} \tag{60}$$

In other words, the main diagonal matrix element $\langle w|\rho(t_1)|w\rangle$ is the spin population of the energy level $|w\rangle$. The density matrix element $\langle a|\rho(t_1)|b\rangle$ below the main diagonal is defined by Equation (61):

$$\langle a|\rho(t_1)|b\rangle \equiv \langle I_+^{b,a}(t_1)\rangle = \mathrm{Tr}\{\rho(t_1) I_x^{b,a}\} + \mathrm{i}\mathrm{Tr}\{\rho(t_1) I_y^{b,a}\} \tag{61}$$

with the magnetic numbers a and b satisfying the condition $a < b$. The density matrix element $\langle w|\rho(t_1)|q\rangle$ above the main diagonal is defined by Equation (62):

$$\langle w|\rho(t_1)|q\rangle \equiv \langle I_-^{w,q}(t_1)\rangle = \mathrm{Tr}\{\rho(t_1) I_x^{w,q}\} - \mathrm{i}\mathrm{Tr}\{\rho(t_1) I_y^{w,q}\} \tag{62}$$

with $w > q$. The density matrix elements $\langle I_{+}^{b,a}(t_1)\rangle$ and $\langle I_{-}^{w,q}(t_1)\rangle$ are the spectral intensities of off-resonance lines because they are complex quantities. More generally, the density matrix element $\langle r|\rho(t_1)|c\rangle$ is called the p-quantum (pQ) coherence where $p = r - c$ is the coherence order. The spin populations of the energy levels are zero-quantum coherences. The matrix element $\langle w|\rho(t_1)|{-w}\rangle$ in the second main diagonal (Equation 63),

$$\langle w|\rho(t_1)|{-w}\rangle \equiv -\mathrm{i}\langle I_y^{w,-w}(t_1)\rangle = -\mathrm{i}\mathrm{Tr}\{\rho(t_1)I_y^{w,-w}\} \quad (63)$$

is an imaginary quantity. As the dispersion spectral line intensity $\langle I_x^{w,-w}(t_1)\rangle = 0$, $\langle w|\rho(t_1)| - w\rangle$ is related to the spectral intensity of the on-resonance absorption line. The SQ or $\pm$1Q coherences induce an RF voltage in the RF coil. These oscillating voltages are observed as an FID that follows the RF pulse. In contrast, MQ coherences do not induce an RF voltage. As a result, no signal is detected.

Figure 10 gives the density matrix $\rho(t_1)$ at the end of an X pulse for a spin $I = \frac{5}{2}$. The first-diagonal elements above the main diagonal of the density matrix are called 1Q coherences, the second-diagonal elements above the main diagonal are called 2Q coherences, and so on. The coherences below the main diagonal elements have a negative value of p. The RF coil only detects $\pm$1Q coherences. As the pQ coherences are the complex conjugates of the $-p$Q coherences, we consider only the $-$1Q coherences during the acquisition period.

The RF pulse dephased by an angle φ_1 relative to an X pulse is an important ingredient of MQ/MAS methodology[47] (section 3.5.8). A density matrix element of a φ_1 pulse is related to that of an X pulse by

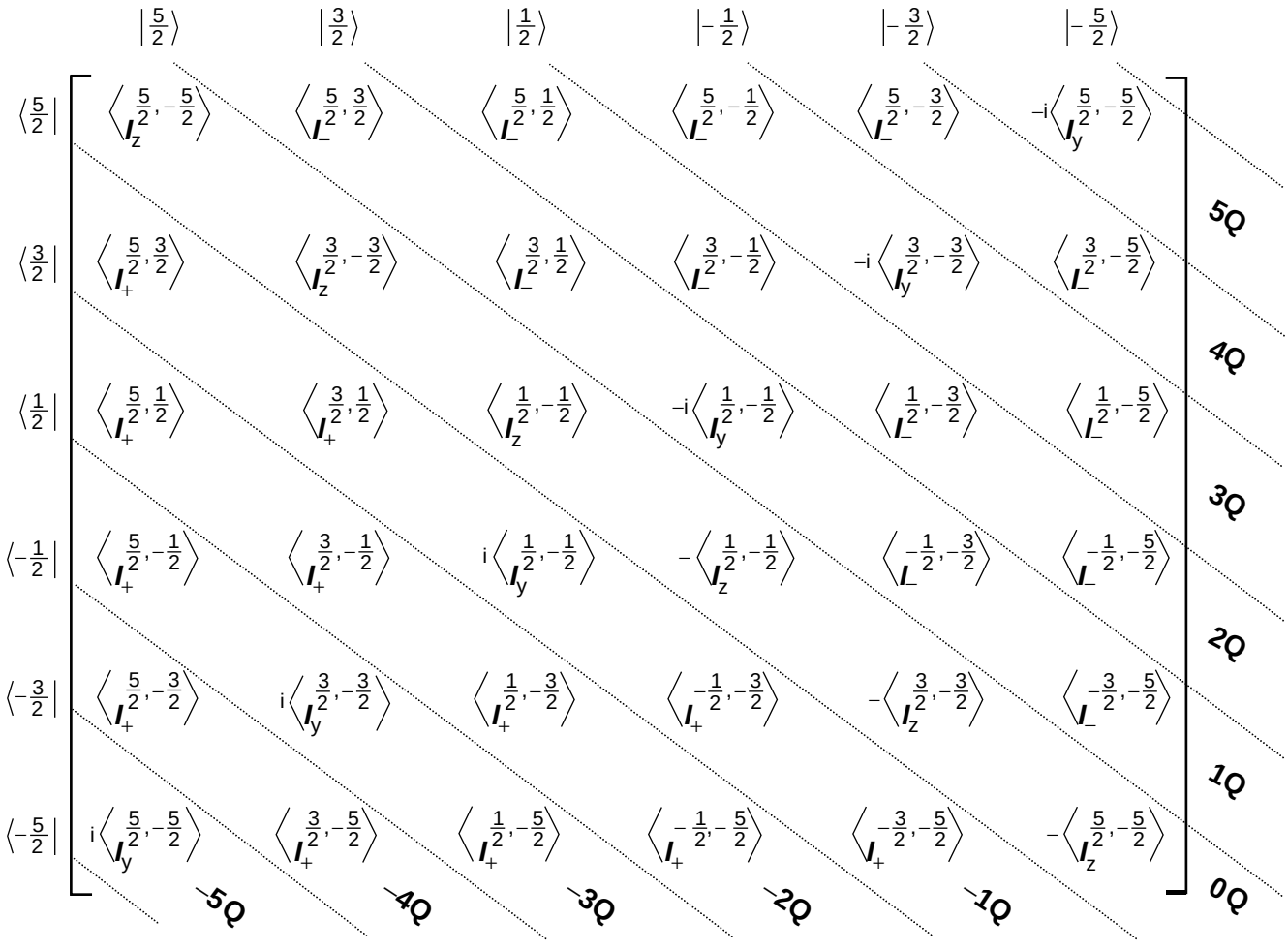

Figure 10 Definition of pQ coherences with the spin $I = \frac{5}{2}$ density matrix at the end of an X pulse, the coherence order p being an integer ranging from -5 to 5. The main diagonal contains real values, whereas the second main diagonal contains pure imaginary values. The other matrix elements are complex values. This matrix is a hermitian one. Matrix elements in the same parallel to the main diagonal have the same coherence order.

Equation (64):[48,49]

$$\langle r|\rho_{\varphi 1}(t_1)|c\rangle = \langle r|\rho(t_1)|c\rangle \exp\{-\mathrm{i}(r-c)\varphi_1\} = \langle r|\rho(t_1)|c\rangle \exp(-\mathrm{i}p\varphi_1) \quad (64)$$

In other words, when an RF pulse is dephased by an angle φ_1, a pQ coherence is dephased by $\exp(-\mathrm{i}p\varphi_1)$, whereas the zero-quantum coherences or spin populations are not affected.[8,25]

3.1.3 Spectral Line Intensity and Excitation Condition

The RF pulse amplitude w_{RF} is usually higher than internal interactions, except the quadrupole interaction. Therefore at least $H_{\mathrm{Q}}^{(1)}$ must be taken into account during the RF pulse to predict the spin dynamics. Two extreme cases appear:

1. When $w_{\mathrm{Q}} \ll w_{\mathrm{RF}}$ all the transitions are irradiated uniformly, and the excitation is known as nonselective or hard-pulse excitation because $H_{\mathrm{Q}}^{(1)}$ need not be considered during the RF pulse.
2. When $w_{\mathrm{Q}} \gg w_{\mathrm{RF}}$ two consecutive energy levels are generally irradiated, and the excitation is said to be selective because the multilevel system is reduced to a two-energy-level system whose absorption line is on resonance and $H_{\mathrm{Q}}^{(1)}$ is taken into account during the RF pulse.

For nonselective excitation, the relative spectral line intensity $I_{\mathrm{NS}}^{m+1,m}$ of the transition $(m+1 \leftrightarrow m)$ is (Equation 65)[50,51]

$$I_{\mathrm{NS}}^{m+1,m} = \frac{\zeta^2}{\sum_{m=-I}^{I-1} \zeta^2} \sin w_{\mathrm{RF}} t_1 \quad (65)$$

For selective excitation, the relative spectral line intensity $I_{\mathrm{S}}^{m+1,m}$ of the transition $(m+1 \leftrightarrow m)$ is (Equation 66)[50,51]

$$I_{\mathrm{S}}^{m+1,m} = \frac{\zeta}{\sum_{m=-I}^{I-1} \zeta^2} \sin \zeta w_{\mathrm{RF}} t_1 \quad (66)$$

Comparison of Equations (65) and (66) shows that for selective excitation the pulse duration that maximizes the relative spectral line intensity of the on-resonance transition $(m+1 \leftrightarrow m)$ is ζ times as short as that for the nonselective excitation. Furthermore, there is also a loss of relative spectral line intensity by the same factor ζ.[52] If the pulse duration is sufficiently short, Equation (67),

$$\sin \zeta w_{\mathrm{RF}} t_1 \approx \zeta w_{\mathrm{RF}} t_1 \quad (67)$$

then Equations (65) and (66) become identical:

$$I_{\mathrm{NS}}^{m+1,m} \approx I_{\mathrm{S}}^{m+1,m} \approx \frac{\zeta^2}{\sum_{m=-I}^{I-1} \zeta^2} w_{\mathrm{RF}} t_1 \quad (68)$$

Although Equation (68) has been deduced from two relationships with limited validity, it becomes valid for both $w_{\mathrm{Q}} \ll w_{\mathrm{RF}}$ and $w_{\mathrm{Q}} \gg w_{\mathrm{RF}}$ provided that the pulse duration is sufficiently short. Consequently, by continuity, Equation (68) remains valid for any ratio of $w_{\mathrm{Q}}/w_{\mathrm{RF}}$. In other words, there is a linear region in which the relative spectral line intensity is independent of w_{Q}, if the transition is excited on resonance with a short pulse duration.

Analytical expressions of the spectral line intensity for spins $I = \frac{3}{2}$,[21,53–56] $\frac{5}{2}$,[42,43] and $\frac{7}{2}$[44–46] are available for any $w_{\mathrm{Q}}/w_{\mathrm{RF}}$ ratio. Taking an internal interaction such as $H_{\mathrm{Q}}^{(1)}$ during the RF pulse is called soft-pulse excitation, which includes both nonselective and selective excitations. For spin $I = \frac{9}{2}$, a numerical procedure must be applied to solve Equations (41) and (43). The SQ spectral line intensity is not given by $\langle I_y^{w+1,w}(t_1)\rangle = \mathrm{Tr}\{\rho(t_1) I_y^{w+1,w}\}$, as shown in Figure 11 for a spin $I = \frac{5}{2}$, but by Equation (69):

$$\langle I_y^{w+1,w}(t_1)\rangle \zeta(w+1, w) = \zeta(w+1, w)\mathrm{Tr}\{\rho(t_1) I_y^{w+1,w}\} \quad (69)$$

This is because SQ coherences are detected directly by an RF coil, in contrast to MQ coherences. As the quadrupole coupling w_{Q} depends on the orientations of $\mathbf{B}_0$ with respect to the crystal, a computer is needed to average the response of the spin system over all of these orientations in order to predict the experimental FID amplitude for a powder sample.[57]

As the NMR absorption line is proportional to the number of spins, the usual way to quantify the number of spins is to compare it with a sample containing a known quantity of spins. Unfortunately, a delay of a few microseconds is necessary before acquisition of the FID. This delay, which depends on the design of the probe head, is called the dead-time of the receiver (Figure 2a). If the latter is much shorter than T_{FID}, the loss of spectral line intensity is negligible and the quantification of the number of spins is reliable. This is the case in high-resolution liquid-state NMR. In solid-state NMR, the absorption lines are broad, that is, T_{FID} is short. The dead-time of the receiver becomes a significant part of

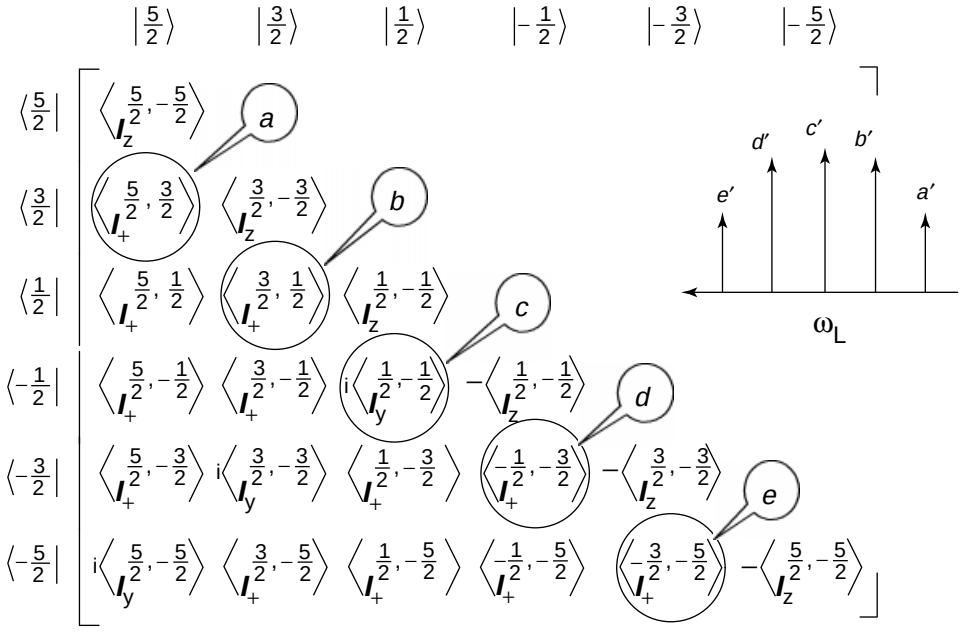

Figure 11 Directly observable coherences of spin $I = \frac{5}{2}$ at the end of an RF pulse. Only ± 1Q coherences, which are complex conjugated, are detected by an RF coil. By convention only -1Q coherences (circled) are considered. These -1Q coherences a–e are related to the area of the absorption lines ($a' \equiv \frac{3}{2} \leftrightarrow \frac{5}{2}$), ($b' \equiv \frac{1}{2} \leftrightarrow \frac{3}{2}$), ($c' \equiv -\frac{1}{2} \leftrightarrow \frac{1}{2}$), ($d' \equiv -\frac{3}{2} \leftrightarrow -\frac{1}{2}$), and ($e' \equiv -\frac{5}{2} \leftrightarrow -\frac{3}{2}$), respectively. The values of ζ (see Table 1) have not been considered here.

the FID and the quantification of the number of spins may not be reliable.

3.1.4 *One-dimensional and Two-dimensional Nutation Experiments*

The spectral line intensity is a sum of $(I + \frac{1}{2})^2$ sine functions[58] whose angular frequencies are the nutation frequencies of the spin system around the RF field $\mathbf{B}_1$. Study of the spectral line intensity versus the pulse duration is called the 1-D nutation experiment. Fourier transform of the spectral line intensity with respect to the pulse duration leads to the first 2-D NMR experiment for half-integer quadrupole spins, and is called the 2-D nutation experiment.[59] Figure 12 presents the principle of this method. The experiment consists in acquiring a series of FIDs following a single RF excitation pulse for increasing pulse duration. The F_2 dimension of the 2-D spectrum is the usual chemical shift axis, whereas the F_1 dimension is the axis of the nutation frequencies of the spin system around $\mathbf{B}_1$. The implementation is simple, but the interpretation is not obvious because the 2-D spectrum associated with a single crystallographic site may consist of several peaks along the F_1 dimension; the positions of these peaks are related to the nutation frequencies. Furthermore, only the SQ coherences generated by the RF pulse are detected by the RF coil; the MQ coherences are not. Rotary-echo and off-resonance nutations[55] have also been introduced. Simulation of experimental 2-D spectra is necessary to extract the two quadrupole parameters, namely the quadrupole coupling constant $e^2qQ/\hbar$ and the asymmetry parameter η.

3.1.4.1 Spin $\mathrm{I} = \frac{3}{2}$ Figure 13 shows the ^{23}Na ($I = \frac{3}{2}$) stacked plotted MAS spectra of a mixture of powdered NaCl and $NaNO_2$ for increasing pulse duration.[60] The powder pattern of Na in $NaNO_2$ is typical of a central line affected by $H_Q^{(2)}$, in agreement with the noncubic crystallographic structure of $NaNO_2$. However, the powder pattern of Na in NaCl has a featureless line shape. As NaCl has a cubic crystallographic structure, the EFG around the sodium site must be very small, if any. All the three absorption lines (one central and two satellite lines) are not resolved in NaCl. It is well known that the NMR spectral line intensities are related to the number of spins in the sample; the ratio of two lines should give the spin population ratio. Figure 13 clearly shows that the spectral line intensity ratio varies with the pulse duration, giving any spin population ratio. This odd behavior is in agreement with the analytical result of Figure 14(a), showing the central-line intensity of a spin $I = \frac{3}{2}$ system versus the pulse duration for several w_Q/w_{RF} ratios.[39] Only when the pulse duration is sufficiently short is the central-line intensity independent of the w_Q/w_{RF} ratio. However, for satellite transitions (Figure 14b),[60] there is no linear region where the satellite-line intensity is independent of the w_Q/w_{RF} ratio. This is because the

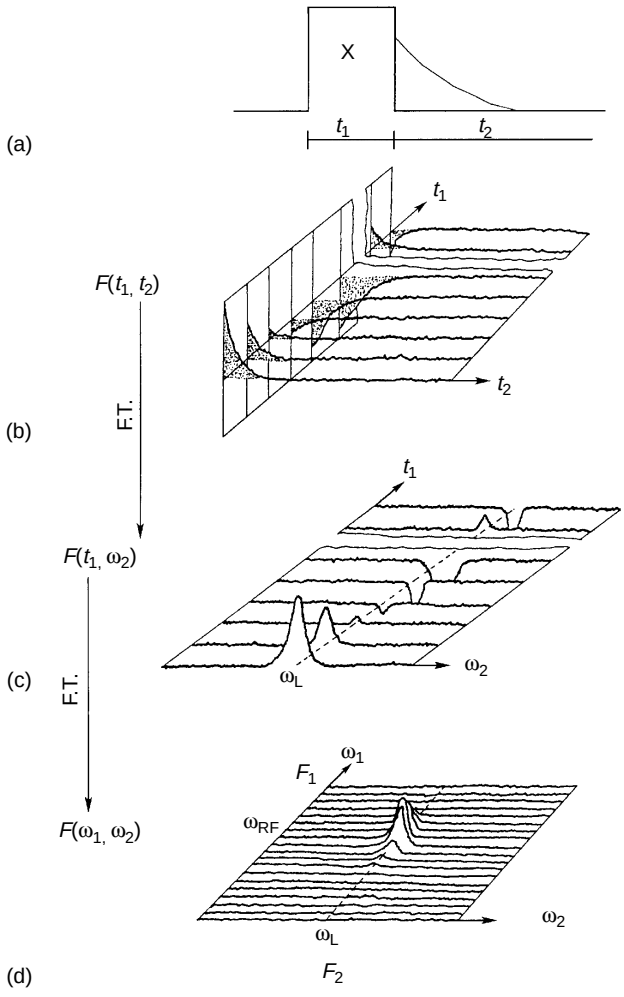

Figure 12 Nutation experiment. (a) The two time-domain parameters involved in 2-D experiments – the pulse duration t_1 describes the evolution period whereas t_2 describes the acquisition period. (b) $F(t_1, t_2)$ is a series of FID acquired with increasing pulse duration t_1. (c) $F(t_1, w_2)$, the Fourier transform of $F(t_1, t_2)$ with respect to t_2, is a series of spectra with increasing pulse duration t_1. (d) $F(w_1, w_2)$, the Fourier transform of $F(t_1, w_2)$ with respect to t_1, is the 2-D nutation spectrum. F_2 is the usual chemical shift axis and F_1 is the nutation frequency axis. The peak is located at w_{RF} in the F_1 dimension and w_L in the F_2 dimension for a spin $I = \frac{1}{2}$ system.

satellite lines become increasingly off resonance when the w_Q/w_{RF} ratio increases. The effective RF field that the spin system is submitted to differs with $\mathbf{B}_1$.

For a short pulse duration the spectral line intensity ratio does not depend on w_Q. However, precautions must be taken to ensure that the spectral line intensity ratio is that of the spin populations. For example in Figure 15,[59,60] the molar ratio of $NaNO_2$ to NaCl is 6.50, whereas the ^{23}Na experimental spectral line intensity ratio is 2.50. These two ratios are very different. As the central line of the spin $I = \frac{3}{2}$ system represents 4/10 of the

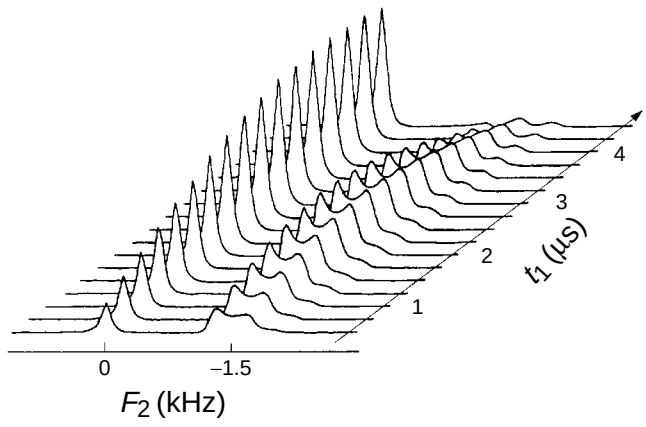

Figure 13 Effect of pulse duration on spectral line intensities: stacked plot of one-pulse ^{23}Na ($I = \frac{3}{2}$) MAS spectra in a mixture of powdered NaCl (line at 0 kHz) and $NaNO_2$ (line at −1.5 kHz) versus the pulse duration t_1, with a recycle delay $D_0 = 60$ s.

full spectrum (see Table 1), multiplying the experimental spectral line intensity ratio by 10/4 indeed gives the spin population ratio.

The main problem in quantifying the spin population is not only the application of a short pulse duration but also the identification of the nature of a featureless line shape (a central line or the full spectrum). One way to proceed with this is to study its behavior with respect to the pulse duration and compare it with the simulation. If the quadrupole coupling constant is relatively small, all the spectral line intensities should be detected.

Figure 16 shows the ^{23}Na 2-D nutation MAS spectrum of the same mixture of NaCl and $NaNO_2$.[61] Peak B is the 2-D line of $NaNO_2$, whereas peaks A and A′ are those of NaCl. The latter two peaks are located at w_{RF} and $2w_{RF}$, respectively, along the nutation axis. Peak B is located at $2w_{RF}$ because $\zeta = 2$ for $I = \frac{3}{2}$ (Table 1). The positions of peaks A and B are in agreement with the strength of the EFG around the sodium nuclei in the two compounds. The EFG around sodium nuclei in NaCl is nearly zero; the nutation frequency is that of a free spin not submitted to the quadrupole interaction. The nutation frequency of sodium nuclei in $NaNO_2$ is $2w_{RF}$ because the quadrupole coupling constant and therefore the quadrupole coupling is much larger than w_{RF}. Peak A′ occurs because the recycle delay D_0 in this experiment is too short compared to the spin–lattice relaxation time T_1 of sodium nuclei. A fuller explanation is given in section 3.1.4.3. The ^{23}Na 2-D nutation experiment has been applied to zeolite NaA.[62]

3.1.4.2 Spin I $= \frac{5}{2}$ The spin $I = \frac{5}{2}$ is not developed here because numerous papers deal with aluminum nuclei ^{27}Al ($I = \frac{5}{2}$) in zeolites.[50,63–66] The effects of pulse duration on the central-line shape are shown in

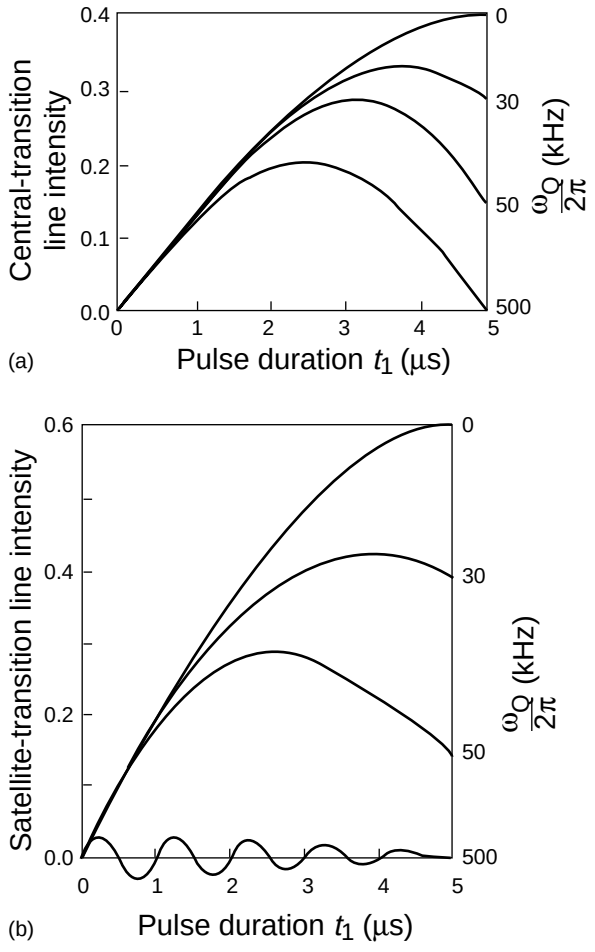

Figure 14 Calculated one-pulse spectral line intensities for a spin $I = \frac{3}{2}$ in a single crystal and submitted to $H_Q^{(1)}$ during the RF pulse versus the pulse duration t_1 for several values of the quadrupole coupling w_Q ($w_Q/(2\pi) = 0$, 30, 50, and 500 kHz), with $w_{RF}/(2\pi) = 50$ kHz: (a) the central transition ($-\frac{1}{2} \leftrightarrow \frac{1}{2}$); (b) the two satellite transitions ($\frac{1}{2} \leftrightarrow \frac{3}{2}$) and ($-\frac{3}{2} \leftrightarrow -\frac{1}{2}$).

Figure 17 which is the MAS central line of ^{55}Mn ($I = \frac{5}{2}$) in $KMnO_4$.[59] Only short pulse durations (<3 μs) yield undistorted MAS powder patterns in agreement with frequency-domain results.

3.1.4.3 Spin I = $\frac{7}{2}$ The FID amplitude in the steady state $\langle I_y(t_1)\rangle$ is related to that in the Boltzmann state $\langle I_z(t_1 = 0)\rangle$, the recycle delay D_0, and the spin–lattice relaxation time T_1 (Equation 70):[8,67]

$$\langle I_y(t_1)\rangle = \langle I_z(t_1 = 0)\rangle \frac{\{1 - \exp(-D_0/T_1)\} \sin w_{RF} t_1}{1 - \exp(-D_0/T_1) \cos w_{RF} t_1} \quad (70)$$

Figure 18 represents the graphs of $\langle I_y(t_1)\rangle : \langle I_z(t_1 = 0)\rangle$ versus the pulse flip angle $w_{RF}t_1$, ranging from 0 to π, for various ratios of D_0/T_1. The maximums of each curve as well as the associated pulse flip angle $w_{RF}t_1$ decrease when the D_0/T_1 ratio decreases. Only the duration of the π pulse, which yields a zero signal, does not depend on the D_0/T_1 ratio. Experimentally, the π-pulse duration is determined first with an aqueous solution, then the $\pi/2$-pulse duration is deduced by taking half the π-pulse duration.

Figure 19(a) represents, in magnitude, the Fourier transform of Equation (70) with respect to the pulse duration, for various D_0/T_1 ratios. It shows peaks

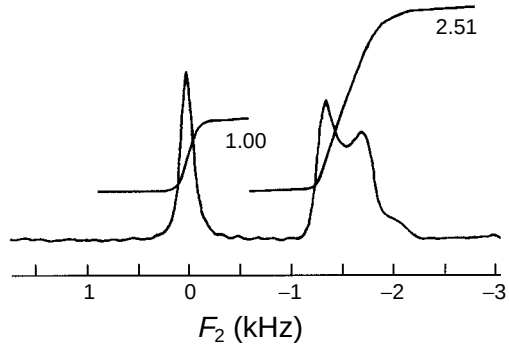

Figure 15 Quantification of spin populations with a short pulse duration $t_1 = 0.25$ μs: one-pulse ^{23}Na ($I = \frac{3}{2}$) MAS spectrum and the integrated area in a mixture of powdered NaCl (line at 0 kHz) and $NaNO_2$ (line at −1.5 kHz) with $D_0 = 60$ s. The molar ratio $NaNO_2$/NaCl is 6.50.

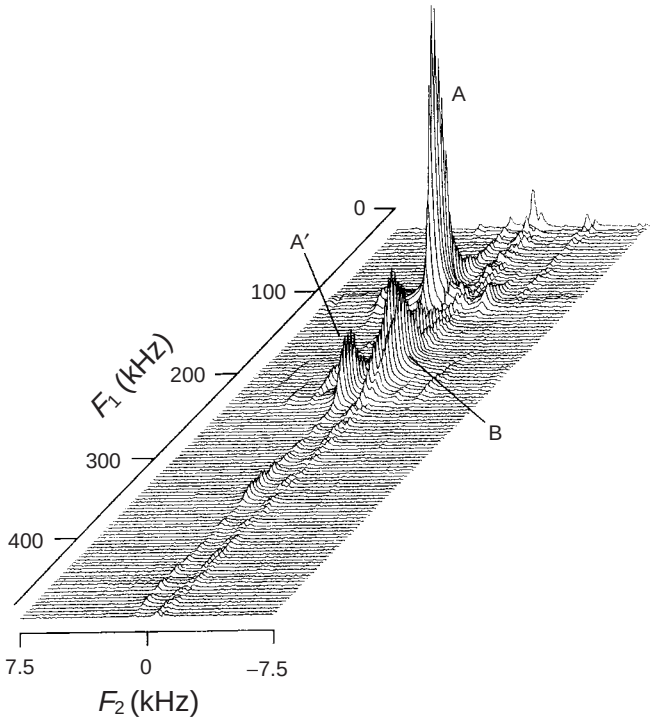

Figure 16 ^{23}Na ($I = \frac{3}{2}$) 2-D nutation MAS spectrum (magnitude mode) in a mixture of powdered NaCl (peaks A and A′) and $NaNO_2$ (peak B) with $D_0 = 5$ s.

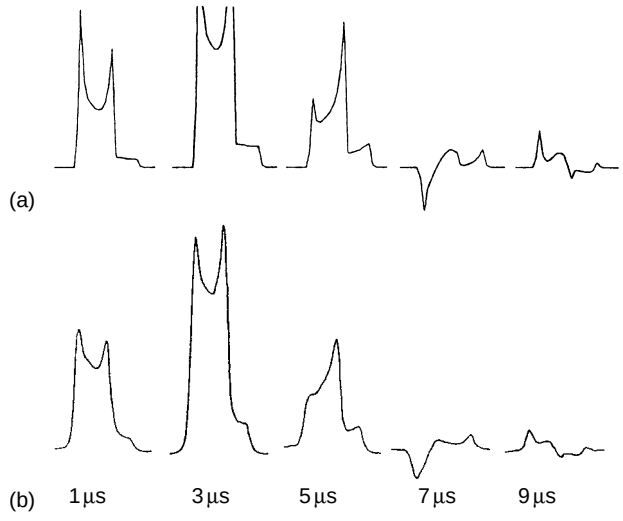

Figure 17 Effect of pulse duration on the central-line shape: (a) simulated and (b) experimental one-pulse MAS spectra of ^{55}Mn ($I = \frac{5}{2}$) in powdered $KMnO_4$ for several pulse durations $t_1 = 1$, 3, 5, 7, and 9 μs. (Reproduced by permission of The American Physical Society from A. Samoson, E. Lippmaa, *Phys. Rev. B*, **28**, 6567–6570 (1983).)

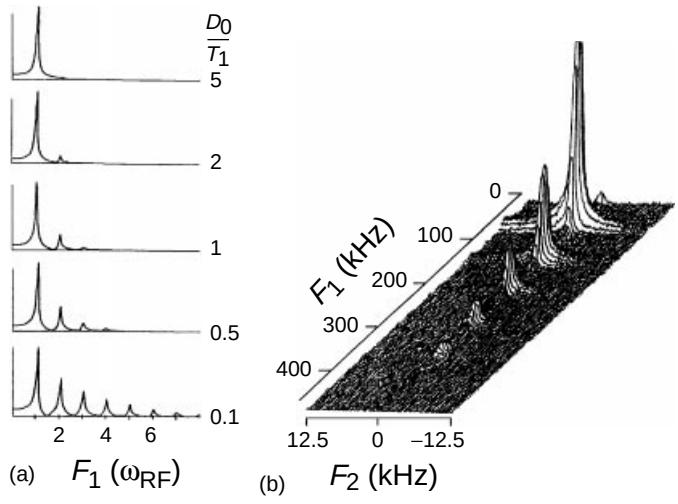

Figure 19 Effect of the recycle delay D_0 on the 2-D nutation spectrum. (a) Fourier transform of Equation (70) or curves in Figure 18 for several D_0/T_1 ratios (5, 2, 1, 0.5, and 0.1). (b) The ^{133}Cs ($I = \frac{7}{2}$) 2-D nutation spectrum (magnitude mode) in powdered CsCl, with $D_0 = 30$ s.

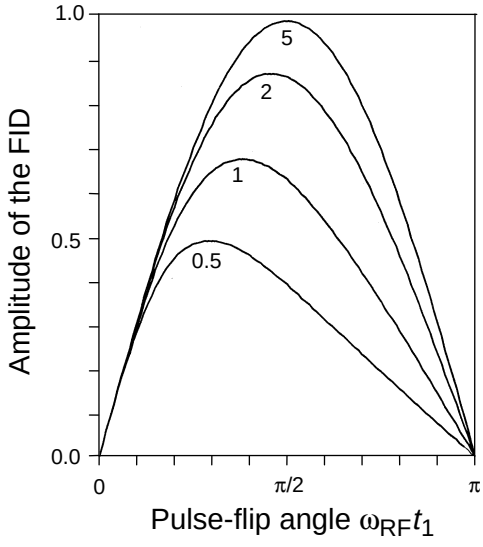

Figure 18 Effect of the recycle delay D_0 on the FID amplitude or the area of the corresponding absorption line: calculated FID amplitude in an aqueous solution versus the pulse flip angle $w_{RF}t_1$ for various D_0/T_1 ratios (5, 2, 1, and 0.5), where T_1 is the spin–lattice relaxation time.

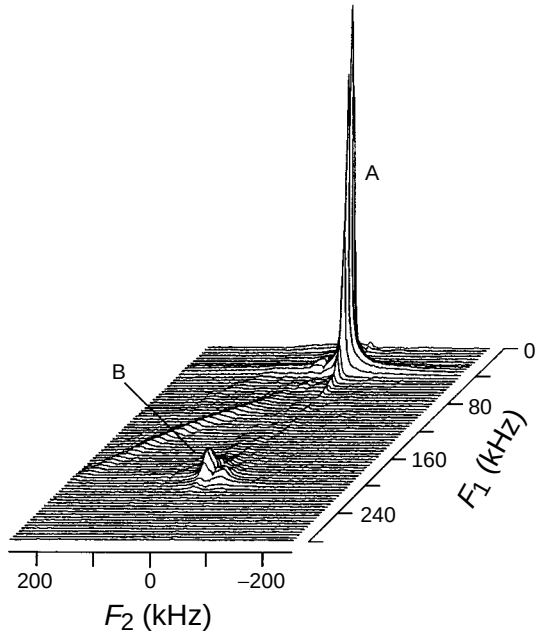

Figure 20 ^{93}Nb ($I = \frac{9}{2}$) 2-D nutation spectrum (magnitude mode) in a mixture of powdered NbO_2F (peak A) and $LiNbO_3$ (peak B) under static conditions with $D_0 = 0.1$ s.

at manifolds of w_{RF}. The number of peaks increases when the D_0/T_1 ratio decreases. We have checked this spin–lattice relaxation effect with cesium nuclei ^{133}Cs ($I = \frac{7}{2}$) in a powdered CsCl (Figure 19b). By comparing the two graphs of Figure 19, the spin–lattice relaxation time of cesium is estimated to be about 300 s.

3.1.4.4 Spin $I = \frac{9}{2}$ The largest stable nuclear spin for NMR is $I = \frac{9}{2}$. The nucleus most studied is niobium ^{93}Nb. Figure 20 shows the 2-D nutation spectrum of ^{93}Nb in a mixture of powdered $LiNbO_3$ and NbO_2F.[68] The crystallographic structure of NbO_2F is cubic, whereas that of $LiNbO_3$ is rhombohedral. Peak A corresponds to

NbO_2F and peak B to $LiNbO_3$. In the nutation frequency axis, peak A is located at w_{RF}, whereas peak B is at $5w_{RF}$ ($\zeta = 5$ for the central transition of a spin $I = \frac{9}{2}$). Peak A is much more intense than peak B because the latter represents only one $\frac{25}{165}$ part of the number of spins.

3.2 Composite-pulse Sequences: Spurious Signal Suppression

Spurious signals in pulsed NMR are often observed.[69] They disturb the signals in such a way that the interpretation of the spectra becomes difficult. We will focus on two kinds of spurious signals:

1. acoustic ringing from the NMR probe during the study of low gyromagnetic ratio nuclei in strong $\mathbf{B}_0$;
2. piezoelectric signals that occur when ferroelectric materials are studied in single crystal form.

This section discusses the first kind of spurious signal, postponing the second case to section 3.5.3. Figure 21(a) shows the ^{131}Xe ($I = \frac{3}{2}$) one-pulse spectra of xenon gas physisorbed in NaY zeolite, for increasing pulse durations.[70] The baselines of these spectra are so

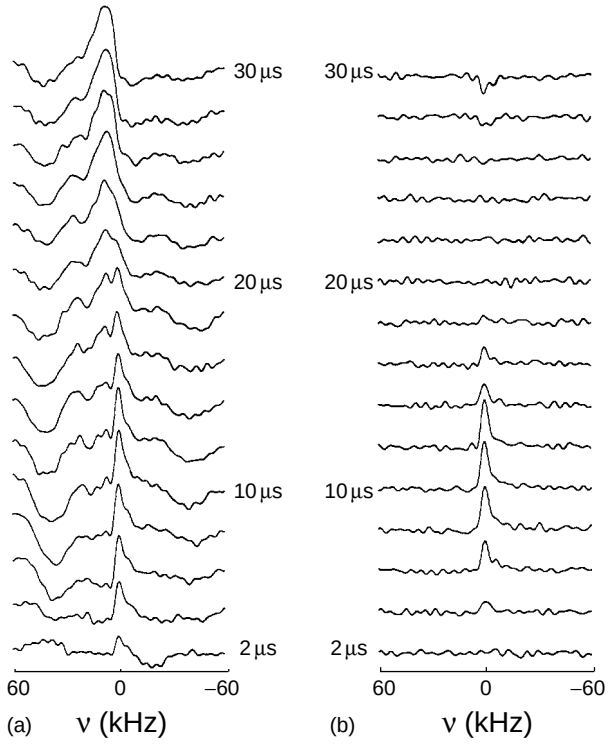

Figure 21 Suppression of the ringing signals from the NMR probe head by using a composite-pulse sequence (Figure 22 and sequence 1): ^{131}Xe ($I = \frac{3}{2}$) spectra of Xe gas physisorbed in NaY zeolite, acquired with (a) one-pulse sequence and (b) composite-pulse sequence for increasing pulse duration t_1 ranging from 2 to 30 µs by steps of 2 µs.

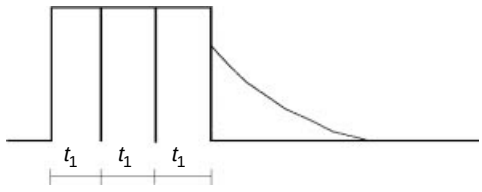

Figure 22 Composite-pulse sequence with phases given in sequence 1 cancels the ringing signals from the NMR probe head.

distorted that the ^{131}Xe signals are difficult to recognize. A composite-pulse sequence consisting of three successive RF pulses of the same duration t_1 (Figure 22) was applied with the following phases:[71]

first RF pulse:	$-X$	$-X$	$+X$	$+X$	
second RF pulse:	$+X$	$+X$	$+X$	$+X$	(sequence 1)
third RF pulse:	$+X$	$-X$	$-X$	$+X$	
receiver:	$+x$	$-x$	$+x$	$-x$	

This sequence, called sequence 1, consists of X and $-X$ pulses. Figure 21(b) presents ^{131}Xe ($I = \frac{3}{2}$) spectra acquired with the composite-pulse sequence.[70] These spectra have flattened baselines, allowing the ^{131}Xe signal to be recognized. The signal has a featureless line shape which does not allow the conclusion that the ^{131}Xe nuclei are submitted to quadrupole interaction. One response to this question is to study the behavior of the spectral line intensity versus the pulse duration t_1.

The Hamiltonian during an X pulse (Equation 71) is

$$H^{(X)} = H_Q^{(1)} - w_{RF} I_x \tag{71}$$

The Hamiltonian during a $-X$ pulse (Equation 72) is

$$H^{(-X)} = H_Q^{(1)} + w_{RF} I_x \tag{72}$$

The two Hamiltonians $H^{(X)}$ and $H^{(-X)}$ have the same eigenvalue matrix Ω, but different eigenvector matrices, denoted by T and U, respectively. The central-line intensity is given by $\zeta(\frac{1}{2}, -\frac{1}{2})\mathrm{Tr}\left(\{\rho_1(t_1) - \rho_2(t_1) + \rho_3(t_1) - \rho_4(t_1)\} I_y^{\frac{1}{2},-\frac{1}{2}}\right)$, where the signs of the four density operators $\rho_j(t_1)$ are those of the receiver phase given in sequence 1, with (Equation 73)

$$\rho_1(t_1) = T\exp(-2i\Omega t_1)T^\dagger U\exp(-i\Omega t_1)U^\dagger\rho(0)U \times \exp(i\Omega t_1)U^\dagger T\exp(2i\Omega t_1)T^\dagger \tag{73}$$

for the first acquisition of the FID. For the second FID acquisition Equation (74) applies:

$$\rho_2(t_1) = U\exp(-i\Omega t_1)U^\dagger T\exp(-i\Omega t_1)T^\dagger U \times \exp(-i\Omega t_1)U^\dagger\rho(0)U\exp(i\Omega t_1)U^\dagger T \times \exp(i\Omega t_1)T^\dagger U\exp(i\Omega t_1)U^\dagger \tag{74}$$

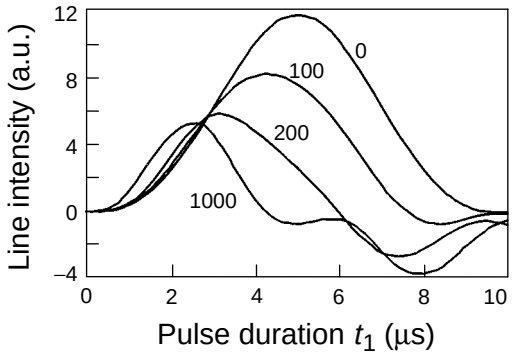

Figure 23 Calculated central-line intensities for spin $I = \frac{3}{2}$ in a powder sample, excited by the composite-pulse sequence of Figure 22, versus the pulse duration t_1 for several values of the quadrupole coupling constant $e^2qQ/\hbar$ (0, 100, 200, and 1000 kHz), with $\eta = 0$ and $w_{RF}/(2\pi) = 50$ kHz.

Equation (75) is for the third acquisition:

$$\rho_3(t_1) = U\exp(-i\Omega t_1)U^\dagger T\exp(-2i\Omega t_1)T^\dagger\rho(0)T \times \exp(2i\Omega t_1)T^\dagger U\exp(i\Omega t_1)U^\dagger \quad (75)$$

For the last acquisition Equation (76) is used:

$$\rho_4(t_1) = T\exp(-3i\Omega t_1)T^\dagger\rho(0)T\exp(3i\Omega t_1)T^\dagger \quad (76)$$

Figure 23 shows the graphs of the central-line intensities of a spin $I = \frac{3}{2}$ versus the pulse duration t_1 by taking into account $H_Q^{(1)}$ during the excitation of the spin system by the composite-pulse sequence.[70] Several quadrupole coupling constants have been used, which means that the sample is supposed to be a powder. The graph for $e^2qQ/\hbar = 0$ is bell shaped, and that for $e^2qQ/\hbar = 1$ MHz has two bell shapes of opposite signs. As with the one-pulse sequence applied to spin $I = \frac{3}{2}$ (Figure 14), the pulse duration that maximizes the spectral line intensity in the selective excitation is half that corresponding to the non-selective excitation condition. In contrast to the one-pulse sequence, there is no linear regime where the response of the spin system is proportional to the pulse duration, even for short pulse durations. Quantitative results based on spin population are not possible with this composite-pulse sequence. Furthermore, broad absorption lines are lost in the dead-time of the receiver, as in the one-pulse experiment. Spin-echo experiments are required in this case.

3.3 Two-pulse Sequences

Fitting the experimental spectral line intensity versus the pulse duration of the one-pulse sequence allows us to determine the two quadrupole parameters. However, this sequence depends only on two independent experimental parameters, the RF pulse amplitude w_{RF} and the pulse duration t_1. As w_{RF} has a limited range of variation, to increase the number of independent experimental parameters we can apply a two-pulse sequence (Figure 9a). Keeping w_{RF} at its maximum value provided by the high-power amplifier so that our assumptions remain valid (Figure 9), we have three time-domain parameters: the durations t_1 and t_3 of the two RF pulses, and the pulse separation τ_2. The graph of the spectral line intensity versus one of these three parameters, the other two being constant, allows us to extract the two quadrupole parameters. Fitting two sets of experimental spectral line intensities, obtained with different values of the two constants, should provide us with the same quadrupole parameters. In practice, we apply both one- and two-pulse sequences. As the delay required to fit the one-pulse spectral line intensities is short, we use the two quadrupole parameters provided by the one-pulse experiment as initial values to fit the two-pulse sequence data.

The internal interaction throughout the two-pulse experiment is $H_Q^{(1)}$. The analytical expressions of the central-line intensity after the second RF pulse for spins $I = \frac{3}{2}$,[21,72,73] $\frac{5}{2}$,[74] and $\frac{7}{2}$[75] in a single crystal are available. Fortunately they can be calculated numerically. As the spin–lattice relaxation is not taken into account, the pulse separation τ_2 must be short. It is of the order of magnitude of the dead-time of the receiver (typically 10–20 μs). All the density matrix elements at the end of the first RF pulse contribute to the spectral line intensity at the end of the second RF pulse. Equations (43–45) are used to calculate the central-line intensities, which are given by $\zeta(-\frac{1}{2}, \frac{1}{2})\mathrm{Tr}\left\{\rho(t_1, \tau_2, t_3)\, I_y^{\frac{1}{2}-\frac{1}{2}}\right\}$. For powder samples the procedure described in section 2.1 should be used to average the quadrupole coupling w_Q.

Figure 24 presents the ^{23}Na ($I = \frac{3}{2}$) spectra of $NaNO_3$ acquired with the two-pulse sequence for increasing second-pulse duration.[72] The Na central line has featureless line shape, irrelevant for line-shape analysis for the extraction of quadrupole parameters. Figure 25 shows the fitting of the experimental central-line intensities versus the second-pulse duration.[72] The result of the fitting for the quadrupole coupling constant is quite good.

Two-pulse sequences without pulse separation, that is, $\tau_2 = 0$, such as the spin-lock sequence[48,76] or the rotary echo sequence,[77] can also be applied to determine the quadrupole parameters from a featureless line shape.

3.4 Solomon Echo Sequences

The FIDs that have short durations T_{FID} are lost in the dead-time of the receiver following an RF pulse. This is the case of the FIDs of the satellite transitions whose powder pattern spreads far out from the central line. As the satellite-transition powder pattern provides us with the quadrupole parameters, we should apply the

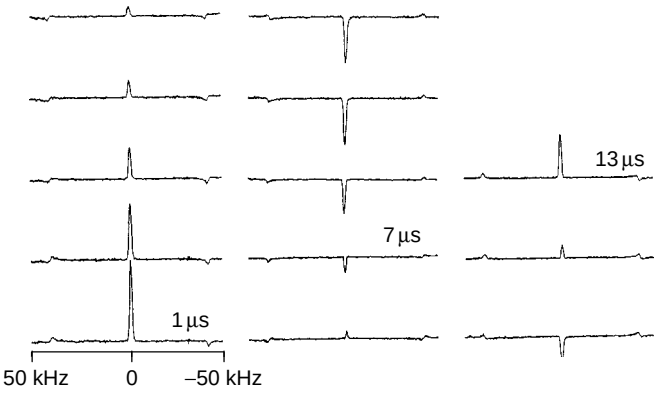

Figure 24 Two-pulse ^{23}Na ($I = \frac{3}{2}$) spectra in a powdered $NaNO_3$ for increasing second-pulse duration t_3 from 1 to 13 μs, in static condition with a short pulse separation $\tau_2 = 10$ μs and $D_0 = 60$ s. (Reproduced from P.P. Man, 'Determination of the Quadrupolar Coupling Constant in Powdered Samples with a Two In-phase RF Pulse Sequence in Solid-state NMR', *Chem. Phys. Lett.*, **168**, 227–232, Copyright (1990) with permission from Elsevier Science.)

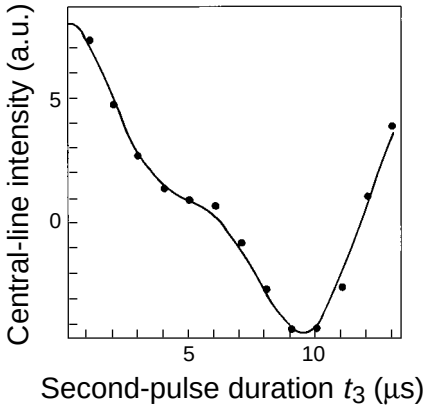

Figure 25 Experimental (filled circles) and calculated (solid line) central-line intensities of ^{23}Na ($I = \frac{3}{2}$) in a powdered $NaNO_3$ corresponding to Figure 24. The following parameters were used in the calculation: $t_1 = 4$ μs; $\tau_2 = 10$ μs; $t_3 = 1$–13 μs; $e^2qQ/\hbar = 336$ kHz; $\eta = 0$; $w_{RF}/(2\pi) = 46$ kHz (Reprinted from P.P. Man, 'Determination of the Quadrupolar Coupling Constant in Powdered Samples with a Two In-phase RF Pulse Sequence in Solid-state NMR', *Chem. Phys. Lett.*, **168**, 227–232, Copyright (1990) with permission from Elsevier Science.)

Solomon echo sequences, two-pulse sequences separated by a delay τ_2, to recover this powder pattern. These echo sequences allow us to detect the satellite transitions as echoes located far from the second RF pulse, therefore they are not affected by the dead-time of the receiver following the second RF pulse.

The positions of the Solomon echoes and the contribution of coherences generated by the first RF pulse have been already determined for the four half-integer quadrupole spins.[16] The interaction considered throughout the experiment is still $H_Q^{(1)}$ (see Figure 9a). The pulse separation τ_2 must be larger than the dead-time of the receiver but much smaller than the FID duration of the central transition T_{FID} so that the Solomon echoes can be detected. There is no Solomon echo for the central transition. The Solomon echoes are satellite-transition signals. However these echoes are superimposed on the central-transition FID following the second RF pulse. In the literature, echoes observed in these conditions for $I = \frac{3}{2}$ are called quadrupole echoes. In this paper, the term "Solomon echoes" includes those observed for $I = \frac{3}{2}$.

3.4.1 Spin I = $\frac{3}{2}$

Numerous studies have been done on spin $I = \frac{3}{2}$ systems[78,79] but the predictions are valid only in the hard-pulse or nonselective excitation condition. That is, $H_Q^{(1)}$ has been neglected during the excitation of the spin system by the RF pulses.

3.4.1.1 Hard-pulse Excitation Figure 26(a) is the oscillogram of the one-pulse experiment from ^{81}Br

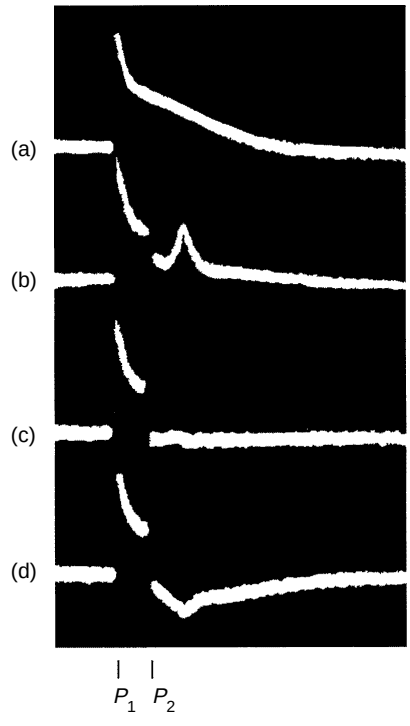

Figure 26 Oscillogram of Solomon echo from ^{81}Br ($I = \frac{3}{2}$) in KBr single crystal. The separation of the two RF pulses P_1 and P_2 is $\tau_2 = 180$ μs. (a) One X pulse with $\pi/2$ pulse flip angle, i.e. $\{X\}_{\pi/2}$; (b) the sequence $\{X\}_{\pi/2}$—τ_2—$\{Y\}_{\pi/2}$; (c) the sequence $\{X\}_{\pi/2}$—τ_2—$\{X\}_{\pi/2}$; (d) the sequence $\{X\}_{\pi/2}$—τ_2—$\{X\}_{\pi/3}$. (Reproduced by permission of Pergamon Press from G. Bonera, M. Galimberti, *Solid State Commun.*, **4**, 589–591 (1966).)

($I = \frac{3}{2}$) in KBr single crystal;[78] two FIDs are clearly observed: the long one is that of the central transition, whereas the shorter one is for the two satellite transitions. Figure 26(b–d) shows the response of the spin system to three different experimental conditions of the Solomon echo sequence. The FID following the first RF pulse is that of the satellite transitions. This observation supports the condition that the pulse separation must be shorter than T_{FID}, the duration of the central-transition FID. The observed echo, which is very sharp, is the satellite-transition signal and is located at $\tau_4 = \tau_2$. The central-transition FID following the second RF pulse is not observed in these oscillograms due to the experimental conditions, which cause confusion with the Hahn echoes also located at $\tau_4 = \tau_2$ and obtained with a pulse separation $\tau_2 \geq T_{\mathrm{FID}}$ (see section 3.5).

For two in-phase RF pulses, the echo amplitude $E_{XX}^{\frac{3}{2},\frac{1}{2}}(\tau_4 = \tau_2)$ versus the second-pulse flip angle β_3 is the expression $\frac{1}{2}(A + A')$ of Bonera and Galimberti (Equation 77):[78]

$$E_{XX}^{\frac{3}{2},\frac{1}{2}}(\tau_4 = \tau_2) = \tfrac{3}{2}\cos^2\tfrac{1}{2}\beta_3 \sin^4\tfrac{1}{2}\beta_3 - \tfrac{3}{2}\sin^2\tfrac{1}{2}\beta_3\cos^4\tfrac{1}{2}\beta_3 = -\tfrac{9}{8}\sin^2\beta_3\cos\beta_3 \qquad (77)$$

For two RF pulses in quadrature phase, the echo amplitude $E_{XY}^{\frac{3}{2},\frac{1}{2}}(\tau_4 = \tau_2)$ versus the second-pulse flip angle is (Equation 78)[78]

$$E_{XY}^{\frac{3}{2},\frac{1}{2}}(\tau_4 = \tau_2) = \tfrac{9}{8}\sin^2\beta_3 \qquad (78)$$

The thin solid line in Figure 27(a) represents the opposite of Equation (77), whereas the thin dashed line in Figure 27(b) represents the opposite of Equation (78). This complication is due to the phases of the RF pulses used, namely $\{-X\}\_\tau_2\_\{-X\}$ for Figure 27(a) and $\{-X\}\_\tau_2\_\{Y\}$ for Figure 27(b). They provide a simple explanation for Figure 26(b–d). For two in-phase RF pulses, the Solomon echo is a maximum when the second-pulse flip angle is $\pi/3$ (Figure 26d and the thin solid line in Figure 27a) and zero when the second-pulse flip angle is $\pi/2$ (Figure 26c and the thin solid line in Figure 27a). However, for two RF pulses in quadrature phase, the Solomon echo is a maximum when the second-pulse flip angle is $\pi/2$ (Figure 26b and thin dashed line in Figure 27b).

3.4.1.2 Soft-pulse Excitation The limitation of the hard pulse or nonselective excitation is removed by taking into account $H_{\mathrm{Q}}^{(1)}$ during the RF pulses. A single echo is predicted at $\tau_4 = \tau_2$,[16,80] in agreement with the results of the literature. In fact this echo represents the refocusing

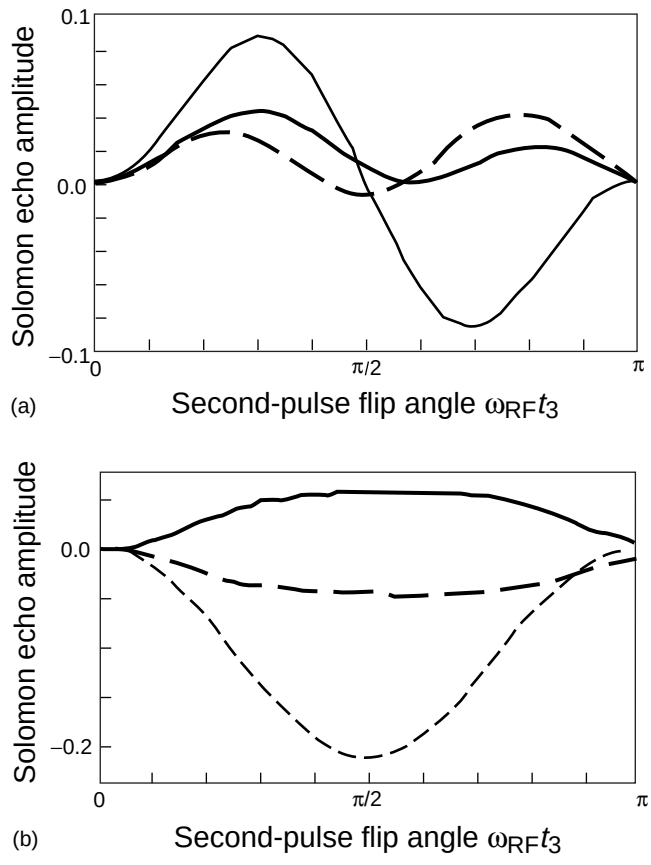

Figure 27 The $\tau_4 = \tau_2$ Solomon echo amplitudes of a spin $I = \frac{3}{2}$ versus the second-pulse flip angle $w_{\mathrm{RF}}t_3$. These echo amplitudes are associated with (a) two in-phase ($-X$, $-X$) RF pulses and (b) two RF pulses in quadrature phase: their x components for the two $w_{\mathrm{Q}}/w_{\mathrm{RF}}$ ratios (thin dashed line for $w_{\mathrm{Q}}/w_{\mathrm{RF}} = 0.001$ and thick dashed line for $w_{\mathrm{Q}}/w_{\mathrm{RF}} = 1$) and their y components (thin solid line for $w_{\mathrm{Q}}/w_{\mathrm{RF}} = 0.001$ and thick solid line for $w_{\mathrm{Q}}/w_{\mathrm{RF}} = 1$). The first-pulse flip angle $w_{\mathrm{RF}}t_1$ is $\pi/2$ and $3\pi/10$ for the two $w_{\mathrm{Q}}/w_{\mathrm{RF}}$ ratios 0.001 and 1, respectively. (Reproduced by permission of American Institute of Physics from P.P. Man, *J. Chem. Phys.*, **106**, 3908–3919 (1997).)

of satellite transitions $\left(\left\langle I_-^{\frac{3}{2},\frac{1}{2}}(t_1)\right\rangle \text{ and } \left\langle I_+^{-\frac{1}{2},-\frac{3}{2}}(t_1)\right\rangle\right)$ and ±2Q coherences $\left(\left\langle I_-^{\frac{3}{2},-\frac{1}{2}}(t_1)\right\rangle \text{ and } \left\langle I_+^{\frac{1}{2},-\frac{3}{2}}(t_1)\right\rangle\right)$ generated by the first RF pulse. The contributions of ±2Q coherences to the Solomon echo were not predicted previously, because the initial state of the spin system is $\rho(0) = I_x$, whose matrix contains ±1Q coherences only.[78] Phase cycling the first RF pulse and the receiver allows us to study these two contributions independently.

Figure 27 presents the $\tau_4 = \tau_2$ Solomon echo amplitudes of a spin $I = \frac{3}{2}$ versus the second-pulse flip angle $w_{\mathrm{RF}}t_3$.[16] These echo amplitudes are associated with two in-phase RF pulses (Figure 27a) and two RF pulses

in quadrature phase (Figure 27b). The echo amplitudes decrease when the w_Q/w_{RF} ratio increases; they can be positive or negative depending on $w_{RF}t_3$ and the w_Q/w_{RF} ratio. The graphs for $w_Q/w_{RF} = 0.001$ are in agreement with Equations (77) and (78), apart from the sign as already explained above. In fact the curves in Figure 27 are plotted by using the numerical procedure described in section 3.4.3.

3.4.2 *Spin* $I = \frac{5}{2}$

The spin $I = \frac{5}{2}$ system was first studied by Solomon[13] who predicted four echoes but observed six experimentally for ^{127}I in KI. This is because he did not consider $H_Q^{(1)}$ during the RF pulses in his calculations. They are located at $\frac{3}{2}\tau$, 2τ, 2τ, $\frac{5}{2}\tau$, 3τ, and 4τ; the echo positions were referenced to the first RF pulse. The $\frac{3}{2}\tau$, 2τ, and 3τ echoes were called allowed echoes, whereas $\frac{5}{2}\tau$ and 4τ echoes were called forbidden echoes.

3.4.2.1 Hard-pulse Excitation The echo amplitudes had been determined for the allowed echoes, which are located at $\tau_4 = \frac{1}{2}\tau_2$, τ_2, and $2\tau_2$ in our notation. For two in-phase RF pulses, the echo amplitudes of the outer-satellite ($\frac{5}{2} \leftrightarrow \frac{3}{2}$) transition versus the second-pulse flip angle β_3 are given by Equations (79) and (80):[81]

$$E_{XX}^{\frac{5}{2},\frac{3}{2}}\left(\tau_4 = \tfrac{1}{2}\tau_2\right) = 20\left\{\cos^3\tfrac{1}{2}\beta_3\sin^2\tfrac{1}{2}\beta_3\left(\cos^5\tfrac{1}{2}\beta_3 - 4\cos^3\tfrac{1}{2}\beta_3\sin^2\tfrac{1}{2}\beta_3\right) - \cos^2\tfrac{1}{2}\beta_3 \times \sin^3\tfrac{1}{2}\beta_3\left(\sin^5\tfrac{1}{2}\beta_3 - 4\cos^2\tfrac{1}{2}\beta_3 \times \sin^3\tfrac{1}{2}\beta_3\right)\right\} \tag{79}$$

$$E_{XX}^{\frac{5}{2},\frac{3}{2}}(\tau_4 = \tau_2) = 25\left(\cos^2\tfrac{1}{2}\beta_3\sin^8\tfrac{1}{2}\beta_3 - \cos^8\tfrac{1}{2}\beta_3 \times \sin^2\tfrac{1}{2}\beta_3\right) \tag{80}$$

Those of the inner-satellite ($\frac{3}{2} \leftrightarrow \frac{1}{2}$) transition versus the second-pulse flip angle β_3 are (Equations 81 and 82)[81]

$$E_{XX}^{\frac{3}{2},\frac{1}{2}}(\tau_4 = \tau_2) = 64\left\{\cos^2\tfrac{1}{2}\beta_3\sin^4\tfrac{1}{2}\beta_3\left(\tfrac{3}{2}\cos^2\tfrac{1}{2}\beta_3 - \sin^2\tfrac{1}{2}\beta_3\right)^2 - \cos^4\tfrac{1}{2}\beta_3\sin^2\tfrac{1}{2}\beta_3 \times \left(\cos^2\tfrac{1}{2}\beta_3 - \tfrac{3}{2}\sin^2\tfrac{1}{2}\beta_3\right)^2\right\} \tag{81}$$

$$E_{XX}^{\frac{3}{2},\frac{1}{2}}(\tau_4 = 2\tau_2) = E_{XX}^{\frac{5}{2},\frac{3}{2}}\left(\tau_4 = \tfrac{1}{2}\tau_2\right) \tag{82}$$

Equations (79) and (82), and the sum of Equations (80) and (81) are equivalent to the terms $E_{1/2}$, E_2, and E_1 of Solomon, respectively.[13]

For two RF pulses in quadrature phase, the echo amplitudes of the outer-satellite ($\frac{5}{2} \leftrightarrow \frac{3}{2}$) transition versus the second-pulse flip angle β_3 are given by Equations (83) and (84):[81]

$$E_{XY}^{\frac{5}{2},\frac{3}{2}}\left(\tau_4 = \tfrac{1}{2}\tau_2\right) = -20\left\{\cos^3\tfrac{1}{2}\beta_3\sin^2\tfrac{1}{2}\beta_3\left(\cos^5\tfrac{1}{2}\beta_3 - 4\cos^3\tfrac{1}{2}\beta_3\sin^2\tfrac{1}{2}\beta_3\right) + \cos^2\tfrac{1}{2}\beta_3 \times \sin^3\tfrac{1}{2}\beta_3\left(\sin^5\tfrac{1}{2}\beta_3 - 4\cos^2\tfrac{1}{2}\beta_3 \times \sin^3\tfrac{1}{2}\beta_3\right)\right\} \tag{83}$$

$$E_{XY}^{\frac{5}{2},\frac{3}{2}}(\tau_4 = \tau_2) = 25\left(\cos^2\tfrac{1}{2}\beta_3\sin^8\tfrac{1}{2}\beta_3 + \cos^8\tfrac{1}{2}\beta_3 \times \sin^2\tfrac{1}{2}\beta_3\right) \tag{84}$$

Those of the inner-satellite ($\frac{3}{2} \leftrightarrow \frac{1}{2}$) transition versus the second-pulse flip angle β_3 are (Equations 85 and 86)[81]

$$E_{XY}^{\frac{3}{2},\frac{1}{2}}(\tau_4 = \tau_2) = 64\left\{\cos^2\tfrac{1}{2}\beta_3\sin^4\tfrac{1}{2}\beta_3\left(\tfrac{3}{2}\cos^2\tfrac{1}{2}\beta_3 - \sin^2\tfrac{1}{2}\beta_3\right)^2 + \cos^4\tfrac{1}{2}\beta_3\sin^2\tfrac{1}{2}\beta_3 \times \left(\cos^2\tfrac{1}{2}\beta_3 - \tfrac{3}{2}\sin^2\tfrac{1}{2}\beta_3\right)^2\right\} \tag{85}$$

$$E_{XY}^{\frac{3}{2},\frac{1}{2}}(\tau_4 = 2\tau_2) = E_{XY}^{\frac{5}{2},\frac{3}{2}}\left(\tau_4 = \tfrac{1}{2}\tau_2\right) \tag{86}$$

3.4.2.2 Soft-pulse Excitation For any w_Q/w_{RF} ratio, six echoes have been predicted because the initial condition of the spin system is $\rho(0) = I_z$ instead of $\rho(0) = I_x$ as in the hard-pulse condition.[16,82] Three echoes, located at $\tau_4 = \tau_2$, $2\tau_2$, and $3\tau_2$, are inner-satellite transition ($\frac{1}{2} \leftrightarrow \frac{3}{2}$) signals:

- the $\tau_4 = \tau_2$ echo represents the refocusing of
  $\left\langle I_-^{\frac{3}{2},\frac{1}{2}}(t_1)\right\rangle$, $\left\langle I_+^{-\frac{1}{2},-\frac{3}{2}}(t_1)\right\rangle$, $\left\langle I_-^{\frac{3}{2},-\frac{1}{2}}(t_1)\right\rangle$, and $\left\langle I_+^{\frac{1}{2},-\frac{3}{2}}(t_1)\right\rangle$
  generated by the first RF pulse;
- the $\tau_4 = 2\tau_2$ echo represents the refocusing of
  $\left\langle I_-^{\frac{5}{2},\frac{3}{2}}(t_1)\right\rangle$, $\left\langle I_+^{-\frac{3}{2},-\frac{5}{2}}(t_1)\right\rangle$, $\left\langle I_-^{\frac{5}{2},-\frac{3}{2}}(t_1)\right\rangle$, and $\left\langle I_+^{\frac{3}{2},-\frac{5}{2}}(t_1)\right\rangle$

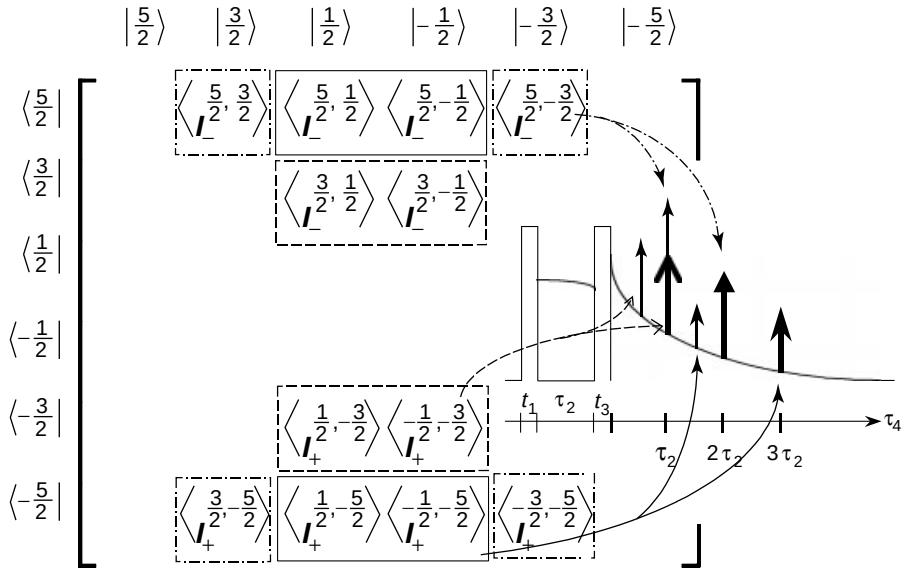

Figure 28 Coherences in the spin $I = \frac{5}{2}$ density matrix developed at the end of the first RF pulse and refocused as Solomon echoes by the second RF pulse. Echoes are represented by thick arrows for the inner-satellite transitions ($\pm\frac{1}{2} \leftrightarrow \pm\frac{3}{2}$) and thin arrows for the outer-satellite transitions ($\pm\frac{3}{2} \leftrightarrow \pm\frac{5}{2}$). Solid-line-framed coherences contribute to the $\tau_4 = 3\tau_2/2$ and $3\tau_2$ echoes. Dashed-line-framed coherences contribute to the $\tau_4 = \tau_2/2$ and τ_2 echoes. Dot-dashed-line-framed coherences contribute to the $\tau_4 = \tau_2$ and $2\tau_2$ echoes. Solomon echoes are superimposed on the central-transition FID following the second RF pulse. The pulse separation is much shorter than the duration T_{FID} of this FID.

- the $\tau_4 = 3\tau_2$ echo represents the refocusing of

$$\left\langle I_-^{\frac{5}{2},\frac{1}{2}}(t_1)\right\rangle, \left\langle I_+^{-\frac{1}{2},-\frac{5}{2}}(t_1)\right\rangle, \left\langle I_-^{\frac{5}{2},-\frac{1}{2}}(t_1)\right\rangle, \text{ and } \left\langle I_+^{\frac{1}{2},-\frac{5}{2}}(t_1)\right\rangle$$

The other three echoes, located at $\tau_4 = \frac{1}{2}\tau_2$, τ_2, and $\frac{3}{2}\tau_2$, are outer-satellite transition ($\frac{3}{2} \leftrightarrow \frac{5}{2}$) signals; the coherences involved for each echo are given in Figure 28. In fact the 12 coherences are involved for both inner- and outer-satellite transition signals. The two forbidden echoes (the $\tau_4 = \frac{3}{2}\tau_2$ and $3\tau_2$ echoes) *solely* represent the refocusing of MQ ($\pm$2Q and $\pm$3Q) coherences generated by the first RF pulse, whereas the four allowed echoes (the $\tau_4 = \frac{1}{2}\tau_2$, τ_2, and $2\tau_2$ echoes) represent *both* the refocusing of SQ ($\pm$1Q) and MQ ($\pm$2Q and $\pm$4Q) coherences generated by the first RF pulse. The main drawback of Solomon echoes for spins $I = \frac{5}{2}$, $\frac{7}{2}$, and $\frac{9}{2}$ is that the Fourier transform of the time-domain signal generates distorted spectra. Direct analysis of the echoes in the time domain is necessary.

Figure 29 is the stacked plot of Solomon echoes from ^{127}I ($I = \frac{5}{2}$) in powdered RbI for increasing second-pulse duration.[70] Indeed six echoes are observed, superimposed on the FID following the second RF pulse. In contrast, Figure 30 is the stacked plot of Solomon echoes from ^{127}I ($I = \frac{5}{2}$) in the same sample, acquired

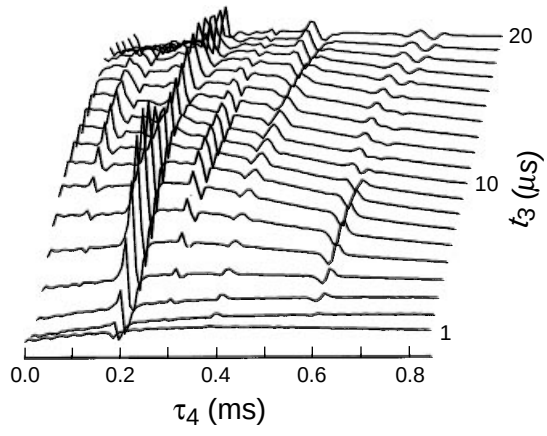

Figure 29 Stacked plot of Solomon echoes from ^{127}I ($I = \frac{5}{2}$) in powdered RbI for increasing second-pulse duration t_3 ranging from 1 to 20 μs, obtained with the $\{X\}$—τ_2—$\{X\}$ sequence and a pulse separation $\tau_2 = 0.2$ ms. Echoes in the acquisition period are located at $\tau_4 = 0.1$, 0.2, 0.3, 0.4, and 0.6 ms.

with the following sequence:[70]

first RF pulse:	X	$-X$	Y	$-Y$	
second RF pulse:	$-X$	$-X$	$-X$	$-X$	(sequence 2)
receiver:	$-y$	$-y$	y	y	

Clearly the FID following the second RF pulse has been canceled by this sequence. However, the $\tau_4 = 2\tau_2$ echo is missing.

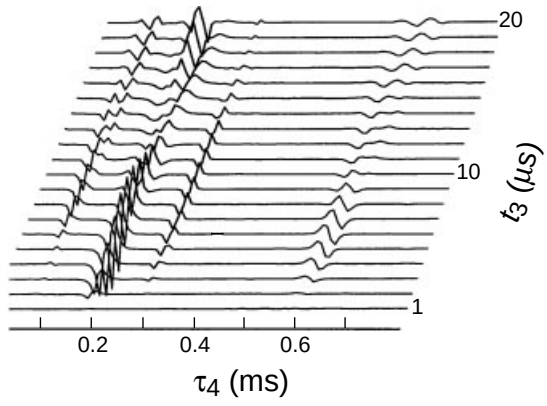

Figure 30 Cancellation of the FID following the second RF pulse in the Solomon echo sequence: stacked plot of Solomon echoes from ^{127}I ($I = \frac{5}{2}$) in powdered RbI for increasing second-pulse duration t_3 ranging from 1 to 20 μs, obtained with the phases given by sequence 2 and a pulse separation $\tau_2 = 200$ μs. Echoes in the acquisition period are located at $\tau_4 = 0.1, 0.2, 0.3$, and 0.6 ms. The $\tau_4 = 0.4$ ms echo is missing.

3.4.3 Numerical Procedure

For simplicity, we propose a numerical procedure for calculating the Solomon echo amplitude versus the second-pulse duration to optimize the experimental conditions for two specific echoes of a spin $I = \frac{5}{2}$ system. The method is applicable to other echoes and to other half-integer quadrupole spins, because all the echo positions and the contribution of the coherences generated by the first RF pulse have been already defined.[16]

Figure 31 presents the numerical procedure for calculating the complex amplitude of the inner-satellite transition Solomon echo located at $\tau_4 = 2\tau_2$ and that of the outer-satellite transition located at $\tau_4 = \tau_2$ of a spin $I = \frac{5}{2}$. Equation (43), which describes the spin dynamics during the first RF pulse, is written in the matrix form. The initial condition for the first RF pulse is the Boltzmann density matrix $\rho(0) = I_z$, which has nonzero real values only along the main diagonal. We extract the four complex spectral line intensities (a_{12}, a_{15}, a_{62}, and a_{65}) and put them into another matrix whose elements are zeros. This matrix becomes the initial condition for the second RF pulse. The complex echo amplitudes $\zeta(\frac{1}{2}, \frac{3}{2})s_{32}$ and $\zeta(\frac{3}{2}, \frac{5}{2})s_{21}$ of the final matrix are that of the inner-satellite transition located at $\tau_4 = 2\tau_2$ and that of the outer-satellite transition located at $\tau_4 = \tau_2$, respectively. These two elements, s_{32} and s_{21}, are -1Q coherences detected by an RF coil. The other elements of this final matrix are meaningless from the point of view of Solomon echoes.

3.5 Hahn Echo Sequences

As shown in the Solomon echo sequence, taking only $H_Q^{(1)}$ into account throughout the experiment does not allow us to predict an echo for the central transition. As the spin–spin relaxation times are not introduced into the density matrix, the central transition, whose frequency is that of the frequency carrier, remains on resonance throughout the sequence. This suggests that the pulse separation must be much shorter than the central-transition FID duration T_{FID}, so that the magnetization of the central transition has no time to dephase during the pulse separation. However, by definition, the satellite transitions are off resonance and have time to dephase during the pulse separation and rephase during the acquisition period.

$$\begin{pmatrix} a_{11} & \boxed{a_{12}} & a_{13} & a_{14} & \boxed{a_{15}} & a_{16} \\ a_{21} & a_{22} & a_{23} & a_{24} & a_{25} & a_{26} \\ a_{31} & a_{32} & a_{33} & a_{34} & a_{35} & a_{36} \\ a_{41} & a_{42} & a_{43} & a_{44} & a_{45} & a_{46} \\ a_{51} & a_{52} & a_{53} & a_{54} & a_{55} & a_{56} \\ a_{61} & \boxed{a_{62}} & a_{63} & a_{64} & \boxed{a_{65}} & a_{66} \end{pmatrix} = \mathrm{Texp}(-\mathrm{i}t_1\Omega)T^{\dagger} \begin{pmatrix} \frac{5}{2} & 0 & 0 & 0 & 0 & 0 \\ 0 & \frac{3}{2} & 0 & 0 & 0 & 0 \\ 0 & 0 & \frac{1}{2} & 0 & 0 & 0 \\ 0 & 0 & 0 & -\frac{1}{2} & 0 & 0 \\ 0 & 0 & 0 & 0 & -\frac{3}{2} & 0 \\ 0 & 0 & 0 & 0 & 0 & -\frac{5}{2} \end{pmatrix} \mathrm{Texp}(\mathrm{i}t_1\Omega)T^{\dagger}$$

$$\begin{pmatrix} s_{11} & s_{12} & s_{13} & s_{14} & s_{15} & s_{16} \\ s_{21} & s_{22} & s_{23} & s_{24} & s_{25} & s_{26} \\ s_{31} & s_{32} & s_{33} & s_{34} & s_{35} & s_{36} \\ s_{41} & s_{42} & s_{43} & s_{44} & s_{45} & s_{46} \\ s_{51} & s_{52} & s_{53} & s_{54} & s_{55} & s_{56} \\ s_{61} & s_{62} & s_{63} & s_{64} & s_{65} & s_{66} \end{pmatrix} = \mathrm{Texp}(-\mathrm{i}t_3\Omega)T^{\dagger} \begin{pmatrix} 0 & a_{12} & 0 & 0 & a_{15} & 0 \\ 0 & 0 & 0 & 0 & 0 & 0 \\ 0 & 0 & 0 & 0 & 0 & 0 \\ 0 & 0 & 0 & 0 & 0 & 0 \\ 0 & 0 & 0 & 0 & 0 & 0 \\ 0 & a_{62} & 0 & 0 & a_{65} & 0 \end{pmatrix} \mathrm{Texp}(\mathrm{i}t_3\Omega)T^{\dagger}$$

Figure 31 Numerical procedure for calculating the complex amplitude (s_{32}) of the inner-satellite transition ($\frac{1}{2} \leftrightarrow \frac{3}{2}$) Solomon echo located at $\tau_4 = 2\tau_2$ and that (s_{21}) of the outer-satellite transition ($\frac{3}{2} \leftrightarrow \frac{5}{2}$) Solomon echo located at $\tau_4 = \tau_2$ of a spin $I = \frac{5}{2}$ under static conditions. The initial condition for the first RF pulse is the Boltzmann density matrix containing nonzero but real diagonal elements. The initial condition for the second RF pulse is the matrix containing only four nonzero but complex elements (a_{12}, a_{15}, a_{62}, and a_{65}) provided by the density matrix of the first RF pulse. T and Ω are the eigenvector and eigenvalue matrices of the interactions involved during the pulses, namely the RF pulse and $H_Q^{(1)}$. The symbol † means transposed and complex conjugated. The two subscripts of the elements of a and s have their usual meanings, that is, the row and column of the matrix element.

To predict an echo for the central transition for pulse separation longer than T_{FID}, we include, during the free precession of the spin system, the secular part of the heteronuclear magnetic dipole–dipole interaction (Equations 87 and 88):[17]

$$H_{\mathrm{D(IS)}} = \Phi I_z \tag{87}$$

$$\Phi = \left(\frac{\mu_0}{4\pi}\right)\frac{\gamma_I\gamma_S\hbar S_z}{2(r_{I-S})^3}(1-3\cos^2\theta_{I-S}) \tag{88}$$

This is instead of the inhomogeneity of $\mathbf{B}_0$,[78,79] because the experiment is performed with a superconducting magnetic field whose homogeneity is very good for solid-state NMR. The interactions considered in this section are given in Figure 9(b). Only $H_{\mathrm{Q}}^{(1)}$ is considered during the RF pulses, an assumption that requires a strong RF pulse amplitude.

3.5.1 Hard-pulse Excitation

The $\tau_4 = \tau_2$ Hahn echo amplitude for the hard-pulse or nonselective excitation ($w_{\mathrm{Q}} \ll w_{\mathrm{RF}}$) was calculated by Mehring and Kanert.[83] Another calculation was performed by Suemitsu and Nakajo.[84] In these papers, two Y pulses were applied and the first RF pulse was a $\pi/2$ pulse so that the initial condition is $\rho(0) = I_x$. Their conventions differ with ours but the results concerning two in-phase RF pulses do not depend on this phase. A bell-like-shape echo associated with the transition ($m+1 \leftrightarrow m$) is along the x axis and its amplitude is (Equations 89 and 90)

$$E_{\mathrm{NS}}(\tau_4 = \tau_2) = C_{\mathrm{NS}}(m, I)\sin w_{\mathrm{RF}}t_1 \tag{89}$$

$$C_{\mathrm{NS}}(m, I) = -\frac{3}{2}\frac{\zeta^2}{I(I+1)(2I+1)} \times \{d^{(I)}_{m,m+1}(w_{\mathrm{RF}}t_3)\}^2 \tag{90}$$

where $d^{(I)}_{m,m+1}(w_{\mathrm{RF}}t_3)$ is the reduced Wigner rotation matrix of order I. The two subscripts m and $m+1$ locate the matrix element. Equation (90) shows that the echo has a negative amplitude. As $C_{\mathrm{NS}}(m, I)$ is an even function of $w_{\mathrm{RF}}t_3$, alternating the phase of the second RF pulse does not change the echo amplitude $E_{\mathrm{NS}}(\tau_4 = \tau_2)$. For short duration of the two RF pulses, Equation (89) becomes Equation (91):[51]

$$E_{\mathrm{NS}}(\tau_4 = \tau_2) = -\frac{3}{2}\frac{\zeta^2}{I(I+1)(2I+1)}w_{\mathrm{RF}}t_1\left\{\frac{1}{2}\zeta w_{\mathrm{RF}}t_3\right\}^2 \tag{91}$$

In fact the Hahn echo amplitude is the product of two functions:[17] the first function, called the excitation function, depends on the first-pulse duration; the second function, called the transfer or conversion function, depends on the second-pulse duration.

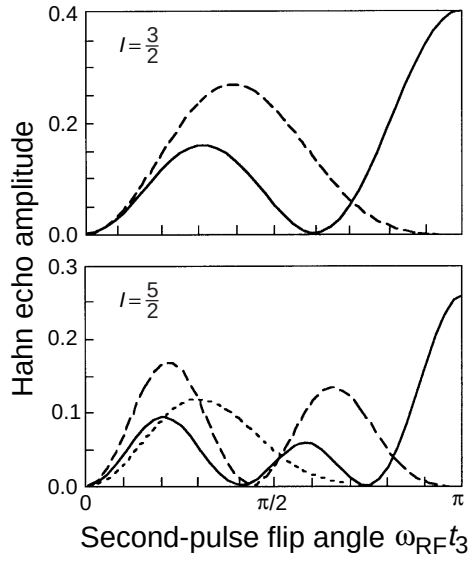

Figure 32 Graphs of the transfer function of the $\tau_4 = \tau_2$ Hahn echo amplitudes versus the second-pulse flip angle $w_{\mathrm{RF}}t_3$ for the spins $I = \frac{3}{2}$ and $\frac{5}{2}$ in the hard-pulse or non-selective excitation condition ($w_{\mathrm{Q}} \ll w_{\mathrm{RF}}$): solid line for the central-transition ($-\frac{1}{2} \leftrightarrow \frac{1}{2}$) echo; dashed line for the satellite-transition ($\pm\frac{1}{2} \leftrightarrow \pm\frac{3}{2}$) echoes; dotted line for the satellite-transition ($\pm\frac{3}{2} \leftrightarrow \pm\frac{5}{2}$) echoes. They are obtained with the numerical procedure described in section 3.5.5 or Figure 31. (Reproduced by permission of The American Physical Society from P.P. Man, *Phys. Rev. B*, **52**, 9418–9426 (1995).)

Figure 32 shows the graphs of the transfer function of the $\tau_4 = \tau_2$ Hahn echo amplitudes versus the second-pulse flip angle for the spins $I = \frac{3}{2}$ and $\frac{5}{2}$,[17,83] obtained by using the numerical procedure described in section 3.5.5. Consider the case of $I = \frac{3}{2}$. The central-transition echo has two maximum and two zero values. The satellite-transition echoes have one maximum and two zero values. All the echoes are observed when the second-pulse flip angle is smaller than $\pi/2$. For larger flip angles, mainly the central-transition echo is observed.

Figure 33 shows the Hahn echoes of ^{37}Cl ($I = \frac{3}{2}$) in a single crystal of NaCl. The echoes of the central transition as well as those of the satellite transitions are observed because the shapes of the echoes vary with the second-pulse duration.[85] These experimental data are in agreement with the predictions (see Figure 32). Despite the cubic structure of NaCl, defects in the structure generate small electric field gradients, whose quadrupole couplings are much smaller than the RF pulse amplitude.

In contrast, Figure 34 shows the Hahn echoes of ^{23}Na ($I = \frac{3}{2}$) in the same single crystal of NaCl.[85] The behavior of these echoes differs from those of chlorine. All the echoes have the same shape. Figure 34

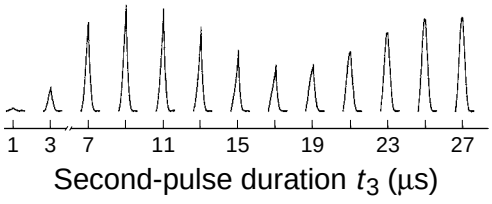

Figure 33 Experimental ^{37}Cl ($I = \frac{3}{2}$) $\tau_4 = \tau_2$ Hahn echo (in the time domain) of a single crystal of NaCl for $t_3 = 1$ to 27 μs by steps of 2 μs. These echoes are acquired with the $\{X\}$—τ_2—$\{\pm X\}$ sequence; $\tau_2 = 1$ ms, $D_0 = 100$ s, and $T_{\mathrm{FID}} = 1$ ms. The echo for $t_3 = 5$ μs is missing.

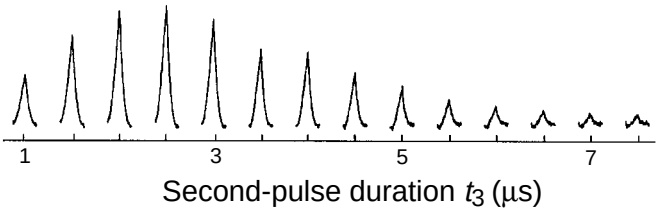

Figure 34 Experimental ^{23}Na ($I = \frac{3}{2}$) $\tau_4 = \tau_2$ Hahn echo (in the time domain) of a single crystal of NaCl for $t_3 = 1$ to 7.5 μs by steps of 0.5 μs. These echoes are acquired with the $\{X\}$—τ_2—$\{\pm X\}$ sequence; $\tau_2 = 400$ μs, $D_0 = 100$ s, and $T_{\mathrm{FID}} = 400$ μs.

is similar to that observed by Flett and Richard[86] and looks very similar to that of the satellite-transition echoes (Figure 32, dashed line in the upper figure). This discrepancy is due to the strength of the homonuclear magnetic dipole–dipole couplings with respect to that of the heteronuclear case. As the gyromagnetic ratio of the sodium nucleus is three times larger than for the chlorine nucleus, the homonuclear magnetic dipole–dipole coupling between sodium is much stronger than the heteronuclear magnetic dipole–dipole couplings between sodium and the two isotopes of chlorine. In other words, during free precession the dominant interactions are not those of Figure 9(b) for sodium. However, the heteronuclear magnetic dipole–dipole coupling of chlorine is much stronger than the homonuclear magnetic dipole–dipole coupling. Therefore chlorine is submitted to the interactions of Figure 9(b).

3.5.2 Selective Excitation

For selective excitation ($w_{\mathrm{Q}} \gg w_{\mathrm{RF}}$) the maximum of the echo amplitude is given by Equations (92) and (93):[51]

$$E_s(\tau_4 = \tau_2) = C_s(m, I) \sin \zeta w_{\mathrm{RF}} t_1 \tag{92}$$

$$C_s(m, I) = -\frac{3}{2} \frac{\zeta}{I(I+1)(2I+1)} \sin^2 \frac{1}{2} \zeta w_{\mathrm{RF}} t_3 \tag{93}$$

For a spin $I = \frac{1}{2}$ system, $\zeta = 1$ (see Table 1), and Equation (92) reduces to Equation (94):

$$E_s(\tau_4 = \tau_2) = -\sin w_{\mathrm{RF}} t_1 \sin^2 \tfrac{1}{2} w_{\mathrm{RF}} t_3 \tag{94}$$

The subscript s in Equation (94) is meaningless in the present case of $I = \frac{1}{2}$, because the latter has only two energy levels. Figure 35 is the oscillogram of proton ^{1}H ($I = \frac{1}{2}$) in glycerine showing an FID following the first RF pulse, an FID following the second RF pulse and the Hahn echo.[14] The latter two signals will be separated if the pulse separation is larger than $2T_{\mathrm{FID}}$. The Hahn echo is due to the inhomogeneity of conventional iron $\mathbf{B}_0$. With modern spectrometers, alternating the phase of the second RF pulse will cancel the FID following the second RF pulse. As a result, the pulse separation can be reduced from $2T_{\mathrm{FID}}$ to T_{FID} – the full echo is still observed but with larger amplitude than that observed when the pulse separation is $2T_{\mathrm{FID}}$. These experimental conditions remain valid for half-integer quadrupole spins. Figure 36

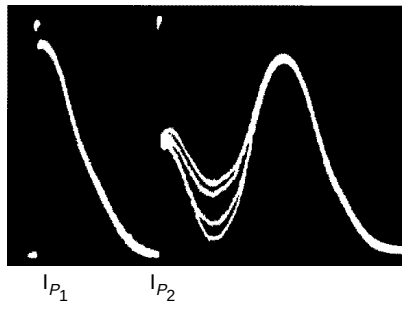

Figure 35 Proton ^{1}H ($I = \frac{1}{2}$) oscillogram in glycerine showing random interference of the FID following the second RF pulse with the $\tau_4 = \tau_2$ Hahn echo for several exposures. The two RF pulses P_1 and P_2 are phase incoherent relative to each other. (Reproduced by permission of The American Physical Society from E.L. Hahn, *Phys. Rev.*, **80**, 580–594 (1950).)

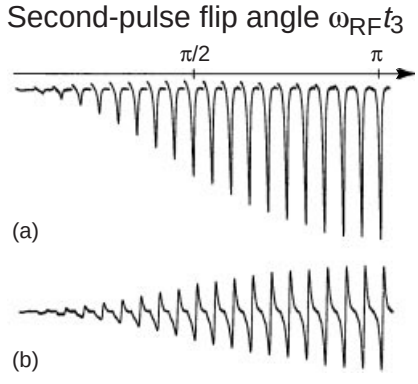

Figure 36 (a) Imaginary-part and (b) real-part echoes (in the time domain) of ^{23}Na in an aqueous solution of NaCl versus the second-pulse flip angle $w_{\mathrm{RF}} t_3$. The echoes are acquired with the $\{X\}_{\pi/2}$—τ_2—$\{X\}$ sequence.

shows the imaginary and real parts of the ^{23}Na echo in an aqueous solution of NaCl versus the second-pulse flip angle.[70] The homogeneity of the superconducting $\mathbf{B}_0$ was reduced by using the z shim. The echo amplitude increases with the second-pulse flip angle, in agreement with Equation (94).

Figure 37 is the ^{87}Rb ($I = \frac{3}{2}$) Hahn echo in powdered pyrochlore $RbNb_2O_5F$.[85] In this compound the EFG around the rubidium atoms is very strong. The variation of the echo amplitude versus the second-pulse duration is described by Equation (92).

As $C_s(m, I)$ is also an even function of $w_{RF}t_3$, alternating the phase of the second RF pulse does not change the echo amplitude $E_s(\tau_4 = \tau_2)$. As alternating the phase of the second RF pulse does not change the echo amplitude in both nonselective and selective excitations, it must be true for any excitation condition. Indeed analytical results on spin $I = \frac{3}{2}$,[85,87] $\frac{5}{2}$,[88,89] and $\frac{7}{2}$[45] support this observation.

If both pulse durations are short Equation (95) holds:

$$E_s(\tau_4 = \tau_2) = E_{NS}(\tau_4 = \tau_2) = -\frac{3}{2I(I+1)(2I+1)} w_{RF}t_1 \left(\tfrac{1}{2}\zeta^2 w_{RF}t_3\right)^2 \quad (95)$$

Therefore the echo amplitude is independent of w_Q but depends *linearly* on the first-pulse duration and *quadratically* on the second-pulse duration.[51] This excitation condition is useful for spin population determination in single crystals as well as in powders.

3.5.3 *Soft-pulse Excitation for Spin* I $= \frac{3}{2}$*: Piezoelectric Signal Suppression*

The secular part of the heteronuclear magnetic dipole–dipole interaction during free precession of the spin system and the first-order quadrupole interaction throughout the experiment are now considered (Figure 9b). For a spin $I = \frac{3}{2}$ system, three Hahn echoes are predicted and observed: two central-transition echoes located at $\tau_4 = \tau_2$ and $\tau_4 = 3\tau_2$, and the satellite-transition echoes located at $\tau_4 = \tau_2$.[17,88] The $\tau_4 = \tau_2$ Hahn echoes are the refocusing of 1Q coherences generated by the first RF pulse, namely

$$-\mathrm{i}\left\langle I_y^{\frac{1}{2},-\frac{1}{2}}(t_1)\right\rangle, \left\langle I_-^{\frac{3}{2},\frac{1}{2}}(t_1)\right\rangle, \text{ and } \left\langle I_-^{-\frac{3}{2},-\frac{1}{2}}(t_1)\right\rangle$$

The $\tau_4 = 3\tau_2$ echo is the refocusing of the 3Q coherence generated by the first RF pulse,

$$-\mathrm{i}\left\langle I_y^{\frac{3}{2},-\frac{3}{2}}(t_1)\right\rangle$$

Figure 38 is the oscillogram of the ^{53}Cr ($I = \frac{3}{2}$) echoes observed in $CdCr_2Se_4$,[90] where the positions of the two echoes are referenced to the first RF pulse, that is, 2τ and 4τ instead of τ_2 and $3\tau_2$.

Figure 39 presents the graphs of the transfer function of the central transition versus the second-pulse flip angle for several w_Q/w_{RF} ratios.[17] They are obtained by using the procedure described in section 3.5.5. The graph for $w_Q/w_{RF} = 0$ is in agreement with that of Mehring and Kanert[83] or Equation (90). The graph for $w_Q/w_{RF} = 20$ is in agreement with Equation (93).

The piezoelectric signals are observed when a ferroelectric material[91] is studied in single crystal form. In the past several methods have been used for attenuating these piezoelectric signals. The simplest but least interesting method is to grind the single crystal into powder so that the centers of gravity of the positive and negative charges are merged. Alternatively, the single crystal can

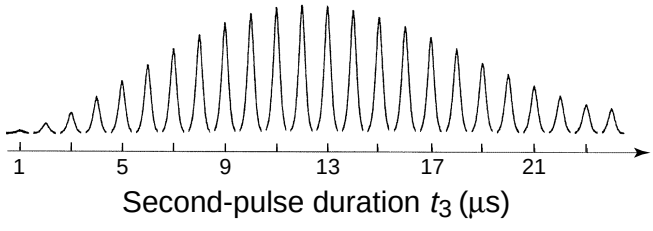

Figure 37 Experimental ^{87}Rb ($I = \frac{3}{2}$) $\tau_4 = \tau_2$ Hahn echo (in the time domain) of powdered pyrochlore $RbNb_2O_5F$ for $t_3 = 1$ to 24 μs by steps of 1 μs. These echoes are acquired with the $\{X\}$—τ_2—$\{\pm X\}$ sequence; $t_1 = 6$ μs, $\tau_2 = 300$ μs, $D_0 = 1$ s, and $T_{FID} = 300$ μs. The RF pulse amplitude is $w_{RF}/(2\pi) = 21$ kHz, corresponding to a $\pi/2$ pulse duration of 12 μs.

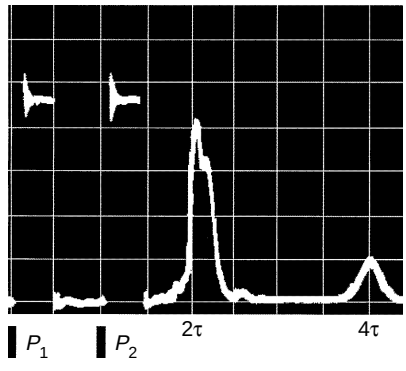

Figure 38 Oscillogram echo signals at times 2τ and 4τ of ^{53}Cr ($I = \frac{3}{2}$) in $CdCr_2Se_4$. The pulse separation is $\tau = 20$ μs. The horizontal scale is 10 μs per division. The positions of the echoes are referenced to the first RF pulse P_1. In fact they correspond to $\tau_4 = \tau_2$ and $3\tau_2$ in our notation where echo positions are referenced to the second RF pulse P_2. (Reprinted from G.N. Abelyashev, V.N. Berzhanskij, N.A. Sergeev, Y.V. Fedotov, 'Multiquantum Effects and NMR in Magnetically Ordered Substances', *Phys. Lett. A.*, **133**, 263–265, Copyright (1988) with permission from Elsevier Science.)

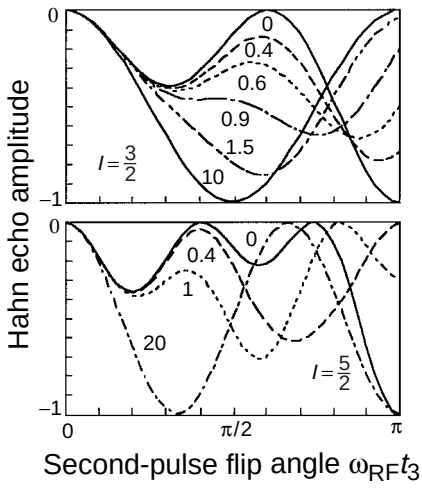

Figure 39 Graphs (for spins $I = \frac{3}{2}$ and $\frac{5}{2}$) of the transfer function of the central-transition Hahn echo amplitude versus the second-pulse flip angle $w_{RF}t_3$ for several w_Q/w_{RF} ratios (0, 0.4, 0.6, 0.9, 1, 1.5, 10, and 20). (Reproduced by permission of The American Physical Society from P.P. Man, *Phys. Rev. B*, **52**, 9418–9426 (1995).)

be put into oil, CCl_4 or paraffin to attenuate the piezoelectric signals. Shielding the sample with an extra coil inside the RF coil is also effective.[91]

Hahn echo sequences were applied to cancel these spurious signals. Five sequences were tested for the proposals. Figure 40 presents the efficiency of these sequences.[92] Clearly sequence (e) gives the best result. Sequence (a), which consists of two RF pulses of the same phase, and sequence (c), which is sequence (a) where the phase of the second RF pulse alternates, provide negative echoes. Sequence (b), which consists of two RF pulses in quadrature phase, and sequence (d), which is sequence (b) where the phase of the second RF pulse alternates, provide positive echoes. Sequence (e) is sequence (c) followed by sequence (d) whose receiver phase has opposite phase to make the echo negative so that the echoes co-add.[93]

first RF pulse:	$+X$	$+X$	$+X$	$+X$	
second RF pulse:	$+X$	$-X$	$+Y$	$-Y$	(sequence e)
receiver:	$+x$	$+x$	$-x$	$-x$	

The efficiency of sequence (e) to cancel the piezoelectric signals does not depend on the two pulse durations.[94] In fact this sequence also cancels the spurious signals generated by the NMR probe head. We have used this sequence to observe ^{131}Xe ($I = \frac{3}{2}$) physisorbed in NaY zeolite (Figure 41).[94]

3.5.4 *Soft-pulse Excitation for Spin* $I = \frac{5}{2}$

Figure 42 shows the coherences developed at the end of the first RF pulse and refocused as Hahn echoes by

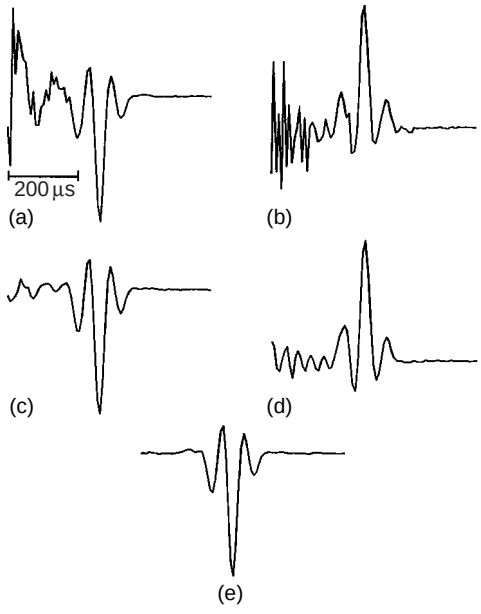

Figure 40 Suppression of the piezoelectric signals from a single crystal by using Hahn echo sequences. ^{7}Li ($I = \frac{3}{2}$) Hahn echoes (in the time domain) of a single crystal of $LiNbO_3$ acquired with the following sequences: (a) $\{X\}$—τ_2—$\{X\}$—acquisition(y); (b) $\{X\}$—τ_2—$\{Y\}$—acquisition(y); (c) $\{X\}$—τ_2—$\{\pm X\}$—acquisition(y); (d) $\{X\}$—τ_2—$\{\pm Y\}$—acquisition(y); (e) is sequence (c) followed by $\{X\}$—τ_2—$\{\pm Y\}$—acquisition($-y$); $\pm y$ is the receiver phase; $D_0 = 100$ s and $\tau_2 = 300\,\mu$s. (Reprinted from P.P. Man, 'Study of a Spin-$\frac{3}{2}$ System by a Quadrupolar-echo Sequence: Suppression of Spurious Signals', *Solid State NMR*, **1**, 149–158, Copyright (1992), with permission from Elsevier Science.)

the second RF pulse.[17] Six echoes have been predicted: three as the central-transition echoes located at $\tau_4 = \tau_2$, $3\tau_2$, and $5\tau_2$; two as the inner-satellite transition echoes located at $\tau_4 = \tau_2$ and $3\tau_2$; and one echo as the outer-satellite transition echo located at $\tau_4 = \tau_2$. These echoes are the refocusing of

$$-\mathrm{i}\left\langle I_y^{\frac{1}{2},-\frac{1}{2}}(t_1)\right\rangle, \left\langle I_-^{\frac{3}{2},\frac{1}{2}}(t_1)\right\rangle, \left\langle I_-^{\frac{5}{2},\frac{3}{2}}(t_1)\right\rangle,$$
$$-\mathrm{i}\left\langle I_y^{\frac{3}{2},-\frac{3}{2}}(t_1)\right\rangle, \left\langle I_-^{\frac{5}{2},-\frac{1}{2}}(t_1)\right\rangle, \text{and } -\mathrm{i}\left\langle I_y^{\frac{5}{2},-\frac{5}{2}}(t_1)\right\rangle$$

respectively. In practice, only the $\tau_4 = \tau_2$ Hahn echoes are observed.

Figure 43 presents the one-pulse spectra of ^{27}Al ($I = \frac{5}{2}$) in a polycrystalline sample of $KAl(SO_4)_2 \cdot 12H_2O$;[89] the satellite-transition powder patterns are distorted by the dead-time of the receiver. However, Figure 44 presents the Hahn echo spectra of ^{27}Al $\left(I = \frac{5}{2}\right)$ in the same sample;[89] the satellite-transition powder patterns are reconstructed only when the second-pulse duration is short. For longer second-pulse durations, the powder patterns differ from what is expected. In this compound, an aluminum atom is hexacoordinated to six water

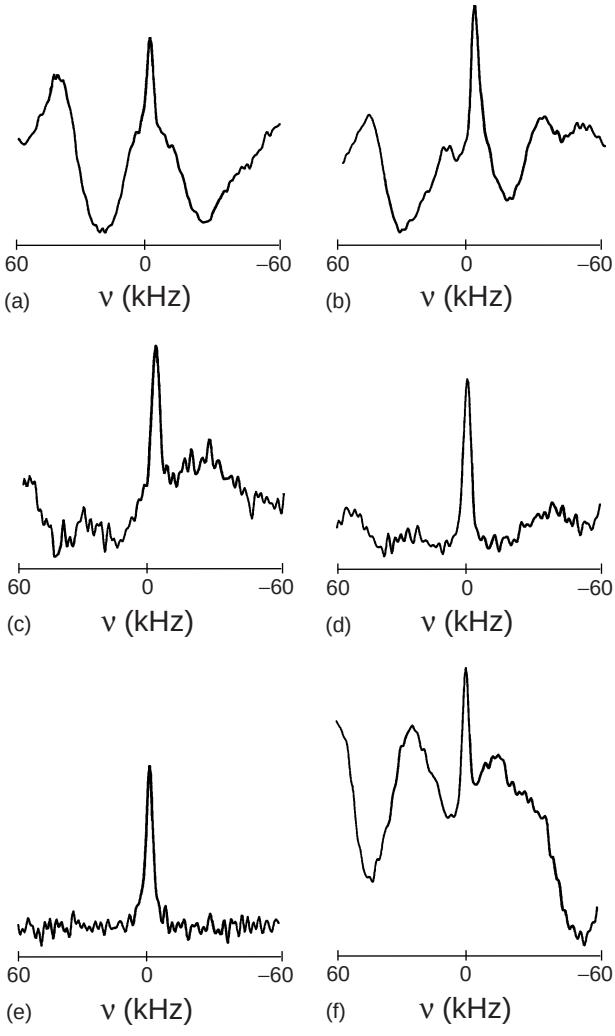

Figure 41 Suppression of the ringing signals from the NMR probe head by using Hahn echo sequences: ^{131}Xe ($I = \frac{3}{2}$) spectra of Xe gas physisorbed in NaY zeolite, acquired with one-pulse sequence (f) and Hahn echo sequences (a–e): sequences used for acquiring (a–e) are identical to those of Figure 40. (Reproduced by permission of Gordon and Breach, Harwood Academic, Yverdon Switzerland, from M.A. Hepp, P.P. Man, J. Fraissard, *Application of NMR Spectroscopy to Cement Science*, eds. P. Colombet, A.R. Grimmer, 455–466 (1994).)

molecules. The heteronuclear magnetic dipole–dipole interaction of aluminum with 12 protons is much larger than the homonuclear magnetic dipole–dipole interaction of aluminum with its surrounding aluminum atoms. In other words, the Hamiltonians (Figure 9b) required for the formation of Hahn echoes are verified for aluminum atoms in this compound.

3.5.5 *Numerical Procedure*

The Hahn echo amplitude is the product of two functions:[17] the first function, called the excitation function, depends on the first-pulse duration t_1; the second function, called the transfer or conversion function, depends on the second-pulse duration t_3. The positions of the central- and satellite-transition Hahn echoes and the coherences generated at the end of the first RF pulse and involved in the Hahn echo amplitude have been established for the four half-integer quadrupole spins.[17]

Figure 45 presents the numerical procedure for calculating the $\tau_4 = \tau_2$ Hahn echo complex amplitude (s_{43}) of the central transition in a spin $I = \frac{5}{2}$ system. The first part of this procedure concerning the first RF pulse is identical to that proposed for Solomon echoes (Figure 31). However, only one coherence or complex spectral line intensity,

$$a_{34} = -\mathrm{i}\left\langle I_{\mathrm{y}}^{\frac{1}{2},-\frac{1}{2}}(t_1)\right\rangle$$

contributes to the initial density matrix for the second RF pulse to calculate the transfer function, which is defined by $\zeta\left(\frac{1}{2}, -\frac{1}{2}\right)\mathrm{Im}(s_{43})/\mathrm{Im}(a_{34})$, where Im means the imaginary part. The other elements of the matrix s are meaningless. Figure 39 shows the graphs of the transfer function for spin $I = \frac{3}{2}$ and $\frac{5}{2}$, obtained with the numerical procedure; one important feature of these transfer functions is that they are always positive or negative, whereas Solomon echoes change sign with the second-pulse duration. For short pulse duration t_3, the transfer function is independent of the quadrupole coupling w_{Q} and varies quadratically with t_3 (see Equation 95).

3.5.6 *Any Spin* I *in a Static Sample*

The interactions considered during free precession define the nature and position of the echoes, whereas the interactions considered during the RF pulses affect the echo amplitude. However, the powder patterns are affected by the two pulse durations.

In particular, when $H_{\mathrm{Q}}^{(2)}$ is taken into account during free precession (Figure 9c), the secular term of the heteronuclear magnetic dipole–dipole interaction need not be considered because $H_{\mathrm{Q}}^{(2)}$ is an odd function of I_z (Equation 7). In other words, $H_{\mathrm{Q}}^{(2)}$ contains a term I_z (Equation 9) that allows the dephasing and the refocusing of the central-transition coherence. Dumazy and colleagues[95] have shown, in the case of $I = \frac{3}{2}$, that only the $\tau_4 = \tau_2$ Hahn echoes are observable.

So far homonuclear magnetic dipole–dipole interaction has been neglected. In fact this interaction, present in a static sample, generates other echoes,[96] which is why the samples used to illustrate theoretical results are so specific: chlorine in NaCl, rubidium in

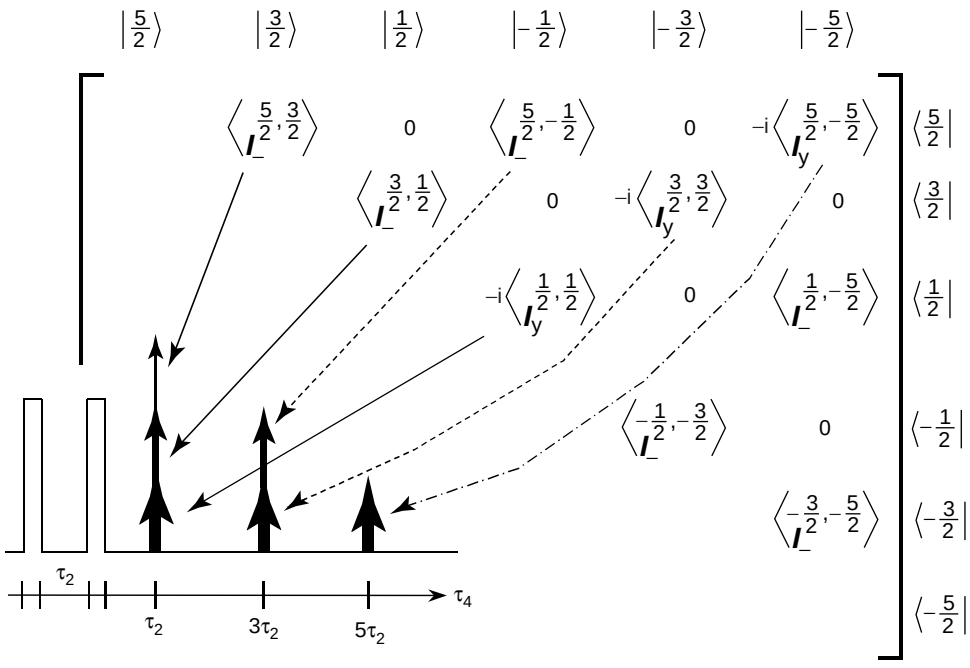

Figure 42 Coherences of the spin $I = \frac{5}{2}$ density matrix developed at the end of the first RF pulse and refocused as Hahn echoes by the second RF pulse. Echoes are represented by thick arrows for the central transition ($-\frac{1}{2} \leftrightarrow \frac{1}{2}$), medium arrows for the inner-satellite transition ($\frac{1}{2} \leftrightarrow \frac{3}{2}$), and a thin arrow for the outer-satellite transition ($\frac{3}{2} \leftrightarrow \frac{5}{2}$). Coherences and corresponding echoes located at $\tau_4 = \tau_2$, $3\tau_2$, and $5\tau_2$ are connected by arrows (solid line for 1Q, dashed line for 3Q, and dot-dashed line for 5Q). (Reproduced by permission of The American Physical Society from P.P. Man, *Phys. Rev. B*, **52**, 9418–9426 (1995).)

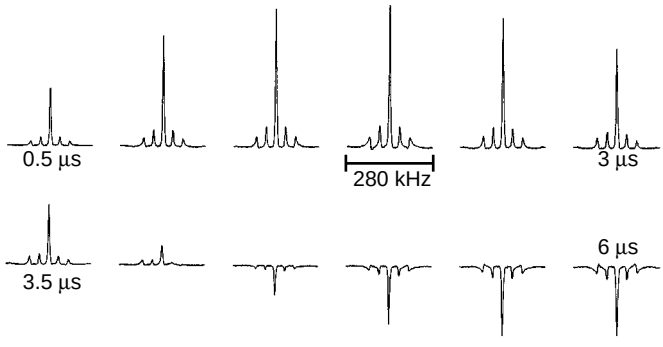

Figure 43 Effect of the dead-time of the receiver on the satellite-transition powder pattern: one-pulse spectra of ^{27}Al ($I = \frac{5}{2}$) in a polycrystalline sample of $KAl(SO_4)_2 \cdot 12H_2O$. The pulse duration t_1 increases from 0.5 to 6 μs by steps of 0.5 μs. (Reprinted from P.P. Man, E. Duprey, J. Fraissard, P. Tougne, J.-B. d'Espinose, 'Spin-$\frac{5}{2}$ Hahn Echoes in Solids', *Solid State NMR*, **5**, 181–188, Copyright (1995), with permission from Elsevier Science.)

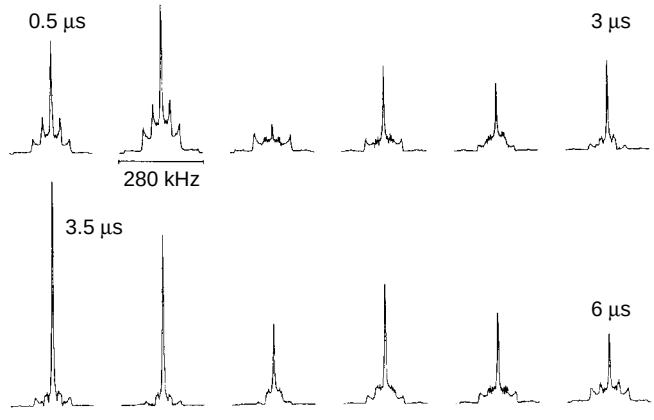

Figure 44 Effect of the second-pulse duration on the spectral line intensity and the shape of the spectrum, Fourier transform of half of the $\tau_4 = \tau_2$ Hahn echo: the $\tau_4 = \tau_2$ Hahn echo spectra of ^{27}Al ($I = \frac{5}{2}$) in a polycrystalline sample of $KAl(SO_4)_2 \cdot 12H_2O$, acquired with the sequence $\{X\}$—τ_2—$\{\pm X\}$, $\tau_2 = 160$ μs and $D_0 = 1$ s; $T_{FID} = 200$ μs. The second-pulse duration t_3 increases from 0.5 to 6 μs by steps of 0.5 μs. (Reprinted from P.P. Man, E. Duprey, J. Fraissard, P. Tougne, J.-B. d'Espinose, 'Spin-$\frac{5}{2}$ Hahn Echoes in Solids', *Solid State NMR*, **5**, 181–188, Copyright (1995), with permission from Elsevier Science.)

the pyrochlore $RbNb_2O_5F$, or aluminum in $KAl(SO_4)_2 \cdot 12H_2O$.

3.5.7 Any Spin I *in a Fast-rotating Sample*

In this and the following section, the sample rotates at the magic angle θ_m under rapid conditions during the two-pulse experiment. The following interactions (Equations 96 and 97) are taken into account to predict the spin dynamics (Figure 9d):

$$H_{int} = H_{CS} + H_Q^{(2)\text{fast MAS}} \tag{96}$$

$$\begin{pmatrix} a_{11} & a_{12} & a_{13} & a_{14} & a_{15} & a_{16} \\ a_{21} & a_{22} & a_{23} & a_{24} & a_{25} & a_{26} \\ a_{31} & a_{32} & a_{33} & \boxed{a_{34}} & a_{35} & a_{36} \\ a_{41} & a_{42} & a_{43} & a_{44} & a_{45} & a_{46} \\ a_{51} & a_{52} & a_{53} & a_{54} & a_{55} & a_{56} \\ a_{61} & a_{62} & a_{63} & a_{64} & a_{65} & a_{66} \end{pmatrix} = \mathrm{Texp}(-\mathrm{i}t_1\Omega)T^{\dagger} \begin{pmatrix} \frac{5}{2} & 0 & 0 & 0 & 0 & 0 \\ 0 & \frac{3}{2} & 0 & 0 & 0 & 0 \\ 0 & 0 & \frac{1}{2} & 0 & 0 & 0 \\ 0 & 0 & 0 & -\frac{1}{2} & 0 & 0 \\ 0 & 0 & 0 & 0 & -\frac{3}{2} & 0 \\ 0 & 0 & 0 & 0 & 0 & -\frac{5}{2} \end{pmatrix} \mathrm{Texp}(\mathrm{i}t_1\Omega)T^{\dagger}$$

$$\begin{pmatrix} s_{11} & s_{12} & s_{13} & s_{14} & s_{15} & s_{16} \\ s_{21} & s_{22} & s_{23} & s_{24} & s_{25} & s_{26} \\ s_{31} & s_{32} & s_{33} & s_{34} & s_{35} & s_{36} \\ s_{41} & s_{42} & s_{43} & s_{44} & s_{45} & s_{46} \\ s_{51} & s_{52} & s_{53} & s_{54} & s_{55} & s_{56} \\ s_{61} & s_{62} & s_{63} & s_{64} & s_{65} & s_{66} \end{pmatrix} = \mathrm{Texp}(-\mathrm{i}t_3\Omega)T^{\dagger} \begin{pmatrix} 0 & 0 & 0 & 0 & 0 & 0 \\ 0 & 0 & 0 & 0 & 0 & 0 \\ 0 & 0 & 0 & a_{34} & 0 & 0 \\ 0 & 0 & 0 & 0 & 0 & 0 \\ 0 & 0 & 0 & 0 & 0 & 0 \\ 0 & 0 & 0 & 0 & 0 & 0 \end{pmatrix} \mathrm{Texp}(\mathrm{i}t_3\Omega)T^{\dagger}$$

Figure 45 Numerical procedure for calculating the complex amplitude s_{43} of the central-transition $\tau_4 = \tau_2$ Hahn echo of a spin $I = \frac{5}{2}$, valid for static condition whatever the pulse durations or fast MAS condition with short pulse durations. The initial condition for the first RF pulse is the Boltzmann density matrix containing nonzero but real diagonal elements. The initial condition for the second RF pulse is the matrix containing only one nonzero but complex element, a_{34}, provided by the density matrix of the first RF pulse. The other parameters are identical to those of Figure 31.

during the free precession of the spin system, because $H_{\mathrm{Q}}^{(1)} = 0$ in the fast condition; and

$$H = H_{\mathrm{Q}}^{(1)} + H_{\mathrm{RF}} \tag{97}$$

during the RF pulses. The static Hamiltonian is considered during the RF pulses, which means that the pulse durations must be short enough so that the rotor appears static during the excitation of the spin system.

3.5.7.1 p-*Quantum Line Shift* In theoretical study, the isotropic chemical shift $\delta_{\mathrm{CS}}^{(\mathrm{iso})}$ of a line located at w_{L} is referenced relative to w_{c}. The contribution of H_{CS} (Equation 38) to the absorption line position with respect to w_{c} is defined by Equation (98):

$$\begin{aligned} w_{r,c}^{(\mathrm{iso})} &= \langle r|H_{\mathrm{CS}}|r\rangle - \langle c|H_{\mathrm{CS}}|c\rangle = -(r-c)w_{\mathrm{c}}\delta_{\mathrm{CS}}^{(\mathrm{iso})} \\ &= -(r-c)(w_{\mathrm{L}} - w_{\mathrm{c}}) \end{aligned} \tag{98}$$

The analytical expression of $H_{\mathrm{Q}}^{(2)\mathrm{fast\ MAS}}$ is unknown but is defined by the second-order quadrupole shift $w_{r,c}^{(2)\mathrm{fast\ MAS}}$ of the $(r-c)$-quantum absorption line relative to w_{L} (Equation 99):

$$w_{r,c}^{(2)\mathrm{fast\ MAS}} = \langle r|H_{\mathrm{Q}}^{(2)\mathrm{fast\ MAS}}|r\rangle - \langle c|H_{\mathrm{Q}}^{(2)\mathrm{fast\ MAS}}|c\rangle \tag{99}$$

We confine ourselves to investigate the on-resonance symmetrical coherences. On-resonance means "in the second main diagonal of the density matrix". Symmetrical means "connecting $|r\rangle$ with $|-r\rangle$", that is, $c = -r$. In this case, the coherence order is $p = 2r$ and[18]

$$\begin{aligned} w_{p/2,-p/2}^{(2)\mathrm{fast\ MAS}} &= -\frac{\Omega_{\mathrm{Q}}^2}{w_{\mathrm{L}}}\Big\{\tfrac{1}{2}C_0(I,p)B_{00}(\eta) + \tfrac{1}{2}C_2(I,p) \\ &\quad \times \{B_{40}(\eta)d_{0,0}^{(4)}(\beta_1) + 2B_{42}(\eta)d_{2,0}^{(4)}(\beta_1)\cos 2\alpha_1 \\ &\quad + 2B_{44}(\eta)d_{4,0}^{(4)}(\beta_1)\cos 4\alpha_1\}P_4(\cos\theta_{\mathrm{m}})\Big\} \\ &= w_{p/2,-p/2}^{(2)\mathrm{iso}}(I,p) - k(I,p)\xi_{-1/2,1/2} \\ &= \lambda(I,p)w_{-1/2,1/2}^{(2)\mathrm{iso}} - k(I,p)\xi_{-1/2,1/2} \end{aligned} \tag{100}$$

The parameters $C_0(I,p)$, $C_2(I,p)$, $\lambda(I,p)$, and $k(I,p)$, used in Equation (100) and given values in Table 2, are defined in Equations (101–104):

$$C_0(I,p) = p\left\{I(I+1) - \tfrac{3}{4}p^2\right\} \tag{101}$$

$$C_2(I,p) = p\left\{18I(I+1) - \tfrac{17}{2}p^2 - 5\right\} \tag{102}$$

$$\lambda(I,p) = \frac{C_0(I,p)}{C_0(I,-1)} \tag{103}$$

$$k(I,p) = -\frac{C_2(I,p)}{C_2(I,-1)} \tag{104}$$

The other parameters in Equation (100) have been defined previously.[18] The function $\xi_{-1/2,1/2}$ depends on orientation parameters. The second-order quadrupole shift of the center of gravity of the central-transition

Table 2 Parameters depending on the spin I and the coherence order p. $C_0(I,p)$ is defined by Equation (101) and $C_2(I,p)$ by Equation (102). The parameter $\lambda(I,p)$, given by Equation (103), is the ratio of the second-order quadrupole shift of the center of gravity of a spectrum generated by a pQ coherence to that of the −1Q coherence. $k(I,p)$, defined by Equation (104), defines the echo position

I	p	$C_0(I,p)$	$C_2(I,p)$	$\lambda(I,p)$	$k(I,p)$	$k(I,p)-p$
$\frac{3}{2}$	−1	−3	−54	1	−1	0
	−3	9	42	−3	7/9	34/9
$\frac{5}{2}$	−1	−8	−144	1	−1	0
	3	6	228	−3/4	19/12	−17/12
	−5	50	300	−25/4	25/12	85/12

powder pattern ($p = -1$) $w^{(2)\mathrm{iso}}_{-1/2,1/2}$ is given by Equation (36). If η cannot be determined by line-shape analysis, the parameter $C_{\mathrm{Q}\eta}$ relating $e^2qQ/\hbar$ and η (Equation 105),

$$C_{\mathrm{Q}\eta} = \frac{e^2qQ}{\hbar}\sqrt{\tfrac{1}{3}\eta^2+1} = I(2I-1)\frac{w_{\mathrm{L}}}{2\pi}\sqrt{\frac{40}{3\left\{I(I+1)-\frac{3}{4}\right\}}\left(-\frac{w^{(2)\mathrm{iso}}_{-1/2,1/2}}{w_0}\right)} \tag{105}$$

derived from Equations (12) and (36), is used for characterizing a material. This is especially the case for materials having featureless NMR line shapes in the F_2 dimension, such as glasses. As H_{CS} is also considered during free precession of the spin system, the total shift $w^{\mathrm{fast\ MAS}}_{p/2,-p/2}$ of the pQ absorption line is given by Equation (106),

$$w^{\mathrm{fast\ MAS}}_{p/2,-p/2} = \lambda(I,p)w^{(2)\mathrm{iso}}_{-1/2,1/2} - k(I,p)\xi_{-1/2,1/2} - pw_{\mathrm{c}}\delta^{(\mathrm{iso})}_{\mathrm{CS}} \tag{106}$$

which is the sum of Equations (98) and (100).

3.5.7.2 Phase Modulation of the Echo and Antiecho Amplitudes The amplitude of the central-transition FID during the acquisition period τ_4 is described by Equation (107):[18]

$$\begin{aligned}\left\langle -\tfrac{1}{2}\middle|\,\rho^{\mathrm{s}}(t_1,\tau_2,t_3,\tau_4)\,\middle|\tfrac{1}{2}\right\rangle &= \exp(-\mathrm{i}\tau_4 w^{\mathrm{fast\ MAS}}_{-1/2,1/2})\\ &\times \sum_{\substack{p=-2I\\ p\ \mathrm{odd}}}^{2I}\left\langle -\tfrac{1}{2}\middle|\,\rho^{\mathrm{s}}_p(t_1,t_3)\,\middle|\tfrac{1}{2}\right\rangle \exp(-\mathrm{i}\tau_2 w^{\mathrm{fast\ MAS}}_{p/2,-p/2})\\ &= \sum_{\substack{p=-2I\\ p\ \mathrm{odd}}}^{2I}\left\langle -\tfrac{1}{2}\middle|\,\rho^{\mathrm{s}}_p(t_1,t_3)\,\middle|\tfrac{1}{2}\right\rangle \exp(-\mathrm{i}\{\tau_4+\lambda(I,p)\tau_2\}w^{(2)\mathrm{iso}}_{-1/2,1/2})\\ &\times \exp(-\mathrm{i}\{\tau_4-k(I,p)\tau_2\}\xi_{-1/2,1/2})\\ &\times \exp(-\mathrm{i}\{\tau_4-p\tau_2\}w_{\mathrm{c}}\delta^{(\mathrm{iso})}_{\mathrm{CS}})\end{aligned} \tag{107}$$

Echoes appear at the positions τ_4 defined by the three conditions of Equation (108):

$$\tau_4+\lambda(I,p)\tau_2 = 0, \quad \tau_4 - k(I,p)\tau_2 = 0, \quad \tau_4 - p\tau_2 = 0 \tag{108}$$

By convention the refocusing of coherence occurring after the second RF pulse is an echo, whereas that occurring before the second RF pulse is an antiecho. They are central-transition signals. As $\lambda(I,p)$ and $k(I,p)$ are odd functions of p, the positions of the echoes and antiechoes are symmetrical with respect to $\tau_4 = 0$.

For a given I and p, the amplitudes of the echo and antiecho located at $\tau_4 = k(I,p)\tau_2$ are phase modulated as in Equations (109) and (110):

$$\left\langle -\tfrac{1}{2}\middle|\,\rho^{\mathrm{s}}(t_1,\tau_2,t_3,\tau_4 = k(I,p)\tau_2)\,\middle|\tfrac{1}{2}\right\rangle = \left\langle -\tfrac{1}{2}\middle|\,\rho^{\mathrm{s}}_p(t_1,t_3)\,\middle|\tfrac{1}{2}\right\rangle \times \exp\{-\mathrm{i}\tau_2 w_{\mathrm{F1}}(I,p)\} \tag{109}$$

$$w_{\mathrm{F1}}(I,p) = \{k(I,p)+\lambda(I,p)\}w^{(2)\mathrm{iso}}_{-1/2,1/2} + \{k(I,p)-p\}w_{\mathrm{c}}\delta^{(\mathrm{iso})}_{\mathrm{CS}} \tag{110}$$

The term $w_{\mathrm{F1}}(I,p)$ depends on two isotropic shift values, $w^{(2)\mathrm{iso}}_{-1/2,1/2}$ and $\delta^{(\mathrm{iso})}_{\mathrm{CS}}$, and is therefore independent of the nature of the sample (single crystal or powder). As a result, $w_{\mathrm{F1}}(I,p)$ is not broadened by orientation-dependent parameters when the sample is polycrystalline. Equation (110) plays a crucial role in MQ/MAS methodology. The density matrix $\rho^{\mathrm{s}}_p(t_1,t_3)$ in Equations (107) and (109) is defined by[17]

$$\rho^{\mathrm{s}}_p(t_1,t_3) = T\exp(-\mathrm{i}\Omega t_3)T^{\dagger}\rho^{\mathrm{s}}_p(t_1)T\exp(\mathrm{i}\Omega t_3)T^{\dagger} \tag{111}$$

Equation (111) differs from Equation (43) by the initial density operator, $\rho^{\mathrm{s}}_p(t_1)$ instead of $\rho(0)$. In fact Equation (111) has been used within the two numerical procedures described in sections 3.4.3 and 3.5.5. Similarly, the amplitudes of echo and antiecho located at $\tau_4 = -\lambda(I,p)\tau_2$ are phase modulated by

$$w_{\mathrm{F1}}(I,p) = -\{k(I,p)+\lambda(I,p)\}\xi_{-1/2,1/2} - \{p+\lambda(I,p)\}\delta^{(\mathrm{iso})}_{\mathrm{CS}}w_{\mathrm{c}} \tag{112}$$

Those of the echo and antiecho located at $\tau_4 = p\tau_2$ are phase modulated by

$$w_{\mathrm{F1}}(I,p) = \{p+\lambda(I,p)\}w^{(2)\mathrm{iso}}_{-1/2,1/2} + \{p-k(I,p)\}\xi_{-1/2,1/2} \tag{113}$$

Equations (112) and (113) depend on $\xi_{-1/2,1/2}$, which is a function of orientation parameters. In a powder sample, this dependence may destroy the echoes and antiechoes.

For the $\tau_4 = \tau_2$ Hahn echo, which is the refocusing of the 1Q coherence developed at the end of the first RF pulse, we have from Table 2: $p = 1$, $k(I,1) = 1$, and $\lambda(I,1) = -1$, that is, $w_{\mathrm{F1}}(I,1) = 0$ for Equations (110), (112) and (113). The amplitudes of the $\tau_4 = \tau_2$ Hahn echo (1Q echo) and the $\tau_4 = -\tau_2$ Hahn antiecho (-1Q antiecho) are not phase modulated. The MQ/MAS method (see section 3.5.8), if it is applied to the $\tau_4 = \tau_2$ Hahn echo, will not split peaks in the F_1 dimension.

Figure 46 presents the echoes for the spin $I = \frac{3}{2}$ system.[49] The echo located at $\tau_4 = \frac{7}{9}\tau_2$, which is the refocusing of the -3Q coherence developed at the end of the first RF pulse, is called -3Q echo and is close to the 1Q echo. The latter has an amplitude much

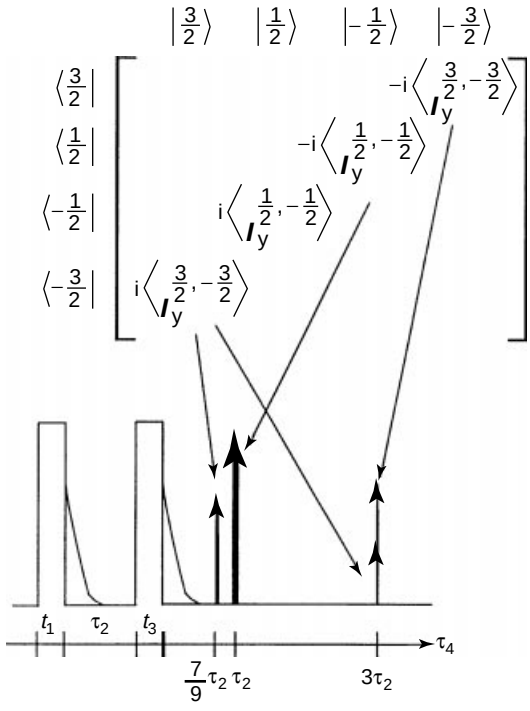

Figure 46 On-resonance coherences in the second main diagonal of the spin $I = \frac{3}{2}$ density matrix developed at the end of the first RF pulse and refocused as Hahn echoes by the second RF pulse in rapid MAS conditions: the thick arrow at $\tau_4 = \tau_2$ is the 1Q Hahn echo, the medium arrow at $\tau_4 = \frac{7}{9}\tau_2$ is the echo observed in the 3Q MAS experiment, and the thin arrows at $\tau_4 = 3\tau_2$ are echoes not often observed. On-resonance coherences and corresponding echoes are connected by arrows. Antiechoes are not shown. (Reproduced by permission of The American Physical Society from P.P. Man, *Phys. Rev. B*, **55**, 8406–8424 (1997).)

larger than that of the −3Q echo. As the 3Q and −3Q coherences at the end of the first RF pulse have opposite amplitudes, Figure 47 only shows the graph of the imaginary part,

$$\left\langle I_y^{\frac{3}{2},-\frac{3}{2}}(t_1)\right\rangle = \mathrm{Tr}\left\{\rho(t_1)\, I_y^{\frac{3}{2},-\frac{3}{2}}\right\}$$

of the 3Q coherence for a spin $I = \frac{3}{2}$, for three values of quadrupole coupling.[49] Their maxima are obtained with longer pulse duration than that used for −1Q coherence. As far as the pulse durations are short enough, the transfer function can be calculated by using the numerical procedure described in section 3.5.5.

Phase cycling the RF pulse and the receiver is required to cancel the 1Q echo and the −1Q antiecho without affecting the −3Q echo and the 3Q antiecho of an $I = \frac{3}{2}$ system. The other method is to apply a pulsed magnetic field gradient to cancel the unwanted echo and antiecho.[97]

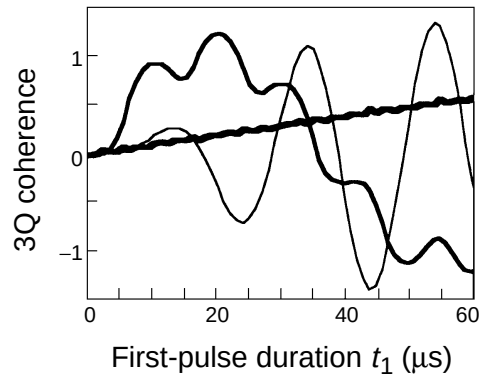

Figure 47 Graph of the excitation function (or the imaginary part) of the 3Q on-resonance coherence for a spin $I = \frac{3}{2}$, generated by the first RF pulse in a Hahn echo sequence consisting of two $-X$ pulses, versus the first-pulse duration t_1 for $w_{RF}/(2\pi) = 50$ kHz and three values of $w_Q/(2\pi)$: thin line for 10 kHz, medium line for 50 kHz, and thick line for 200 kHz. (Reproduced by permission of The American Physical Society from P.P. Man, *Phys. Rev. B*, **55**, 8406–8424 (1997).)

3.5.8 Multiple Quantum/Magic-angle Spinning Under Rapid Conditions

Frydman and colleagues[47,98] introduced the MQ/MAS methodology, which is based on 2-D methods. The MQ/MAS methodology takes advantage of the properties of the MQ coherences to generate high-resolution isotropic spectra along the F_1 dimension, giving the number of different crystallographic sites in a compound when the conventional 1-D MAS experiment provides overlapping absorption lines. Among all the coherences generated by the first RF pulse, the specific MQ coherences are detected selectively by phase cycling the RF pulses and the receiver in the Hahn echo sequence. A sheared 2-D MQ/MAS spectrum represents the correlation of a specific MQ coherence in the F_1 dimension with an SQ coherence in the F_2 dimension. The 2-D spectrum associated with a single site consists of a single peak, an MQ-filtered central-transition peak (simply called the peak in the remainder of this article). Provided that the sheared 2-D MQ/MAS spectrum is labeled in chemical shift units and the zero ppm positions in both axes are defined, knowledge of the two observed chemical shifts of the center of gravity $\delta_{G1}^{(obs)}$ and $\delta_{G2}^{(obs)}$ of a peak in the two dimensions (F_1 and F_2) enables determination of the true isotropic chemical shift $\delta_{CS}^{(iso)}$ of an absorption line. The asymmetry parameter η may be determined by the line shape of the cross-section of a peak parallel to F_2.

The rotor spinning axis is at the magic angle throughout the experiment. Thus a standard MAS probehead suffices for the experiment, but the NMR spectrometer must be equipped with a digital dephaser of the RF

pulses or a pulsed magnetic field gradient probe. The optimum experimental conditions for MQ/MAS experiments are strong RF pulses, small offset, and high rotor spinning rate.[99] Quantitative results on spin populations are not obvious, but are possible under particular conditions. Conventional 1-D MAS spectra obtained with short pulse durations allow determination of the spin populations if the absorption lines are not overlapping (section 3.1.4.1). If not, the MQ/MAS methodology can be used to determine the number of peaks or crystallographic sites, their true isotropic chemical shifts, and the quadrupole parameters. Thanks to these data, the 1-D MAS spectra can be simulated to obtain the spin population of each site.[100]

3.5.8.1 Selective Detection of the ±3Q Coherences To cancel the 1Q echo and −1Q antiecho in the two-pulse sequence, the standard way is to cycle the RF pulse phases and that of the receiver. We have already applied a mathematical approach.[49] Here we apply a diagramatic approach. Figure 48(a–c) shows the positions of the on-resonance coherences (±1Q and ±3Q) at the end of the first RF pulse when the RF field $\mathbf{B}_1$ is positioned at 0°, 120°, and 240° in the rotating frame. The ±3Q coherences remain along the y axis of the receiver, in agreement with Equation (64). Cycling according to these three cases co-adds the ±3Q coherences and cancels the ±1Q coherences. However the zero-quantum coherences are not affected by this RF pulse cycling and are also co-added; they will contribute to the FID following the second RF pulse. To cancel the zero-quantum coherences, $\mathbf{B}_1$ is positioned at 90°, 180°, and 300° (Figure 48d–f). The

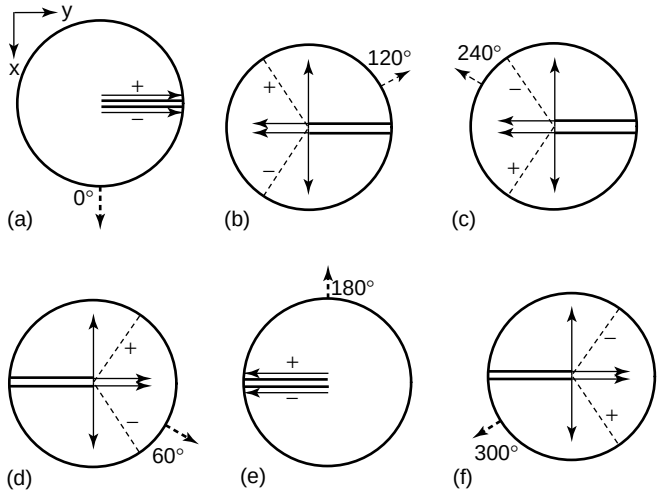

Figure 48 Evolution of the ±1Q on-resonance coherences (dashed lines, + for 1Q and − for −1Q) with their projections (arrows) along the x and y axis of the rotating frame and that of the ±3Q on-resonance coherences (thick lines) for the six positions of the RF field $\mathbf{B}_1$ (dashed arrows) at the end of the first RF pulse in the two-pulse MQ/MAS experiment: (a) 0°, (b) 120°, (c) 240°, (d) 60°, (e) 180°, and (f) 300°.

±1Q coherences are canceled but ±3Q coherences are along the $-y$ axis of the receiver. To co-add the contributions of the ±3Q coherences to those of Figure 48(a–c) the receiver phase must be set to $-y$. In this case the contributions of the zero-quantum coherences are also canceled. As a result, these six phase-cyclings of the first RF pulses and the receiver allow selective detection of the ±3Q coherences generated by the first RF pulse.[101]

3.5.8.2 Experimental and Data Processing From now on, standard notation for 2-D NMR is used: t_1 (the pulse separation) is the experimental evolution period, and t_2 is the acquisition period. First, the echo signal is optimized by systematic variation of each pulse duration.[99] Then, signal acquisition in the 2-D experiment occurs as follows: for each increment Δt_1 of the experimental evolution period, the time-domain signals appearing after the second RF pulse are acquired in the simultaneous mode. To obtain a pure 2-D absorption spectrum, the hypercomplex method[102] for generating quadrature detection in the t_1 domain is applied during the signal acquisition. Sometimes the increment of the experimental evolution period is synchronized with the rotor spinning rate.[103]

Double Fourier transform of the experimental data from $F(t_1, t_2)$ to $F(w_1, w_2)$ via $F(t_1, w_2)$ yields a pure 2-D absorption spectrum but tilted. However a shearing transformation of $F(t_1, w_2)$ yields a powder pattern along the F_2 dimension, and a high-resolution featureless line shape in the F_1 dimension. The sheared 2-D spectrum becomes a 2-D isotropic/anisotropic correlation spectrum. More details on the shearing transformation can be found in literature.[49,98,102]

3.5.8.3 Labeling the F_1 Axis in the Frequency Unit The spectral width (SW) in the F_1 dimension (SW1) of a 2-D MQ/MAS spectrum is equal to the inverse of the increment of the evolution period. Unfortunately, two definitions of the evolution period appear in the literature, giving two conventions for scaling in frequency units the SW1. The first convention (Cz) considers the experimental evolution period as the evolution period;[98,104] therefore $\mathrm{SW1_{Cz}} = 1/(\Delta t_1)$. The second convention (Ck) considers the position of the echo relative to the first RF pulse, equal to $(1 + k)$ times the experimental evolution period, as the evolution period;[102,105] therefore $\mathrm{SW1_{Ck}} = 1/\{(1 + k)\Delta t_1\}$. This article uses the Cz convention, because both conventions have been compared previously.[49]

If we synchronize the increment of the experimental evolution period Δt_1 with the inverse of the rotor spinning rate ν_{rotor}, that is if $\Delta t_1 = 1/\nu_{\mathrm{rotor}}$, then $\mathrm{SW1_{Cz}} = \nu_{\mathrm{rotor}}$. Spinning sidebands along the F_1 dimension, located outside the $\mathrm{SW1_{Cz}}$, will be folded back onto the centerband, increasing the spectral line intensity and improving the line shape of the centerband.[103] However,

Table 3 Relationships of various parameters of chemical shift (CS), offset, shift, and center of gravity (CG) expressed with respect to the carrier frequency w_c, the coherence order p of the echo located at kt_1, and λ (Equation 103) used in this paper and those of Amoureux and Fernandez[106] for sheared 2-D MQ/MAS spectra. ($w_{F1}(I,p) = (k+\lambda)w^{(2)iso}_{-1/2,1/2} + (k-p)\delta^{(iso)}_{CS} w_c$; $k \equiv R$ in Amoureux and Fernandez's notation.)

Parameter	This paper	Amoureux and Fernandez[106]
$\delta^{(obs)}_{G2}$:[a]	$\delta^{(iso)}_{CS} + \frac{w^{(2)iso}_{-1/2,1/2}}{w_c}$	$\delta^{(iso)}_{CS} + \frac{w^{(2)iso}_{-1/2,1/2}}{w_c}$
$\delta^{(obs)}_{G1z}$:[b]	$\frac{w_{F1}(I,p)}{w_c} = (k-p)\delta^{(iso)}_{CS} + (k+\lambda)\frac{w^{(2)iso}_{-1/2,1/2}}{w_c}$	$\frac{w_{F1}(I,p)}{(k-p)w_c} = \delta^{(iso)}_{CS} - \frac{10}{17}\frac{w^{(2)iso}_{-1/2,1/2}}{w_c}$
$\delta^{(iso)}_{CS}$:[c]	$\frac{10}{27}\delta^{(obs)}_{G2} - \frac{1}{p+\lambda}\delta^{(obs)}_{G1z}$	$\frac{10}{27}\delta^{(obs)}_{G2} + \frac{17}{27}\delta^{(obs)}_{G1z}$
$\frac{w^{(2)iso}_{-1/2,1/2}}{w_c}$:[d]	$\frac{1}{\lambda+p}\{\delta^{(obs)}_{G1z} - (k-p)\delta^{(obs)}_{G2}\}$	$\frac{17}{27}(\delta^{(obs)}_{G2} - \delta^{(obs)}_{G1z})$
Ω_{F2}:[e]	Experimental	Experimental
δ_{F2}:[f]	$\frac{\Omega_{F2}}{w_c}$	$\frac{\Omega_{F2}}{w_c}$
Ω_{F1z}:[g]	$(k-p)\Omega_{F2}$	$(k-p)\Omega_{F2}$
δ_{F1z}:[h]	$\frac{\Omega_{F1z}}{w_c} = (k-p)\delta_{F2}$	$\frac{\Omega_{F1z}}{(k-p)w_c} = \delta_{F2}$

[a] Observed chemical shift of the center of gravity of a peak in the F_2 dimension.
[b] Observed chemical shift of the center of gravity of a peak in the F_1 dimension.
[c] Isotropic chemical shift.
[d] Second-order quadrupole shift of the central line expressed as chemical shift.
[e] Offset of the frequency carrier with respect to the aqueous solution in the F_2 dimension.
[f] chemical shift of the frequency carrier with respect to the aqueous solution in the F_2 dimension.
[g] Offset of the frequency carrier with respect to the aqueous solution in the F_1 dimension.
[h] chemical shift of the frequency carrier with respect to the aqueous solution in the F_1 dimension.

if ν_{rotor} is not high enough and the spectrum consists of several centerbands, one or several of them can be located outside the $SW1_{Cz}$ but still appear within the $SW1_{Cz}$ as a result of folding. Consequently, the positions of the center of gravity of these folded centerbands will be incorrect.

3.5.8.4 Labeling the F_1 *Axis in Chemical Shift Units*
In theoretical study, the isotropic chemical shifts of a peak along the F_1 and F_2 dimensions of a 2-D spectrum are referenced to w_c, which is located at the center of each of the two SWs. However, the second-order quadrupole shift is referenced to w_L. If the acquisition of the data starts at the position $t_2 = kt_1$ of the echo, the position $w_{F1}(I,p)$ of a peak relative to w_c along the F_1 dimension is given by Equation (110). Therefore, the observed chemical shift of its center of gravity $\delta^{(obs)}_{G1}$ with respect to w_c is equal to its position divided by w_c (Equation 114):

$$\delta^{(obs)}_{G1} = \frac{w_{F1}(I,p)}{w_c} \tag{114}$$

Amoureux and Fernandez[106] apply Equation (115):

$$\delta^{(obs)}_{G1} = \frac{w_{F1}(I,p)}{(k-p)w_c} \tag{115}$$

that is, the carrier frequency in the F_1 dimension is $(k-p)w_c$ instead of w_c. In some cases $(k-p)w_c$ takes a negative value. Table 3 shows the main differences between these two points of view.

As the aim of the shearing transformation is to shift data acquisition from the end of the second RF pulse to the echo position after the end of the 2-D signal acquisition,[49] Equations (110), (112) and (113) remain valid for a sheared 2-D spectrum. Along the F_1 dimension, the observed chemical shift of the center of gravity of a peak relative to w_c (Equation 114) for the Cz convention is given by Equation (116):

$$\delta^{(iso)}_{G1z} = (k-p)\delta^{(obs)}_{CS} + (k+\lambda)\frac{w^{(2)iso}_{-1/2,1/2}}{w_c} \tag{116}$$

As the observed chemical shift of the center of gravity of the central-transition powder pattern relative to w_c along the F_2 dimension $\delta^{(obs)}_{G2}$ is given by Equation (37), the latter and Equation (116) allow deduction of the true isotropic chemical shift of a peak relative to w_c (Equation 117):

$$\delta^{(iso)}_{CS} = \frac{(k+\lambda)\delta^{(obs)}_{G2} - \delta^{(obs)}_{G1z}}{p+\lambda} = \frac{10}{27}\delta^{(obs)}_{G2} - \frac{1}{p+\lambda}\delta^{(obs)}_{G1z} \tag{117}$$

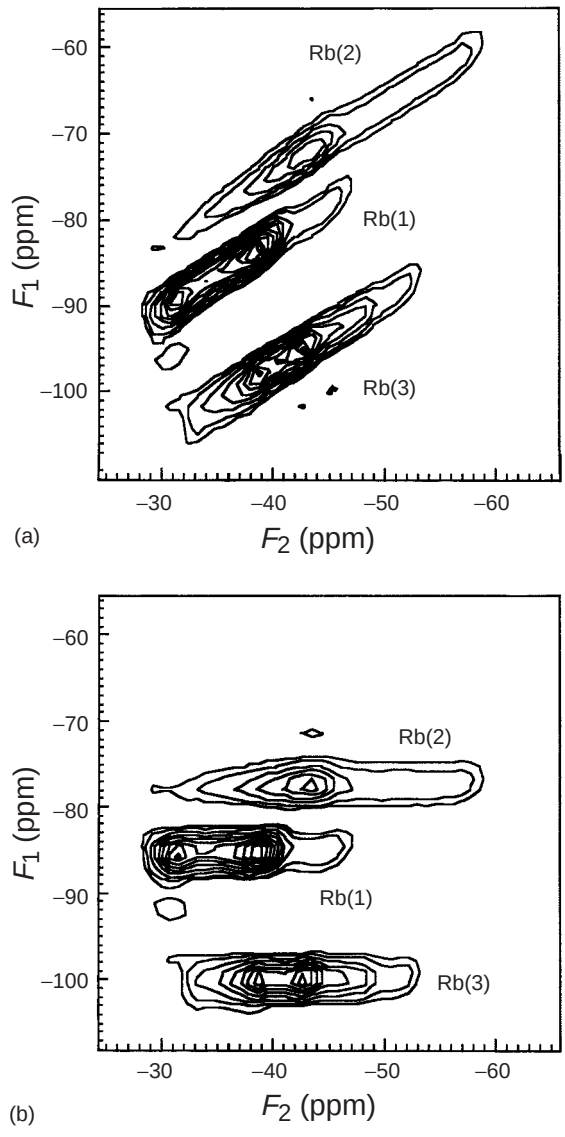

Figure 49 Contour plot of the (a) unsheared and (b) sheared 2-D 3Q-MAS spectra of ^{87}Rb ($I = \frac{3}{2}$) in $RbNO_3$ powder, obtained at 98.2 MHz. The three Rb sites, Rb(1), Rb(2), and Rb(3) are observed. The axis of the F_1 dimension is labeled using the Cz convention. The F_2 dimension is the usual chemical shift axis. (Reproduced by permission of The American Physical Society from P.P. Man, *Phys. Rev. B*, **58**, 2764–2782 (1998).)

From a practical point of view, in a 1-D spectrum or the F_2 dimension of a 2-D spectrum, the chemical shift of an absorption line is referenced experimentally to an external aqueous solution with $\delta_{CS}^{(iso)} = 0$ ppm, by definition. For both dimensions of a 2-D MQ/MAS spectrum, knowing the frequency offsets of w_c relative to the aqueous solution, Ω_{F1} in the F_1 dimension and Ω_{F2} in the F_2 dimension, allows us to express the observed chemical shifts of the center of gravity of any peak ($\delta_{G1}^{(obs)}$ in the F_1 dimension and $\delta_{G2}^{(obs)}$ in the F_2 dimension) relative to the aqueous solution. Unfortunately, Ω_{F1} differs from Ω_{F2}. For the Cz convention, this difference is given by Equation (118):

$$\Omega_{F1z} = (k - p)\Omega_{F2} \tag{118}$$

Now we know the position (Equation 112) of a peak relative to w_c and the offset (Equation 118) of w_c relative to the aqueous solution in the F_1 dimension. Therefore we know the position of the peak relative to the aqueous solution, which is what we are looking for. As the offsets in both dimensions are known, Equations (37), (116) and (117) remain valid even when the observed chemical shifts of the center of gravity of a peak along the two axes are referenced to an aqueous solution instead of w_c.

We can also deduce $w_{-1/2,1/2}^{(2)iso}$ from Equations (37) and (116):

$$\frac{w_{-1/2,1/2}^{(2)iso}}{w_c} = \frac{1}{\lambda + p}\{\delta_{G1z}^{(obs)} - (k - p)\delta_{G2}^{(obs)}\} \tag{119}$$

However, Equation (119) does not allow us to determine the quadrupole coupling constant and the asymmetry

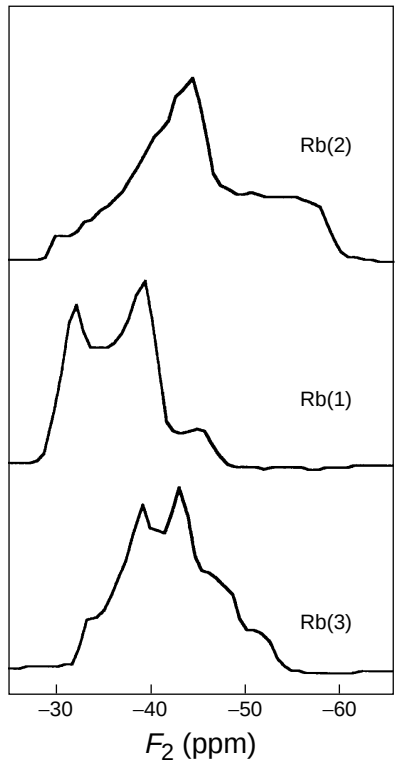

Figure 50 The three cross-section spectra (parallel to the F_2 dimension) of the sheared 2-D 3Q-MAS spectrum of ^{87}Rb ($I = \frac{3}{2}$) in $RbNO_3$ powder of Figure 49(b). (Reproduced by permission of The American Physical Society from P.P. Man, *Phys. Rev. B*, **58**, 2764–2782 (1998).)

Table 4 The carrier frequency, offset Ω_{F1} of the frequency carrier with respect to the aqueous solution, SW1, and the chemical shift range $\Delta\delta_{CS}$ in the F_1 dimension are related to the carrier frequency w_c and the offset Ω_{F2} of the frequency carrier relative to the aqueous solution in the F_2 dimension, the increment Δt_1 of the experimental evolution period, and the coherence order p of the echo located at kt_1 relative to the second RF pulse for the four conventions appearing in the literature. The Cz convention considers the experimental evolution period t_1 as the evolution period, whereas the Ck convention considers the position $(1+k)t_1$ of the echo relative to the first RF pulse as the evolution period

Convention	Carrier frequency	Ω_{F1}	SW1	$\Delta\delta_{CS}$
Cz, Medek et al.[98]	w_c	$(k-p)\Omega_{F2}$	$\frac{1}{\Delta t_1}$	$\frac{1}{w_c\Delta t_1}$
Ck, Massiot[102]	w_c	$\frac{k-p}{1+k}\Omega_{F2}$	$\frac{1}{(1+k)\Delta t_1}$	$\frac{1}{w_c(1+k)\Delta t_1}$
Cz, Amoureux and Fernandez[106]	$(k-p)w_c$	$(k-p)\Omega_{F2}$	$\frac{1}{\Delta t_1}$	$\frac{1}{(k-p)w_c\Delta t_1}$
Ck, Amoureux and Fernandez[106]	$(k-p)w_c$	$\frac{k-p}{1+k}\Omega_{F2}$	$\frac{1}{(1+k)\Delta t_1}$	$\frac{1}{(k-p)w_c(1+k)\Delta t_1}$

parameter η independently. The latter may be obtained by fitting the line shape of the cross-section (parallel to the F_2 dimension) of the peak.

Figure 49 shows the contour plots of the unsheared and sheared 2-D 3Q-MAS spectra of ^{87}Rb ($I = \frac{3}{2}$) in $RbNO_3$ powder, acquired at 98.2 MHz.[49] The F_1 axis is labeled according to the Cz convention. The three Rb sites Rb(1), Rb(2), and Rb(3) are observed. The line widths of these sheared spectra (Figure 49b) in the F_1 dimension are smaller than those in the F_2 dimension, given the high-resolution spectra along the F_1 dimension. Figure 50 presents the cross-section spectra (parallel to the F_2 dimension in Figure 49b) of the three sites.[49] Line-shape analysis provides us with the asymmetry parameter of each rubidium site.

For convenience, Table 4 gathers the relevant relationships for the two conventions, Cz and Ck, and the two points of view (the present paper using w_c as the carrier frequency and Amoureux and colleagues using $(k-p)w_c$ as the carrier frequency in the F_1 dimension).

4 PERSPECTIVE AND FUTURE DEVELOPMENTS

In solid-state NMR, the quadrupole coupling constant and the asymmetry parameter of half-integer quadrupole spins in a powder sample are determined by the central-transition powder pattern if the second-order quadrupole interaction is the main interaction. This powder pattern is generally observed with the one-pulse sequence; however, this is not always the case for the satellite transition. This article has presented both 1-D and 2-D methods based on Hahn echoes to determine these quadrupole parameters.

When the first-order quadrupole interaction becomes the main interaction, the central transition has a featureless line shape. The two parameters should be determined by the satellite-transition powder pattern if it is to be observed properly. Alternatively, some of the methods proposed in this article should be applied to determine these parameters from a featureless central-transition line shape, such as the two-pulse sequence with a short pulse separation.

As the strength of the Zeeman field $\mathbf{B}_0$ increases year after year, the effects of the second-order quadrupole interaction, which is inversely proportional to $\mathbf{B}_0$, decrease. However, the first-order quadrupole interaction, which does not depend on $\mathbf{B}_0$, is likely to become the dominant interaction in the near future. If the satellite-transition powder pattern cannot be detected properly, Solomon echo sequences should be applied. Unfortunately, these echoes are not yet well characterized. Progress in understanding these echoes is required.

LIST OF SYMBOLS

$\mathbf{B}_0$	Zeeman field
$\mathbf{B}_1$	Radiofrequency field
$\delta_{CS}^{(iso)}$	Isotropic chemical shift
$\delta_{G1}^{(obs)}$	Observed chemical shift of the center of gravity of the central-transition powder pattern in the F_1 dimension
$\delta_{G2}^{(obs)}$	Observed chemical shift of the center of gravity of the central-transition powder pattern in the F_2 dimension
D_0	Recycle delay of an NMR experiment
$e^2qQ/\hbar$	Quadrupole coupling constant
$F(t_1, \tau_2 = 0)$	Amplitude of the FID at the end of an RF pulse
F_1	First dimension of a 2-D spectrum
F_2	Second dimension of a 2-D spectrum
η	Asymmetry parameter

H_{CS}	Isotropic chemical shift interaction
H_{Δ}	Offset interaction
$H_Q^{(1)}$	First-order quadrupole interaction
$H_Q^{(2)}$	Second-order quadrupole interaction
$H_Q^{(2)\text{fast MAS}}$	Second-order quadrupole interaction of a sample rotating at the magic angle under rapid conditions
H_Z	Zeeman interaction
I	Nuclear spin
$\langle I_y(t_1)\rangle$	Amplitude of an FID at the end of an RF pulse
θ_m	Magic angle ($= 54°44'$)
t_1	Duration of the first RF pulse, or the evolution period in a 2-D experiment
t_2	Acquisition period in a 2-D experiment
t_3	Duration of the second RF pulse in a two-pulse sequence
τ_2	Acquisition period in a one-pulse sequence, or separation between the two RF pulses in a two-pulse sequence
τ_4	Acquisition period in a two-pulse sequence
T_1	Spin–lattice relaxation time of a nuclear spin
T_{FID}	Duration of FID
$w_{-1/2,1/2}^{(2)\text{iso}}$	Second-order quadrupole shift of the center of gravity of the central-transition powder pattern
w_L	Larmor frequency
w_{RF}	Amplitude of the RF pulse
w_Q	Quadrupole coupling
w_c	Carrier frequency
$\zeta^2(m+1, m)$	Probability per second that an RF field induces a transition between $\lvert m\rangle$ and $\lvert m+1\rangle$

ABBREVIATIONS AND ACRONYMS

CW	Continuous Wave
EFG	Electric-field Gradient
FID	Free-induction Decay
MAS	Magic-angle Spinning
MQ	Multiple Quantum
MQ/MAS	Multiple Quantum/Magic-angle Spinning
NMR	Nuclear Magnetic Resonance
PAS	Principal-axis System
RF	Radiofrequency
SQ	Single Quantum
SW	Spectral Width
VAS	Variable-angle Spinning
1-D	One-dimensional
2-D	Two-dimensional

RELATED ARTICLES

Biomedical Spectroscopy **(Volume 1)**
Multinuclear Magnetic Resonance Spectroscopic Imaging

Coatings **(Volume 2)**
Nuclear Magnetic Resonance of Coating and Adhesive Systems

Forensic Science **(Volume 5)**
Nuclear Magnetic Resonance Spectroscopy for the Detection and Quantification of Abused Drugs

Particle Size Analysis **(Volume 6)**
Surface Area and Pore Size Distributions

Polymers and Rubbers **(Volume 9)**
Nuclear Magnetic Resonance, Solid State in Analysis of Polymers and Rubbers

Steel and Related Materials **(Volume 10)**
Nuclear Magnetic Resonance in Metals Analysis

Nuclear Magnetic Resonance and Electron Spin Resonance Spectroscopy **(Volume 13)**
Nuclear Magnetic Resonance and Electron Spin Resonance Spectroscopy: Introduction

Nuclear Magnetic Resonance and Electron Spin Resonance Spectroscopy cont'd **(Volume 14)**
Nuclear Magnetic Resonance of Geological Materials and Glasses • Quadrupolar Nuclei in Solid-state Nuclear Magnetic Resonance • Solid-state Nuclear Magnetic Resonance • Zeeman Interaction in Nuclear Magnetic Resonance

REFERENCES

1. A. Abragam, *The Principles of Nuclear Magnetism*, Clarendon Press, Oxford, 1961.
2. R.V. Pound, 'Nuclear Electric Quadrupole Interactions in Crystals', *Phys. Rev.*, **79**, 685–702 (1950).
3. J.L. Dye, A.S. Ellaboudy, J. Kim, 'Solid State NMR of Quadrupolar Nuclei', in *Modern NMR Techniques and Their Application in Chemistry, Pract. Spectr. Ser.*, eds. A.I. Popov, K. Hallenga, Marcel Dekker, New York, 217–323, Vol. 11, 1991.

4. M.H. Cohen, F. Reif, 'Quadrupole Effects in Nuclear Magnetic Resonance Studies of Solids', in *Solid State Physics*, eds. F. Seitz, D. Turnbull, Academic Press, New York, 321–438, Vol. 5, 1957.
5. F. Borsa, A. Rigamonti, 'Comparison of NMR and NQR Studies of Phase Transitions in Disordered and Ordered Crystals', in *Topics in Current Physics, Structural Phase Transitions II*, eds. K.A. Müller, H. Thomas, Springer-Verlag, Berlin, 83–183,Vol. 45, 1991.
6. A. Rigamonti, 'NMR/NQR Studies of Structural Phase Transitions', *Adv. Phys.*, **33**, 115–191 (1984).
7. D. Freude, J. Haase, 'Quadrupole Effects in Solid-state Nuclear Magnetic Resonance', in *NMR Basic Principles and Progress*, eds. P. Diehl, E. Fluck, H. Günter, R. Kosfeld, J. Seelig, Springer-Verlag, Berlin, 1–90, Vol. 29, 1993.
8. R.R. Ernst, G. Bodenhausen, A. Wokaun, *Principles of Nuclear Magnetic Resonance in One and Two Dimensions*, Clarendon Press, Oxford, 1990.
9. R. Freeman, *Spin Choreography, Basic Steps in High Resolution NMR*, Spektrum Academic, Oxford, 1997.
10. K. Schmidt-Rohr, H.W. Spiess, *Multidimensional Solid-state NMR and Polymers*, Academic Press, San Diego, 1994.
11. P.P. Man, 'Quadrupole Interaction', in *Encyclopedia of Nuclear Magnetic Resonance*, eds. D.M. Grant, R.K. Harris, Wiley, Chichester, 3838–3848, 1996.
12. A.J. Vega, 'Quadrupolar Nuclei in Solids', in *Encyclopedia of Nuclear Magnetic Resonance*, eds. D.M. Grant, R.K. Harris, Wiley, Chichester, 3888–3898, 1996.
13. I. Solomon, 'Multiple Echoes in Solids', *Phys. Rev.*, **110**, 61–65 (1958).
14. E.L. Hahn, 'Spin Echoes', *Phys. Rev.*, **80**, 580–594 (1950).
15. E. Lippmaa, A. Samoson, M. Mägi, 'High-resolution ^{27}Al NMR of Aluminosilicates', *J. Am. Chem. Soc.*, **108**, 1730–1735 (1986).
16. P.P. Man, 'Numerical Analysis of Solomon Echo Amplitudes in Static Solids', *J. Chem. Phys.*, **106**, 3908–3919 (1997).
17. P.P. Man, 'Numerical Analysis of Hahn Echoes in Solids', *Phys. Rev. B*, **52**, 9418–9426 (1995).
18. P.P. Man, 'Second-order Quadrupole Effects on Hahn Echoes in Fast-rotating Solids at the Magic Angle', *Phys. Rev. B*, **55**, 8406–8424 (1997).
19. M.H. Levitt, 'The Signs of Frequencies and Phases in NMR', *J. Magn. Reson.*, **126**, 164–182 (1997).
20. K. Narita, J.J. Umeda, H. Kusumoto, 'NMR Powder Patterns of the Second-order Nuclear Quadrupole Interaction in Solids with Asymmetric Field Gradient', *J. Chem. Phys.*, **44**, 2719–2723 (1966).
21. P.P. Man, 'Measurement of Quadrupolar Coupling with a Two-pulse Sequence in Solid-state NMR', *Mol. Phys.*, **69**, 337–346 (1990).
22. D.W. Alderman, M.S. Solum, D.M. Grant, 'Methods for Analyzing Spectroscopic Line Shapes. NMR Solid Powder Patterns', *J. Chem. Phys.*, **84**, 3717–3725 (1986).
23. M. Bak, N.C. Nielsen, 'REPULSION, a Novel Approach to Efficient Powder Averaging in Solid-state NMR', *J. Magn. Reson.*, **125**, 132–139 (1997).
24. C.P. Slichter, *Principles of Magnetic Resonance*, Springer-Verlag, Berlin, 1990.
25. M. Goldman, *Quantum Description of High-resolution NMR in Liquids*, Clarendon Press, Oxford, 1988.
26. G. Bodenhausen, 'Multiple Quantum NMR', *Progr. Nucl. Magn. Reson. Spectrosc.*, **14**, 137–173 (1981).
27. G. Lindblom, H. Wennerström, B. Lindman, 'Multiple Quantum Transitions for Spin-$\frac{3}{2}$ Nuclei in the NMR Spectra of Lyotropic Liquid Crystals', *J. Magn. Reson.*, **23**, 177–179 (1976).
28. P.A. Spencer, D.G. Hughes, 'Double-quantum NMR of ^{23}Na in $NaNO_3$ by Double Resonance', *J. Magn. Reson.*, **38**, 1–8 (1980).
29. P.P. Man, R. Couty, J. Fraissard, 'Determination of the Line Intensities of ^{27}Al in Al_2O_3 by Solid-state NMR', *J. Magn. Reson.*, **86**, 613–617 (1990).
30. P.C. Taylor, J.B. Baugher, H.M. Kriz, 'Magnetic Resonance Spectra in Polycrystalline Solids', *Chem. Rev.*, **75**, 203–240 (1975).
31. J. Skibsted, N.C. Nielsen, H. Bildsøe, H.J. Jakobsen, 'Satellite Transition in MAS NMR Spectra of Quadrupolar Nuclei', *J. Magn. Reson.*, **95**, 88–117 (1991).
32. B. Herreros, P.P. Man, J.-M. Manoli, J. Fraissard, '^{139}La Solid-state NMR Investigation of Lanthanum-exchanged Y Zeolites', *J. Chem. Soc., Chem. Commun.*, 464–466 (1992).
33. D.R. Eaton, R.J. Buist, B.G. Sayer, 'The ^{59}Co Nuclear Magnetic Resonance Spectra of Polycrystalline Complexes', *Can. J. Chem.*, **65**, 1332–1335 (1987).
34. Z. Zheng, Z. Gan, N.K. Sethi, D.W. Alderman, D.M. Grant, 'An Efficient Simulation of VAS Lineshapes for the Quadrupolar Nuclei with Half-integer Spin', *J. Magn. Reson.*, **95**, 509–522 (1991).
35. D. Massiot, B. Cote, F. Taulelle, J.-P. Coutures, '^{27}Al MAS NMR of Crystalline and Amorphous Materials', in *Application of NMR Spectroscopy to Cement Science*, eds. P. Colombet, A.R. Grimmer, Gordon and Breach, Yverdon, Switzerland, 153–169, 1994.
36. D. Massiot, I. Farnan, N. Gauthier, D. Trumeau, A. Trokiner, J.-P. Coutures, 'Ga-71 and Ga-69 NMR Study of Beta-Ga_2O_3: Resolution of Four- and Six-fold Coordinated Ga Sites in Static Conditions', *Solid State NMR*, **4**, 241–248 (1995).
37. T.J. Bastow, '^{139}La NMR Characterization of La_2O_3 and $La_{1-x}Sr_xMO_3$ where M = Cr, Mn or Co', *Solid State NMR*, **3**, 17–22 (1994).
38. S. Vega, Y. Naor, 'Triple Quantum NMR on Spin Systems with $I = 3/2$ in Solids', *J. Chem. Phys.*, **75**, 75–86 (1981).

39. P.P. Man, 'Investigation of the Central Line of ^{55}Mn in $KMnO_4$ by a Two-dimensional NMR Method', *J. Magn. Reson.*, **67**, 78–90 (1986).
40. A. Wokaun, R.R. Ernst, 'Selective Excitation and Detection in Multilevel Spin Systems: Application of Single Transition Operators', *J. Chem. Phys.*, **67**, 1752–1758 (1977).
41. S. Ding, C.A. McDowell, 'Spin-locking Spectral Lineshapes of the Central Transition of Half-integer Quadrupole Systems Under MAS', *J. Mol. Struct.*, **355**, 135–142 (1995).
42. J.A.M. van der Mijden, R. Janssen, W.S. Veeman, 'Analytical Description of the $I = 5/2$ Quadrupole Nutation Experiment', *Mol. Phys.*, **69**, 53–64 (1990).
43. P.P. Man, 'Analytical Expression for the Spin-$\frac{5}{2}$ Line Intensities', *Mol. Phys.*, **78**, 307–318 (1993).
44. P.P. Man, P. Tougne, 'Exact Expression for the Spin-$\frac{7}{2}$ Line Intensities: Application to Solid State ^{59}Co(III) NMR', *Mol. Phys.*, **83**, 997–1009 (1994).
45. P. Kempgens, J. Hirschinger, P. Granger, J. Rosé, 'Spin-$\frac{7}{2}$ Nutation and Hahn-echo Amplitudes in Model Compounds and Application to the Tetrahedral Cluster $Co_4(CO)_{12}$', *Solid State NMR*, **10**, 95–103 (1997).
46. S.Z. Ageev, B.C. Sanctuary, 'Analytical Solutions for Spin-$\frac{7}{2}$ Line Intensities in Solid State NMR', *Mol. Phys.*, **84**, 835–844 (1995).
47. L. Frydman, J.S. Harwood, 'Isotropic Spectra of Half-integer Quadrupolar Spins from Bidimensional MAS NMR', *J. Am. Chem. Soc.*, **117**, 5367–5368 (1995).
48. S.Z. Ageev, P.P. Man, B.C. Sanctuary, 'Detection of Double and Four Quantum Coherences for Spin-$\frac{7}{2}$ Excited by Spin Lock Pulse Sequences', *J. Magn. Reson.*, **128**, 12–20 (1997).
49. P.P. Man, 'Scaling and Labeling the High-resolution Isotropic Axis of Two-dimensional Multiple Quantum Magic-angle-spinning Spectra of Half-integer Quadrupole Spins', *Phys. Rev. B*, **58**, 2764–2782 (1998).
50. P.P. Man, J. Klinowski, A. Trokiner, H. Zanni, P. Papon, 'Selective and Non-selective NMR Excitation of Quadrupolar Nuclei in the Solid State', *Chem. Phys. Lett.*, **151**, 143–150 (1988).
51. P.P. Man, 'Excitation Conditions for Quantitative Determination of Quadrupolar Spins with One Pulse or Spin-echo Sequences in Solid-state NMR', *Appl. Magn. Reson.*, **4**, 65–87 (1993).
52. V.H. Schmidt, 'Pulse Response in the Presence of Quadrupolar Splitting, in Pulsed Magnetic and Optical Resonance', in *Proceedings of the Ampere International Summer School 1971*, ed. R. Blinc, J. Stefan Institut, Ljubljana, 75–83, 1972.
53. L. Pandey, D.G. Hughes, 'RF Pulse Response of a System of $I = 3/2$ Nuclei in the Presence of Quadrupole Splitting', *J. Mol. Struct.*, **111**, 91–96 (1983).
54. L. Pandey, S. Towta, D.G. Hughes, 'NMR Pulse Response and Measurement of the Quadrupole Coupling Constant of $I = 3/2$ Nuclei', *J. Chem. Phys.*, **85**, 6923–6927 (1986).
55. A.P.M. Kentgens, 'Off-resonance Nutation NMR Spectroscopy of Half-integer Quadrupolar Nuclei', *Progr. Nucl. Magn. Reson. Spectrosc.*, **32**, 141–164 (1998).
56. H.W. Shin, S.H. Choh, T.H. Yeom, K.S. Hong, D.Y. Han, '1-D Nutation NMR of ^{7}Li in $LiTaO_3$ and $LiNbO_3$ Single Crystals and Powders', *J. Korean Phys. Soc.*, **32**, S662–S664 (1998).
57. A.P.M. Kentgens, J.J.M. Lemmens, F.M.M. Geurts, W.S. Veeman, 'Two-dimensional Solid-state Nutation NMR of Half-integer Quadrupolar Nuclei', *J. Magn. Reson.*, **71**, 62–74 (1987).
58. A. Samoson, E. Lippmaa, '2-D NMR Nutation Spectroscopy in Solids', *J. Magn. Reson.*, **79**, 255–268 (1988).
59. A. Samoson, E. Lippmaa, 'Excitation Phenomena and Line Intensities in High-resolution NMR Powder Spectra of Half-integer Quadrupolar Nuclei', *Phys. Rev. B*, **28**, 6567–6570 (1983).
60. P.P. Man, 'Measurement of Quadrupolar Spin Population by Solid-state NMR', *J. Magn. Reson.*, **77**, 148–154 (1988).
61. P.P. Man, 'The Two-dimensional Fourier Transform Analysis of Spin-lattice Relaxation Time', in *XXIII Congress Ampere on Magnetic Resonance*, eds. B. Maraviglia, F.D. Lucas, R. Campanella, Instituto Superiore di Sanita, Rome, 574–575, 1986.
62. G.A.H. Tijink, R. Janssen, W.S. Veeman, 'Investigation of the Hydration of Zeolite NaA by Two-dimensional ^{23}Na Nutation NMR', *J. Am. Chem. Soc.*, **109**, 7301–7304 (1987).
63. A. Samoson, E. Lippmaa, G. Engelhardt, U. Lohse, G. Jerschkewitz, 'Quantitative High-resolution Aluminium-27 NMR. Tetrahedral Nonframework Aluminium in Hydrothermally Treated Zeolites', *Chem. Phys. Lett.*, **134**, 589–592 (1987).
64. J. Klinowski, 'Nuclear Magnetic Resonance Studies of Zeolites', *Progr. Nucl. Magn. Reson. Spectrosc.*, **16**, 237–309 (1984).
65. J.M. Thomas, J. Klinowski, 'The Structure of Aluminosilicate and Related Catalysts by High-resolution Solid-state NMR Spectroscopy', *Adv. Catal.*, **33**, 199–374 (1985).
66. G. Engelhardt, D. Michel, *High Resolution Solid-state NMR of Silicates and Zeolites*, Wiley, Chichester, 1987.
67. R. Freeman, H.D.W. Hill, 'Phase and Intensity Anomalies in Fourier Transform NMR', *J. Magn. Reson.*, **4**, 366–383 (1971).
68. P.P. Man, H. Theveneau, P. Papon, 'Investigation of the Central Line of ^{93}Nb by a Two-dimensional NMR Method', *J. Magn. Reson.*, **64**, 271–277 (1985).
69. I.P. Gerothanassis, 'Methods of Avoiding the Effects of Acoustic Ringing in Pulsed Fourier Transform NMR

Spectroscopy', *Progr. Nucl. Magn. Reson. Spectrosc.*, **19**, 267–329 (1987).
70. P.P. Man, unpublished results (1998).
71. S. Zhang, X. Wu, M. Mehring, 'Elimination of the Ringing Effects in Multiple-pulse Sequences', *Chem. Phys. Lett.*, **173**, 481–484 (1990).
72. P.P. Man, 'Determination of the Quadrupolar Coupling Constant in Powdered Samples with a Two In-phase RF Pulse Sequence in Solid-state NMR', *Chem. Phys. Lett.*, **168**, 227–232 (1990).
73. M.A. Hepp, P.P. Man, A. Trokiner, H. Zanni, J. Fraissard, 'Determination of the Electric Field Gradient in $RbCaF_3$ Near the Phase Transition', *Solid State Commun.*, **84**, 869–873 (1992).
74. P.P. Man, 'Determination of Spin-$\frac{5}{2}$ Quadrupolar Coupling with Two-pulse Sequences', *Solid State NMR*, **2**, 165–180 (1993).
75. S.Z. Ageev, P.P. Man, J. Fraissard, B.C. Sanctuary, 'Determination of Quadrupolar Spin Coupling for Spin-$\frac{7}{2}$ Using Two-pulse Sequences', *Mol. Phys.*, **91**, 75–80 (1997).
76. P.P. Man, 'Double-quantum Coherence Detection in a Spin-$\frac{3}{2}$ System Excited by Two Consecutive RF Pulses', *Mol. Phys.*, **76**, 1119–1129 (1992).
77. P.P. Man, 'Measurement of the Quadrupolar Coupling with Two Pulses of Opposite Phase', *J. Magn. Reson.*, **94**, 258–267 (1991).
78. G. Bonera, M. Galimberti, 'Phase-dependence of Quadrupolar Echoes in Solids', *Solid State Commun.*, **4**, 589–591 (1966).
79. J. Butterworth, 'Spin Echoes in Solids', *Proc. Phys. Soc., London*, **86**, 297–304 (1965).
80. P.P. Man, 'Study of a Spin-$\frac{3}{2}$ System by a Spin-echo Sequence', *Mol. Phys.*, **72**, 321–331 (1991).
81. I.D. Weisman, L.H. Bennett, 'Quadrupolar Echoes in Solids', *Phys. Rev.*, **181**, 1341–1350 (1969).
82. P.P. Man, 'Solomon Echoes Extended to Soft Pulse Excitation', *Z. Naturforsch., A*, **49**, 89–96 (1994).
83. M. Mehring, O. Kanert, 'Line Shape Analysis of Spin Echo Signals in Cubic Solids', *Z. Naturforsch., A*, **24**, 768–774 (1969).
84. M. Suemitsu, N. Nakajo, 'Charged Point Defects in GaAs Crystals Evaluated by NMR Spin Echo', *J. Appl. Phys.*, **66**, 3178–3186 (1989).
85. P.P. Man, 'Importance of the Magnetic Dipolar Coupling on the Quadrupolar Spin-echo Amplitude', *J. Magn. Reson.*, **100**, 157–165 (1992).
86. A.M. Flett, J.C.S. Richards, '^{23}Na Spin Echoes in NaCl Single Crystals', *Proc. Phys. Soc.*, **86**, 171–179 (1965).
87. P.P. Man, 'Study of a Spin-$\frac{3}{2}$ System by a Spin-echo Sequence (Part 2)', *J. Chim. Phys. Phys.-Chim. Biol.*, **89**, 335–358 (1992).
88. P.P. Man, 'Mathematical Analysis of Electric-quadrupole and Heteronuclear Magnetic-dipole Interactions on Spin-$\frac{5}{2}$ Hahn Echo Amplitudes in Solids', *J. Magn. Reson. A*, **114**, 59–69 (1995).
89. P.P. Man, E. Duprey, J. Fraissard, P. Tougne, J.-B. d'Espinose, 'Spin-$\frac{5}{2}$ Echoes in Solids', *Solid State NMR*, **5**, 181–188 (1995).
90. G.N. Abelyashev, V.N. Berzhanskij, N.A. Sergeev, Y.V. Fedotov, 'Multiquantum Effects and NMR in Magnetically Ordered Substances', *Phys. Lett. A*, **133**, 263–265 (1988).
91. D.G. Hughes, L. Pandey, 'Spurious Signals Caused by the Piezoelectric Ringing of $NaNO_2$ in Pulsed NMR', *J. Magn. Reson.*, **56**, 428–442 (1984).
92. P.P. Man, 'Study of a Spin-$\frac{3}{2}$ System by a Quadrupolar-echo Sequence: Suppression of Spurious Signals', *Solid State NMR*, **1**, 149–158 (1992).
93. A.C. Kunwar, G.L. Turner, E. Oldfield, 'Solid-state Spin-echo Fourier Transform NMR of ^{39}K and ^{67}Zn Salts at High-field', *J. Magn. Reson.*, **69**, 124–127 (1986).
94. M.A. Hepp, P.P. Man, J. Fraissard, 'Excitation Conditions for Quantitative Determination of Quadrupolar Spins with a Spin-echo Sequence; Cancellation of Spurious Signals', in *Application of NMR Spectroscopy to Cement Science*, eds. P. Colombet, A.R. Grimmer, Gordon and Breach, Yverdon, Switzerland, 455–466, 1994.
95. Y. Dumazy, J.-P. Amoureux, C. Fernandez, 'Theoretical and Experimental Study of Quadrupolar Echoes in Solid State NMR', *Mol. Phys.*, **90**, 959–970 (1997).
96. R. Kimmich, *NMR: Tomography, Diffusometry, Relaxometry*, Springer-Verlag, Berlin, 1997.
97. C.A. Fyfe, J. Skibsted, H. Grondey, H.M.z. Altenschildesche, 'Pulsed Field Gradient MQ MAS NMR Spectroscopy of Half-integer Spin Quadrupolar Nuclei', *Chem. Phys. Lett.*, **281**, 44–48 (1997).
98. A. Medek, J.S. Harwood, L. Frydman, 'Multiple Quantum MAS NMR: a New Method for the Study of Quadrupolar Nuclei in Solids', *J. Am. Chem. Soc.*, **117**, 12 779–12 787 (1995).
99. J.-P. Amoureux, C. Fernandez, L. Frydman, 'Optimized MQ MAS NMR Experiments on Half-integer Quadrupoles', *Chem. Phys. Lett.*, **259**, 347–355 (1996).
100. J.-P. Amoureux, 'High-resolution Solid-state NMR for Spin-$\frac{3}{2}$ and $\frac{9}{2}$: the Multi-quantum Transition Method', *Solid State NMR*, **2**, 83–88 (1993).
101. A. Wokaun, R.R. Ernst, 'Selective Detection of Multiple Quantum Transitions in NMR by 2D Spectroscopy', *Chem. Phys. Lett.*, **52**, 407–412 (1977).
102. D. Massiot, B. Touzo, D. Trumeau, J.P. Coutures, J. Virlet, P. Florian, P.J. Grandinetti, 'Two-dimensional MAS Isotropic Reconstruction Sequences for Quadrupolar Nuclei', *Solid State NMR*, **6**, 73–83 (1996).
103. D. Massiot, 'Sensitivity and Lineshape Improvements of MQ/MAS by Rotor-synchronized Data Acquisition', *J. Magn. Reson. A*, **122**, 240–244 (1996).

104. M. Hanaya, R.K. Harris, 'Optimization of 2D MQ/MAS NMR Experiments for $I = 3/2$ Nuclei on a Moderate-field Spectrometer', *J. Phys. Chem. A*, **101**, 6903–6910 (1997).
105. S.H. Wang, Z. Xu, J.H. Baltisberger, L.M. Bull, J.F. Stebbins, A. Pines, 'MQ MAS and DAS NMR Spectroscopy of Quadrupolar Nuclei', *Solid State NMR*, **8**, 1–16 (1997).
106. J.-P. Amoureux, C. Fernandez, 'Triple, Quintuple and Higher Order Multiple Quantum MAS NMR of Quadrupolar Nuclei', *Solid State NMR*, **10**, 211–223 (1998).